博士論文

Assessment of graphite oxidization model for HTGR air ingress accident

（高温ガス炉空気侵入事故時の黒鉛酸化の評価）

呉 楊

Study on Graphite Oxidization Model for HTGR Air Ingress Accident

A dissertation submitted to
The University of Tokyo
In partial fulfillment of the requirements
For the degree of

Doctor of Philosophy

In

NUCLEAR ENGINEERING AND MANAGEMENT

By

Yang Wu

June 2017

Table of Contents

List of Figures

List of Tables

List of Symbols

A	Surface area [m^2]
b	Volume per mole that is occupied by the molecular [m^3/mole]
B_x	Body force [N/m^3]
c_p	Thermal capacity of the fluid [J/kgK]
$C_{p,V}$	Volumetric heat capacity [J/m^{3}K]
C_w	Concentration on the solid wall [mole/m^3]
d	Hydrodynamic diameter of the tube [m]
D	Diameter of the molecular [Å]
D_{AB}	Mass diffusivity [m^2/s]
E_a	Activation energy [J]
F_{ij}	View factor from surface j to i
g	Gravitational acceleration [m/s^2]
h	Convective heat transfer coefficient [W/m^{2}K]
h	Plank constant [J·s]
K_1	Pre-exponent coefficient
k	Thermal conductivity [W/mK]
k_B	Boltzmann constant [J/K]
k_c	Convective mass transfer coefficient [m/s]
k_v	Rate constant
L	Significant length [m]
L_e	Lewis number
$M(B)$	Multiplication factor
M_i	Molecular mass of species I [u]
M_{ni}	Mass of i-th noncondensable gas [g]
M_n	Total mass of noncondensable gas in the gaseous phase [kg]
$\dot{m}_{O_2}$	Oxygen mole flow rate at inlet [mole/s]
M_s	Mass of steam in the gas phase [kg]
N	Number of noncondensables
N_A	Avogadro constant [mol^{-1}]

$\mathrm{M_c}$	Molecular mass of carbon [u]
P	Total power radiated from an object [W]
P	Pressure [Pa]
P_i	Partial pressures of an individual non-condensable components [Pa]
Pr	Prandtl number
$\mathrm{P_{O_2}}$	Partial pressure of oxygen [Pa]
Q'	Heat flux into and out of the volume [W]
Q''	Internal generation of energy [W]
Q_{gf}	Sensible heat transfer rate per unit volume. This is the heat transfer at the noncondensable gas-liquid interface [W]
Q_i	Net heat flux [W/m^2]
Q_{ig}	Interface heat transfer terms related to gas [W]
Q_{if}	Interface heat transfer terms related to fluid [W]
Q_{wg}	Wall heat transfer rates per unit volume of steam [W/m^3]
Q_{wf}	Wall heat transfer rates per unit volume of liquid [W/m^3]
R	Radiosity [W/m^2]
R(0)	Reaction rate at zero burn-off [kg/s]
R(B)	Reaction rate at burn-off of B [kg/s]
s	Surface area [$\mathrm{m^2}$]
S	Internal heat source [$\mathrm{W/m^3}$]
Sh	Sherwood number
t	Time [sec]
T	Absolute temperature [K]
T_g	Temperate of the bulk fluid [K]
T_{ir}	Temperature reading of the IR thermometer [°C]
T_k	Temperature reading of the k-type thermocouple [°C]
U	Specific internal energy [J/kg]
U_i	Internal energy of an individual non-condensable components [J/kg]
v	Velocity vector [m/s]
V	Volume [m^3]
V_i	Specific volumes of an individual non-condensable components [m^3/kg]
v_g	Velocities of the gas phase [kg/s]

v_∞	Velocity of bulk fluid [kg/s]
v_f	Velocities of the fluid phase [kg/s]
x	Total length of the tube [m]
$\mathrm{X_i}$	Mole fraction of species i at outlet
X_n	Total noncondensable mass fraction in the gas phase
α_g	Vapor volume fraction
α_f	Liquid volume fraction
Γ_g	Gas generation terms
Γ_f	Liquid generation terms
Γ_n	Total noncondensable gas generation term
Γ_{ni}	Gas generation of each noncondensable species
ε	Emissivity
λ	Wavelength of infrared thermometer [μm]
μ	Dynamic viscosity of the fluid [kg/ms]
ρ_g	Boron densities in the steam phase [kg/m^3]
ρ_f	Boron densities in the fluid phase [kg/m^3]
ρ	Reflectivity
ρ_i	Density of species i [kg/m^3]
σ	Stefan-Boltzmann constant [W/m^{2}K^4]
τ	Stress tensor [N/m^2]
Δc_A	Driving force concentration difference [mole/m^3]

List of Acronyms

ATR	Advanced Test Reactor
AVR	Arbeitsgemeinshaft Versuchs Reaktor
CD-adapco	Computational Dynamics-Analysis & Design Application Company Ltd
CFD	Computational Fluid Dynamic
CHT	Conjugate Heat Transfer
EGP	Energy Heterogeneous Direct Currant Reactor with 6 Loops of Circulation of the Coolant
FEA	Finite element analysis
FOV	Field of View
FSV	Fort St.Vrain
FTIR	Fourier transform infrared spectroscopy
GCR	Gas-Cooled Reactor
GTHTR	Gas Turbine High Temperature Reactor
GT-MHR	Gas Turbine Modular Helium Reactor
HTGR	High Temperature Gas-Cooled Reactor
HTMR	High Temperature Modular Reactor
HTR	High Temperature Reactor
HTR-PM	High Temperature Reactor Pebble Bed Modules
HTTR	High Temperature Engineering Test Reactor
INET	Institute of Nuclear Energy Technology
ISS	Innovation Systems Software
JAERI	Japan Atomic Energy Research Institute
LOCA	Loss of Coolant Accident
MHR	Modular Helium Reactor
NRC	Nuclear Regulatory Commission
PBMR	Pebble Bed Modular Reactor
RBMK	Reaktor Bolshoy Moshchnosty Kanalny
RCS	Reactor Coolant System
RELAP	Reactor Excursion and Leak Analysis Program
RPV	Reactor Pressure Vessel
SCDAP	Severe Core Damage Analysis Package
SC-HTGR	Steam Cycle High Temperature Gas cooled Reactor
SDTP	SCDAP Development and Training Program
SLPM	Standard Liter Per Minute
THTR	Thorium High Temperature Reactor
VHTR	Very High Temperature Reactor
Xe	X energy

1. Introduction

1.1 Motivations

The development of high temperature gas-cooled reactor (HTGR) was started in 1950s, and recently, the technology has attracted renew interest because of its inherent safety features and its potential of cogenerating of electricity and high temperature process heat to produce hydrogen. Two HTGR test reactors are under active research and development. One is the 30MWth High Temperature engineering Test Reactor (HTTR) in Japan, the other is the 10MWth High Temperature Reactor in China (HTR-10).

The key feature of HTGR is that the reactor is operated at high temperature compared to other reactor designs. The major characteristic of HTGR technology is the helium coolant, graphite moderator and the multi-coated fuel particle design. The helium coolant is chemical inert to core components and remains single phase under all conditions. The graphite has high strength, stability， heat capacity and thermal conductivity under elevated temperature. The fuel deign, which is the refractory coated fuel particles dispersed in a graphite matrix, allows retaining fission products up to 1600˚C. A unique feature of HTGR is that the reactor core has low power density, which is effective for rejecting decay heat passively. Specifically, the decay heat can be passively transferred by natural means (conduction, natural convection and thermal radiation) to reactor pressure vessel and then pass to the environment through thermal radiation.

At present, the most critical accident for HTGR design is the air ingress, which caused by the guillotine type break of main coolant pipe. It starts with helium depressurization, after which air is anticipated to enter the core through the break, leading to oxidation of in-core graphite structures and fuel. Such a situation would have serious consequences including temperature increase due to exothermic oxidation reaction, mechanical degradation of graphite structures and accumulation of explosive CO gas in the reactor.

To understand the consequence of air-ingress, the mechanisms of graphite oxidation need to be studied first. Extensive studies regarding this topic were carried out for decades, and following conclusion were drawn. The reaction can be classified into three regimes based on temperature, which are the chemical kinetic controlled regime, the in-pore diffusion controlled regime and the mass transfer controlled regime. Also, it has been found that in chemical kinetic controlled regime, the oxidation rate is strongly dependent on the graphite burn-off with the maximum value found at 30%~40%.There are many models developed for analysis of graphite oxidation. However, several issues and concerns regarding the currently available models need to be addressed:

1) The predicted reaction rate exhibits discontinuities at the transition temperatures.

2) At a given temperature, the reaction rates predicted by different models greatly differ from each other.

3) The regime transition temperatures reported by different researchers varied widely.

4) Studies on the quantitative relationship between oxidation rate and burn-off are very limited.

Given the importance of graphite oxidation in HTGR severe accident analysis, it is important to develop computer codes, which will allow the important phenomena, such as graphite temperature transient, exothermic heat generation, etc. to be predicted and analyzed. Currently there are several system analysis codes that are capable of modeling graphite oxidation. Nevertheless, the drawbacks and limitations of those codes are identified as follows: Firstly, as some codes were developed long time ago, the oxidation correlations were developed for historical graphite grades that were no longer in use. Due to the impurity, grain size, etc., different grades of graphite are observed to have different chemical kinetic characteristics. Therefore, to calculate the oxidation rate of a specific grade of graphite, it is required to use its corresponding oxidation rate equation. Secondly, the code may experience some inconsistency within the oxidation models. For instance, in GAMMA (which is a HTGR safety analysis code), the correlation of graphite IG-110 was used for calculating graphite oxidation, whereas, for the Boudouard reaction (C/CO_2 reaction), which also occurs during an event of air ingress, the correlation of graphite A3-3 was adopted. This happened because some reaction rate data were not available while the code was developed. Thirdly, the effect of burn-off on reaction rate was not modeled in most codes. Although the mechanism was well understood, there were very limited studies on quantitatively defining the relationship between burn-off and reaction rate. Since no explicit function was given, the variation of reaction rate at different burn-off level cannot be implemented. Last but not least, all the code validations were performed using steady state graphite oxidation data, however, the validation is incomplete without transient validation, especially for HTGR safety analysis codes. Air ingress is a transient process where various physical and chemical phenomena such as thermal radiation, convection, conduction, graphite oxidation, CO combustion, etc. would take place. Therefore, only after validation against both steady state and transient cases, can the HTGR safety analysis code be considered qualified for its intended purpose. However, such transient validation experiments have not been undertaken yet.

Beside graphite oxidation, another important phenomenon in the progression of air ingress is radiation heat transfer. In HTGR, radiation heat transfer is the dominant heat removal mechanism. Therefore, accurate prediction of radiation heat transfer is as important as modeling the graphite oxidation in air ingress analysis. The rate of radiation heat transfer is dependent on temperatures, geometries, relative locations of objects in a system, emissivity, etc. For HTGRs, in order to estimate the heat removal by radiation, it is essential to obtain the exact emissivity of the major core components. In previous studies, constant emissivity of 0.8 is used in system analysis codes to estimate the overall radiation heat removal as a conservative estimation. But, emissivity is a dynamic surface property, which generally depends on temperature, wavelength, degrees of oxidation, etc. So acquiring the actual emissivity of the graphite, for both before and after oxidation, is a straightforward way to improve the accuracy of the HTGR safety analysis.

1.2 Objective of this Study

Up till now, the most critical event that may occur in HTGR is an air ingress accident, followed by a postulated main coolant pipe break. Such a situation would have serious consequences including temperature increase due to exothermic oxidation reactions, mechanical degradation of graphite structures and accumulation of explosive CO gas in the reactor. Given the potential hazards and risks caused by air ingress, it is critical to improve the HTGR safety under such event of accident, which serves as the ultimate purpose of present study.

The safety of HTGR in the event of air ingress can be improved from different aspects, for instance, developing oxidation resistance core graphites, exploring accident tolerant fuel designs, proposing countermeasures that limit the amount of air ingress into the reactor code, etc. Nevertheless, the basic principle of any studies with respect to HTGR air ingress safety evaluation would be performing HTGR safety analysis so that core behaviors, especially the transient of fuel temperature, can be predicted and analyzed during the accident.

To that end, the primary objective of this study was to improve the safety analysis of HTGR in an event of air ingress. Reactor safety analysis requires proper computational tools, which must be developed based on specific accident scenarios and validated against relevant experiments. To improve the safety analysis of an air ingress event, the present study was carried out from the following three aspects. First of all, a transient graphite oxidation experiment was design to provide insight into the progression of an air ingress-like scenario wherein graphite oxidation in conjunction with multi-mode heat transfer take place. In addition, the experimental results provide a database for the validation of computer codes used in HTGR safety analysis. Secondly, the emissivity of graphite (IG-110) was measured before and after oxidation in a wide temperature range to investigate how oxidation could affect the radiation heat transfer among graphite components during air ingress. Last but not least, IG-110 graphite oxidation models were incorporated into a system analysis code called RELAP5/SCDAP. Validation of the improved code was carried out by comparing the code's prediction with two types of graphite oxidation experiments. On is the steady state experiments which mainly focused on the process of graphite oxidation while eliminating other phenomena. The other is the transient oxidation experiment wherein the progression of graphite oxidation was accompany but radiative and convective cooling. With this further validation, RELAP5/SCDAP with a validated graphite oxidation model will exist, that can greatly aid in the safety analysis of HTGR with respect to air ingress.

1.3 Outline of this Thesis

This thesis consists of eight chapters presenting in detail how the graphite oxidation study for HTGR air ingress was carried out.

Chapter I describes the motivations and objective of this study.

Chapter II describes the general background of the present study, including a brief introduction of the history and evolution of HTGR; HTGR design features; the causes, major processes and consequences of air ingress; the characteristic and oxidation of nuclear grade graphite and the two computational tools used in this study, which are RELAP5/SCDAP and Star CCM+.

The theory backgrounds are given in Chapter III. This chapter includes a detailed explanation of classical three-regime graphite oxidation kinetics and the mass transfer theory which is relevant to calculating graphite oxidation rate. For RELAP5/SCDAP, which is the main tool for simulating graphite oxidation, the systems of conservation equations and closure relationships that describe the thermalhydraulic in the code as well as how the code treats conduction and surface-to-surface thermal radiation were presented.

Chapter IV gives a scientific literature review that establishes the motivations and requirements for the present study. The emissivity measurements of graphite and carbon, the state-of-the-art review on experimental study of nuclear grade graphite oxidation as well as the correlations developed from the experimental data and their applications in system analysis codes are presented in this chapter.

The graphite (IG-110) emissivity measurement experiment, including experimental setup, procedures, results and discussions are presented in Chapter V.

Chapter VI describes how the selected graphite oxidation models and correlations were implemented in RELAP5/SCDAP. Also, verification and validation were preformed against steady-state graphite oxidation experiments conducted by various researchers.

The transient graphite oxidization experiment conducted in the present study is described in Chapter IIV. The experimental setup, conditions, procedures and results are presented in detail. Chapter IIV also includes the simulation results of improved

RELAP5/SCDAP code and Star CCM+. Comparisons and evaluations of RELAP5/SCDAP simulation against transient experiments are given at the end of this chapter.

Chapter VIII summarizes the major results and conclusions of this study as well as recommendations for future works.

2. General Background

2.1 History and Evolution of High Temperature Gas-cooled Reactor

Starting from 1950s, the research and development of HTGRs is to improve the performance of Gas-cooled Reactor (GCRs). Both prototype and demonstration plants have been constructed and operated in several countries. Due to various reasons, after the closure of German THTR-300 in 1989, only two new experimental HTGRs were constructed in Japan and China. Recently, the HTGR technology has received increasing interest in many countries because of its inherent safety features and its ability of cogeneration of heat and electricity.

Prototype and Demonstration HTGRs

A HTGR is typically characterized by fully ceramic (graphite) core internal structure, graphite moderation and helium coolant. The prototype HTGRs include the Dragon Reactor (1966-1975) in the United Kingdom, the Arbeitsgemeinshaft Versuchs Reaktor (AVR, 1968) in Germany and the Peach Bottom Unit 1 (1967-1974) in the United States. The prototype HTGRs demonstrated the viability of the HTGR concept, and provide first source of performance data for coated fuel and material irradiation behavior under elevated temperatures [1].

As the HTGR concept had been proven to be viable, from 1970s to early 1990, larger HTGR plants were constructed to demonstrate the commercial viability of HTGR. FSV in the United States and THTR-300 in Germany were constructed for the above purpose. The thermal power and net electrical output of FSV and THTR-300 was 835MWt/330MWe and 750MWt/300MWe respectively. The reactor performances demonstrate the safety characteristics, durability and other key elements for commercial deployment.

HTGR Research Reactors

Currently, two HTGR test reactors are under active research and development. The High Temperature Engineering Test Reactor (HTTR) designed, constructed and operated by Japan Atomic Energy Research Institute (JAERI) is a 30MW prismatic block type reactor. The construction was started in 1991, and the first criticality was achieved in 1998. In 2001, the full power operation was obtained at a helium outlet temperature of 850°C. In 2004, the high-temperature test operation was obtained at a helium outlet temperature of 950°C.

The Institute of Nuclear Energy Technology (INET) began construction of the HTR-10 in 1995 at Tsinghua University in China. HTR-10 is a pebble-bed type reactor of which the designed outlet temperature ranges from 700°C to 950°C. The initial criticality was achieved in 2000 and was operated in its full power of 10MWt by 2003. These test HTGRs demonstrate and update the technological basis for HTGRs, obtain databases for various irradiation behaviors and high temperature properties of advanced materials and used for innovative research on high temperature technology such as process heat applications.

Near-term HTGRs

The HTGR technology has gained increasing interest in many countries around the world in recent years. The renewed interest is due to the unique inherent and passive safety features of HTGR as well as its potential of cogenerating of electricity and high temperature process heat to produce hydrogen. The technologies are developed along two districted paths based on the type of reactor core, i.e. prismatic-block-type reactor and pebble-bed-type reactor. For both designs, an increase in operation temperature and an interface with hydrogen production system are required in order to meet the Generation IV VHTR design objective.

The prismatic-block-type near-term HTGRs include:

- GTHTR300 (Japan Atomic Energy Agency, Japan)
- GT-MHR (OKBM Afrikantov, Russian Federation)
- MHR-T (OKBM Afrikantov, Russian Federation)
- MHR-100 (OKBM Afrikantov, Russian Federation)
- SC-HTGR (AREVA, United States)

The pebble-bed-type near-term HTGRs include:

- HTR-PM (Tsinghua University, China)
- PBMR-400 (Pebble Bed Modular Reactor SOC Ltd, South Africa)
- HTMR-100 (Economics Trevor Blench STL, South Africa)
- Xe-100 (X-energy, United States)

2.2 High Temperature Gas-cooled Reactor Design

As could be inferred from its name, the key feature of HTGRs is that the reactor is operated at high temperature compared to other reactor designs. HTGR is a helium-cooled, graphite-moderated reactor of which the coolant outlet temperature exceeds 800°C. The reactor could be either a “prismatic-block-type” or a “pebble-bed-type” depending on the form of its fuel elements (shown in Figure 2.1). The characteristics of this type of reactor are summarized as follows:

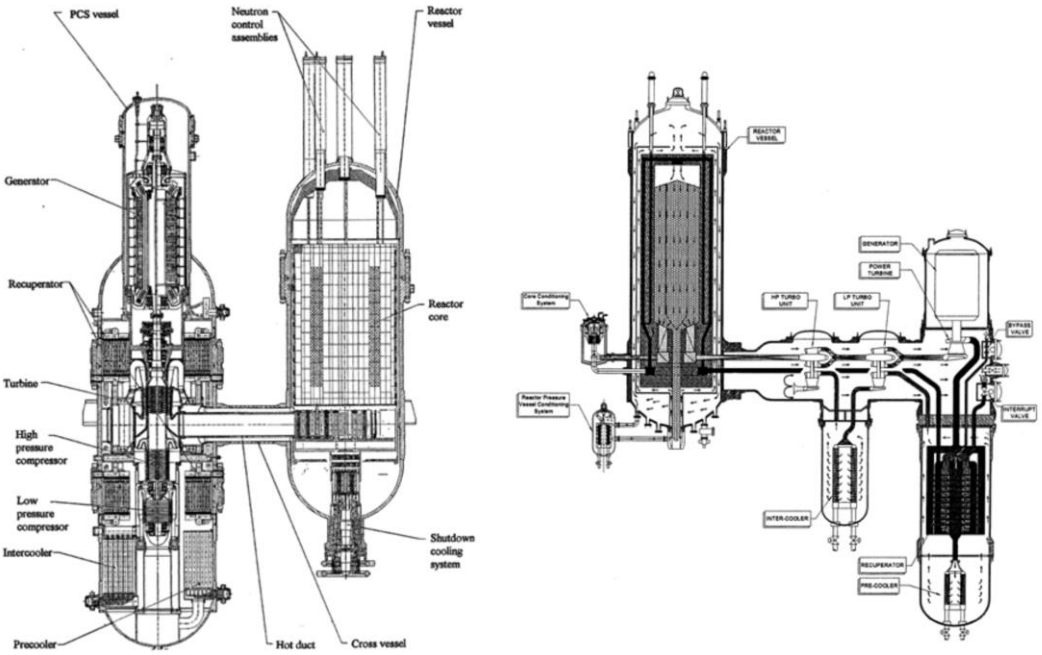

(a) Prismatic-block type reactor [1] (b) Pebble-bed type reactor [2]

Figure 2.1 (a) Prismatic-block type reactor and (b) Pebble-bed type reactor

- The higher operation temperature results in higher thermodynamic efficiency of the plant (Approaching 50% compared to 30%~35% in conventional reactor designs)

- The helium, which works as HTGRs' coolant, is chemically inert to core components.

- The graphite, which is used as moderator and reflector, has large heat capacity. It acts as a thermal barrier that makes the incidental transients very slow.

- The fuel element design, i.e. the multi-coated fuel particles dispersed in a graphite matrix, allows confining radioactive fission products over the full range of operating and accident conditions.

- Following an accident, the reactor could be passively cooled down through conduction, natural convection and radiation heat transfer due to the core geometry and low power density.

2.3 Air Ingress Accident

At present, the most severe accident scenario anticipated for HTGRs is an air ingress accident, following by a postulated guillotine-ended break of main coolant pipe. It starts with helium depressurization, after which air is anticipated to enter the core through the break by molecular diffusion and eventually by natural circulation. The air ingress accident can be categorized into three phases based on the characteristic of phenomena. They are the blow-down phase, the molecular diffusion phase and the natural convection phase [3].

- Blow-down Phase: During blow-down phase, helium will keep discharging out of reactor vessel until the pressures inside and outside reactor vessel are balanced meanwhile the reactor core experiences rapid heat-up.

- Molecular Diffusion Phase: During molecular diffusion phase, due to the air concentration gradient between the reactor vessel and reactor cavity, air in the reactor cavity will enter the reactor vessel by molecular diffusion. The natural circulation is very weak in this phase. Thus graphite oxidation mainly occurs at the bottom of the reactor vessel closed to the break. The fuel temperature is expected to increase at first due to decay heat generation. However, the temperature may cool down later due to the heat removal by conduction and thermal radiation.

- Natural Convection Phase: During natural convection phase, stable global natural circulation will be eventually established inside reactor vessel as a result of gas density difference, which leads to large amount of air ingresses into reactor vessel. Due to the high air-flow rate of global natural circulation, the oxidation reactions will be very active, which leads to rapid fuel temperature increase and excessive graphite components gasification.

Air ingress accident would cause severe consequences including reactor core temperature increase due to exothermic oxidation reactions, mechanical degradation of graphite structures and accumulation of explosive CO gas in the reactor [4].

2.4 Graphite

Overview

Graphite is a crystalline form of carbon. It possesses relatively high heat capacity, thermal conductivity and good mechanical stability under elevated temperatures. The low atomic number and neutron capture cross-section make it a good candidate for neutron moderator. Graphite was used as moderator in several types of reactors including water-cooled reactors, namely, RBMK and EGP-6 (RBMK is a light water-cooled, graphite-moderated Generation II commercial reactor design developed by Soviet Union and EGP-6 is a scaled down version of RBMK reactor design), gas-cooled reactors such as Magnox (CO_2-cooled and graphite-moderated reactor design originated in United Kingdom) and high-temperature gas cooled reactors such as AVR (prototype pebble bed reactor constructed in German in 1960) and HTTR (helium-cooled test reactor under development at JAERI).In HTGRs, graphite is not only used as moderator, but also used as core support components, reflectors and fuel elements (i.e. the triple-isotropic collated fuel particles are dispersed within a graphite matrix to form fuel elements), as a result of its good mechanical performance at high temperature. Moreover, during accidents, graphite components also act as a thermal barrier, which mitigate temperature rises of reactor core.

Nuclear grade graphite

Nuclear grade graphite refers to the graphite that is specifically manufactured for using within a nuclear reactor. Comparing to natural graphite, it possesses high purity to avoid absorption of thermal neutrons and generation of undesirable radioactive species. In addition, for in-core applications, it is required that nuclear grade graphite exhibits acceptable thermal and mechanical properties before and after fast neutron irradiation. There are some historical grades such as H-451 of the USA and Atr-2E of Germany that are no longer manufactured and some new grades of graphite such as NBG-17, NBG-25, PCEA, PPEA, IG-110, IG-430, etc. are under development. Among the listed grades of graphite, IG-110 is used in both HTR-10 and HTTR, which are the only two HTGRs that are currently operating. Table 2.1 shows typical thermo-mechanical properties of IG-110.

Table 2.1 Typical thermo-Mechanical Properties of IG-110 [5]

Producer	Toyo Tanso
Forming Method	Iso-stat.
Source Coke	Petroleum
Bulk Density (g/cm3)(300K)	1.78
Tensile strength (MPa)(300K)	25.3
Compressive Strength (MPa)(300K)	76.8
Young's modulus (GPa)(300K)	7.9
Thermal Conductivity(W/mK) (673K)	80
Grain size (10^{-6}m)	20 (Mean)

Graphite Oxidation

Graphite oxidation could take place during both normal operation and air ingress accident when oxidizing gases present in the system. In general, HTGR reactor core is an inert environment filled with helium that does not chemically react with graphite. However, if there are oxidizing impurities present in the helium coolant gases, even at low concentrations, they may have significant influence on graphite oxidation during the long service time. In postulate accident scenario such as air ingress, excessive air corrosion of graphite would take place which would greatly jeopardize the reactor safety.

2.5 Computational Codes

Two computer codes, i.e. RELAP5/SCDAP and Star CCM+ are used in this study. RELAP5/SCDAP is a one-dimensional system analysis code, designed to estimate the behavior of reactor systems either in normal or accident conditions. It is selected as the main tool for studying the selected graphite oxidation models and correlations. Star CCM+ is a three-dimensional computational fluid dynamic (CFD) code, which is used as a supplemental simulation tool for this study. With a given geometry, initial conditions and boundary conditions, detailed simulations of flow and heat transfer can be obtained using Star CCM+. The simulation results of Star CCM+ and the experimental data are used as RELAP5/SCDAP input for simulating the transient graphite oxidation experiments conducted in this study.

RELAP5/SCDAP

The RELAP5/SCDAP is being developed as part of the international SCDAP Development and Training Program (SDTP) [6]. SDTP consists of nearly 60 program members and licensed software users from universities, research organizations, regulator organizations, etc. all over the world. RELAP5/SCDAP was based on the publicly available RELAP5/MOD3.3 and SCDAP/RELAP5/MOD3.2 developed by the US nuclear Regulatory Commission [6]. It is later improved with advanced programing and numerical methods, user options and advanced models developed by Innovation Systems Software (ISS) and members of SDTP. RELAP5/SCDAP MOD4.0 utilized in this study, is primarily used for developing advanced severe-accident related models and user options. In order to make it easier for program members to develop new models, the code has been currently completely rewritten to FORTRAN 90/95/2000 standards. In this study, selected graphite oxidation models and correlations are incorporated into RELAP5/SCDAP MOD4.0. The code performance was then assessed against heat transfer data from steady state graphite oxidation experiments conducted by various researchers and transient graphite oxidation experiments conducted in present study.

Star CCM+

CD-adapco (Computational Dynamics-Analysis & Design Application Company Ltd), which is best known for its computational fluid dynamic (CFD) products, developed STAR-CCM+ in 2004. STAR-CCM software is an all-in-one solution for multidisciplinary engineering simulation. It is capable of capturing all the relevant physics where multi-scale phenomena involved in physics, chemistry and engineering occur simultaneously [7]. The two major calculation tools involved in present study are computational fluid dynamics (CFD) and conjugate heat transfer (CHT).

CFD makes use of numerical analysis to solve and analyze problems of fluid flows. Computer codes are used to simulate the interaction of liquids and gases with surfaces defined by boundary conditions. The fundamental basis of CFD problems is the Navier-Stokes equations that define single-phase fluid flows. CHT refers to situations in which multiple modes of heat transfer occur simultaneously. For instance, in present study, when gas mixture flowing through an annular graphite pipe, convective heat transfer between the pipe walls and flow, the radiation heat transfer across the inner and outer pipe walls as well as the conduction within the bulk of pipe all take place at the same time. Finite element analysis (FEA) is required for performing the thermal calculation for the solid components, while the flow conditions are kept being estimated and updated by CFD tool. The CHT solution which is embedded in the CFD tool allows the fluid and solid temperatures to be calculated concurrently. This is achieved by 1) a robust coupled solver that simultaneously solves the temperatures of the solid components and the fluid, 2) Prism layer cells generated on the interface of fluid and solid that capture the layer effects and thermal gradients for properly predicting the heat transfer and 3) conformal meshing between the fluid and solid region which ensure accurate heat transfer between two regions without needs for interpolation [8].

3. Theoretical Framework

3.1 Graphite Oxidation Kinetics

The HTGR reactor core consists mainly of graphite. Thus, graphite oxidation should be considered carefully in HTGR safety analysis. The mechanism of graphite oxidation has been studied extensively for decades and it comes to the following conclusion: The chemical reaction between graphite and oxygen can be classified into three basic regimes [9,10] based on temperatures. The oxidation modes of nuclear-grade graphite from regime I to III are shown in Figure 3.1.

Regime I: Chemical kinetic controlled regime

At low temperatures， the graphite oxidation is solely controlled by reaction kinetics. Uniform graphite oxidation occurs as oxygen diffused through the bulk of the graphite specimen. As a result, homogeneous corrosion was observed in graphite specimen, which leads to a decrease of graphite density. It has been reported that the mechanical strength of nuclear grade graphite decreases significantly with density. Specifically speaking, a 50% reduction of mechanical strength is measured for a 7% decrease in density [31]. Although the reaction rate is comparatively low in this regime, after accumulating for days, a considerable amount of graphite oxidation could take place, which could greatly jeopardize the integrity of reactor core. Thus, predicting the oxidation reaction rate and graphite burn-off in Regime I is important in long-term safety examinations.

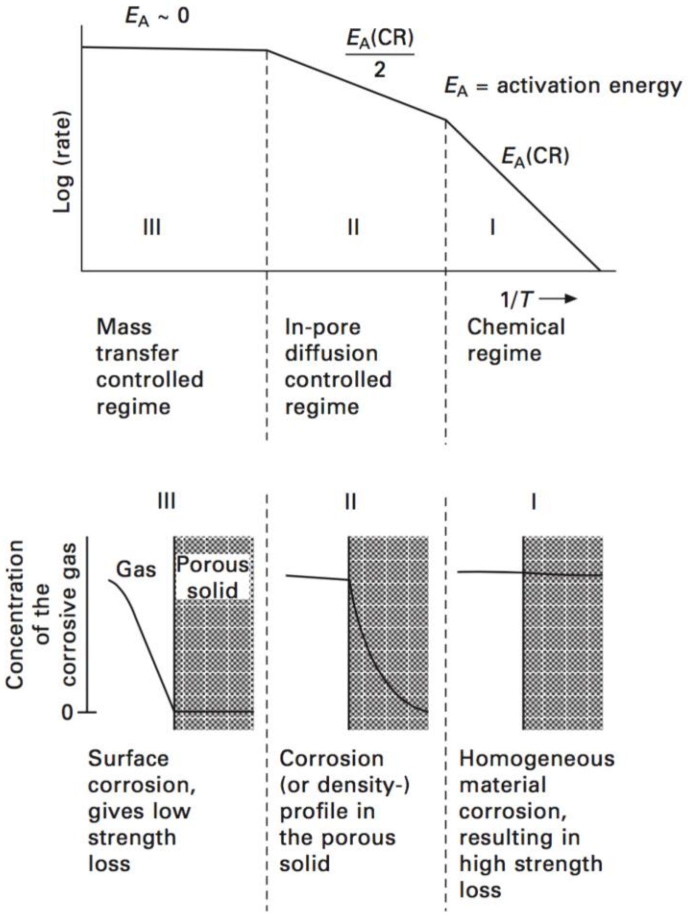

Figure 3.1 Schematics of graphite oxidation regimes [11]

The bulk oxidation of graphite by oxygen in regime I follows an Arrhenius-type law. In addition, it has been found that the regime I reaction rate is strongly dependent on the graphite burn-off, with a maximum value found at 30%~40%. The mechanism was well explained by Fuller and Okoh [30]: When oxidation starts, the surface area of internal pores was low. As oxidation proceeds, the internal poles start to open and connected with each other leading to the generation of additional internal surface area and increasing reaction rate. As oxidation further processes, the pore wall is consumed and collapsed and thus the active reaction area decreases, which explains why the rate starts to decline at ~40% burn-off. The Arrhenius rate equation is given by:

$$r_I = k_v exp(\frac{-E_a}{RT}) P_{O_2}{}^n M(B) \quad [mol \cdot m^{-3} \cdot s^{-1}] \tag{3.1}$$

Where

r_I = Reaction rate

E_a = Activation energy

k_v = Rate constant

n = Order of reaction

P_{O_2} = Partial pressure of oxygen

B = Graphite burn-off

$M(B)$ = Multiplication factor

The graphite burn-off can be defined as:

$$B = \frac{total\ weight\ loss\ of\ graphtie\ during\ oxidation}{original\ weight\ of\ graphtie} \tag{3.2}$$

The multiplication factor $M(B)$ [12] describes how the change of graphite internal surfaces would affect the reaction rate. It varies among graphite grades and could be experimentally determined. Detail expiation on multiplication factor is presented in section 4.1.2.

Regime II: In-pore diffusion controlled regime

At intermediate temperatures, varying contributions of oxygen diffusion through the gaseous boundary layer, diffusion of oxygen into the bulk graphite and the chemical reactivity of graphite affect the oxidation.

At intermediate temperatures, the chemical reactivity of graphite is much higher compared to regime I. Thus, the concentration is kept decreasing while oxygen diffusing into the bulk graphite leading to an oxidation gradient within the specimen. The multi-mechanism makes the reaction rate in this regime hard to be described theoretically.

Regime III: Boundary layer diffusion controlled

At high temperatures, oxygen is consumed immediately at the graphite surface due to high chemical reactivity and the reaction is restricted to the external surface of graphite specimen. However, the oxidation, which depends on the moving flow and surface geometry, does not necessarily to proceed homogenous along the surfaces. The only reaction rate limiting mechanism in regime III becomes the rate at which oxygen can diffuse through the gaseous boundary layer to the graphite surface. Mass transfer rules are applied for determine the reaction rate. Analytical heat transfer solutions have been founded for simple geometry such as pebble and cylinder under certain thermal boundaries conditions, and the mass transfer coefficient can be calculated by applying the heat/mass transfer analogy to convert the heat transfer data to mass transfer data. Nevertheless, some researchers reported that the reaction rates measured in their experiments are higher than the theoretical calculations by up to four times [13].

Boudouard reaction (C/CO_2 reaction) needs to be brought into attention at high temperatures. This reaction leads to graphite corrosion as well as generating toxic and explosive CO gas.

3.2 Mass Transfer

Overview

The following paragraphs briefly introduce the principle of mass transfer and the analogies between mass and heat transfer.

Mass transfer, as could be inferred from its name, is the transport phenomena of mass from one location to another location. When the concentration of a constituent in a system varies from point to point, there is a natural tendency that the constituent would transport from a higher concentration region to a lower concentration region, which explains why mass transfer occurs. There are two fundamental transport modes in mass transfer, namely molecular mass transfer and convective mass transfer. For the previous one, mass is transferred by molecular motion in static fluid, and for the second one, mass transfer happened between a surface and a moving fluid, and the process is aided by the dynamic characteristics of the flow [14]. In our study, we are mostly focusing on the convective mass transfer.

Convective mass transfer

For either laminar or turbulent flow, there is always a layer in which the fluid is laminar and there is no relative motion between the fluid particles and the solid surface. The molecular mass transfer through the stagnant and laminar layer of fluid strongly influences the convective mass transfer. For laminar flow, all the mass transport between the fluid and surface is by molecular means and it is in the direction of concentration decreasing. As for turbulent flow, the mass is also transported by the eddies present within the free stream.

The rate equation for convective mass transfer is given as:

$$N_A = k_c \Delta c_A \tag{3.3}$$

Where:

N_A = Molar mass flux of species A

k_c = Convective mass transfer coefficient

Δc_A = Concentration difference between the boundary surface concentration and the average concentration of the fluid stream of diffusing species A

Two important dimensionless parameters, Schmidt number and Lewis number, are often used to correlate convective mass transport data.

The Schmidt number defined as the ratio of momentum diffusivity to mass diffusivity is analogous to Prandtl number used in convective heat transfer.

$$S_c = \frac{momentum\ diffusivity}{mass\ diffusivity} = \frac{\mu}{\rho D_{AB}} \tag{3.4}$$

Where:

S_c = Schmidt number

μ = Dynamic viscosity of the fluid

ρ = Density of the fluid

D_{AB} = Mass diffusivity

The Lewis number defined as the ratio of thermal diffusivity to mass diffusivity is used to characterize the flowing fluid when convective transfer of mass and energy occur concurrently.

$$L_e = \frac{thermal\ diffusivity}{mass\ diffusivity} = \frac{k}{\rho c_p D_{AB}} = \frac{Sc}{Pr} \tag{3.5}$$

Where:

L_e = Lewis number

k = Thermal conductivity

c_p = Specific heat capacity

Pr = Prandtl number

Another dimensionless number commonly used in mass transfer operation is the Sherwood number (also called the mass transfer Nusselt number). It is defined as the ratio of the convective mass transfer to the rate of diffusive mass transfer.

$$Sh = \frac{convective\ mass\ tranfer\ rate}{molecular\ mass\ tranfer\ rate} = \frac{k_c L}{D_{AB}} \tag{3.6}$$

Where:

Sh = Sherwood number

L = Significant length

Mass/Heat Transfer Analogy

There is a similarity in the differential equations for mass and energy transfer as well as at the boundary where transfer processes are expressed in terms of transport gradient and dimensionless variables. A great deal of effort has been devoted into developing analogies between mass and heat transfer in order to predict similar transport processes from heat transfer data to mass transfer data or vice versa. Since the flow in graphite oxidation experiments is mostly laminar, the discussions regarding mass/heat transfer analogy are mainly focused on such a direction of conversion.

1) Reynolds Analogy

Reynolds postulated that the mechanisms for energy transfer and momentum transfer is identical, i.e. the Prandtl number is unity. By extend the Reynolds postulation to include the mechanism of mass transfer, which is true if Schmidt number is unity, the following expression can be derived:

$$\frac{k_c}{v_\infty} = \frac{h}{\rho v_\infty c_p} \quad or \quad \frac{Nu}{Sh} = \frac{Pr}{Sc} = 1 \tag{3.7}$$

Where:

v_∞ = Velocity of bulk fluid

h = Heat transfer coefficient

ρ = Density of the fluid

c_p = Thermal capacity of the fluid

2) Chilton-Colburn Analogy:

Chilton and Colburn modified the Reynolds' analogy so that there would not have the restrictions that Prandtl number and Schmidt numbers must be equal to 1. They developed the following analogy:

$$\frac{h}{\rho C_p v_\infty} Pr^{2/3} = \frac{k_m}{v_\infty} Sc^{2/3} \quad or \quad \frac{Nu}{Sh} = (\frac{Pr}{Sc})^{\frac{1}{3}} \tag{3.8}$$

Where:

Nu = Nusselt number

Equation (3.8) is valid for gases and liquids in the following ranges:

$$0.6 < Sc < 2500 \; and \; 0.6 < Pr < 100$$

It has been observed that the Chilton-Colburn analogy holds for many different geometries including Flow over flat plate, flow in circular pipe and flow in annulus.[14] Furthermore, for helium, air, nitrogen, oxygen and many other gases, Prandtl number and Schmidt number have similar values (≈0.7) over a wide range of temperature and pressure. Therefore, both Equation (1) and Equation (2) could be used for prediction the mass transfer rate of oxygen to graphite surface during air ingress.

3.3 RELAP5 Thermalhydraulic

3.3.1 Overview of the code

RELAP5/SCDAP was developed at the Idaho National Engineering Laboratory (INEL) for the U.S. Nuclear Regulatory Commission (NRC) for best-estimate transient simulation of light water reactor behavior during severe accident. The code models the coupled behaviors of reactor thermalhydraulic system, the reactor core, the fission product released during severe accident, lost-of-coolant-accident (LOCA), as well as operational transients [15].

The RELAP5/SCDAP package consists of RELAP5 (Reactor Excursion and Leak Analysis Program) and SCDAP (Severe Core Damage Analysis Package). The RELAP5 code models the overall RCS thermalhydraulic, heat realigns or absorbing structures, control system components, reactor point kinetics, non-condensable gas transport, etc. Thermalhydraulic idealization can be created by combining the desire generic component models (i.e. pipe, annulus, junction, pump, heat structure, etc.) and special process models (i.e. form loss, non-condensable gas transfer, etc.). The RELAP5 code is based on a nonhomogeneous and nonequilibrium model for the two-phase system, which is solved by either a semi-implicit or nearly-implicit numerical scheme to permit economical calculation of system transients [15].

The SCDAP code models the behavior of core components during a severe accident. Processes such as fuel rode heat up, radiation heat transfer among core components, fission products release, oxidation and deformation of materials such as zircaloy and stainless steel, collapse of corium, formation of debris can be treated in SCDAP [16].

The exchange of information between SCDAP and RELAP5 occurs at every time step through the medium of common blocks. SCDAP calculates the surface temperate of SCDAP heat structure, the heat transfer to fluid by radiation, release of non-condensable gases, etc. and pass the data to RELAP. Then, RELAP applies the information received from SCDAP to update the coolant conditions, heat /mass transfer coefficient, etc. A summary of the flow of information from SCDAP to RELAP5 and RELAP5 to SCDAP are shown in Figure 3.2 and Figure 3.3. If the success criterion is not met, both SCDAP and RELAP are allowed to run at a smaller time step.

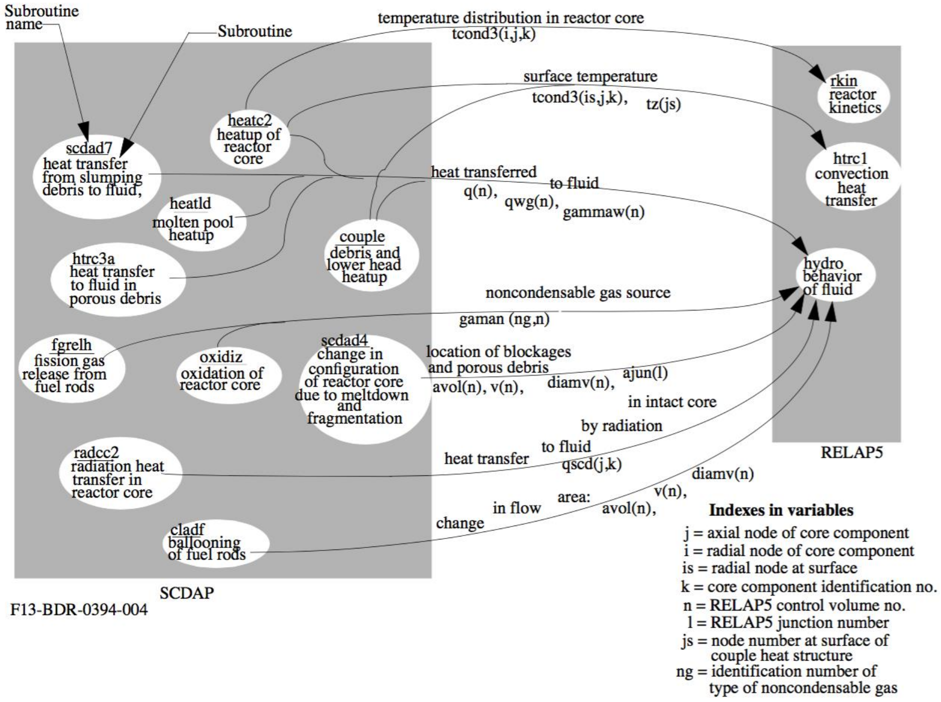

Figure 3.2 Flow of information from SCDAP to RELAP5 [17]

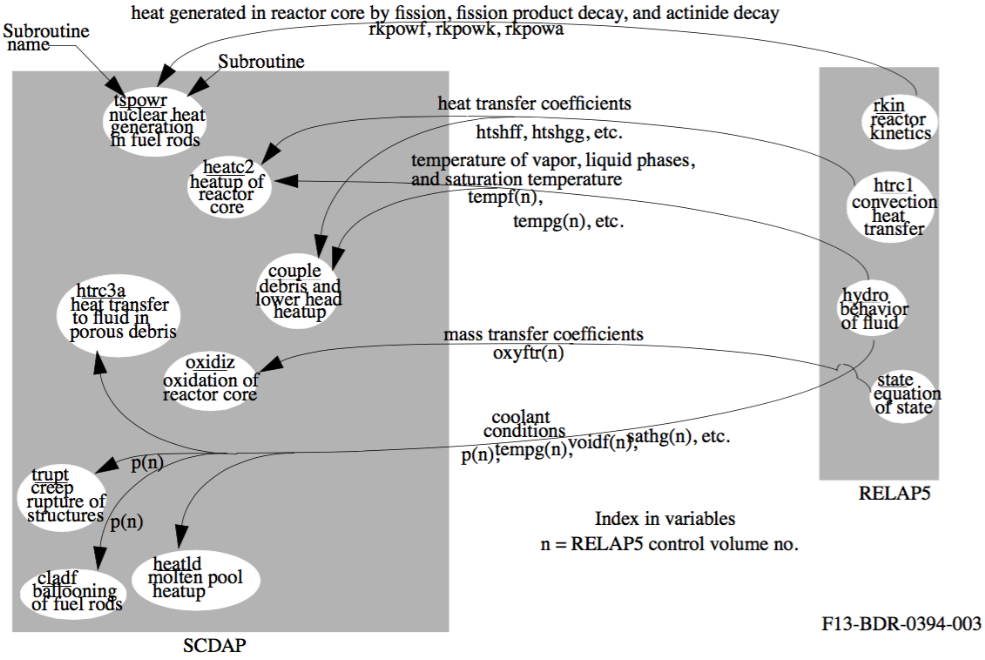

Figure 3.3 Flow of information from RELAP5 to SCDAP [17]

3.3.2 Hydrodynamic model

Mass conservation

Mass can neither be created nor destroyed in non-relativistic reference frames, so it is a conserved quantity in a fluid flow. Within a finite element the rate of change in mass must be the net sum of all mass entering and exiting the element.

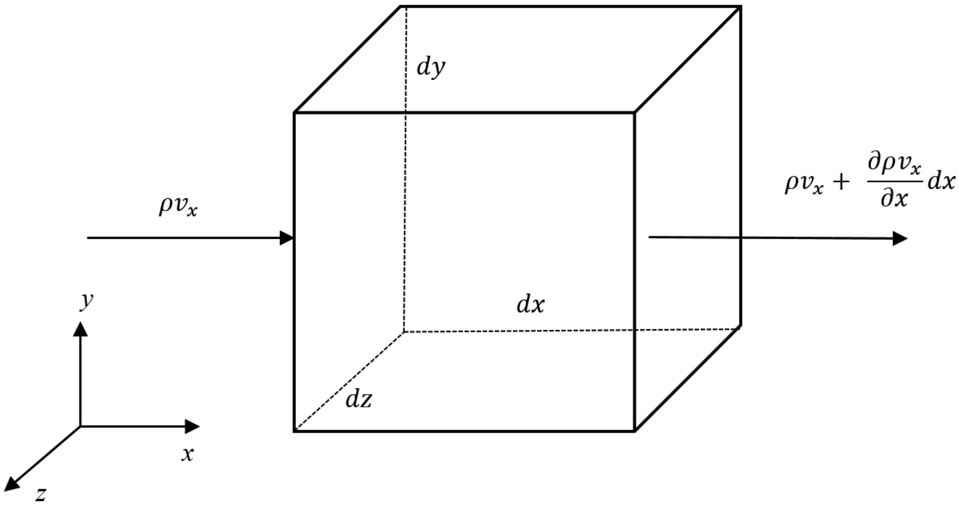

Figure 3.4 Mass flow in x direction

As shown in Figure 3.4, fluid is entering the control volume $dxdydz$ in the x direction with densityρ, velocity v_x and mass flux$\rho v_x dydz$. The mass flux exiting the control volume is $\left(\rho v_x + \frac{\partial \rho v_x}{\partial x} dx\right)(dydz)$. Considering only the x direction, the net accumulation rate of mass in the control volume is:

$$\begin{aligned}\frac{\partial\rho}{\partial t}(dxdydz)|_{v_y=v_z=0} \\ &= \rho v_x(dydz) \\ &-\left(\rho v_x+\frac{\partial\rho v_x}{\partial x}dx\right)(dydz) \\ &= -\frac{\partial\rho v_x}{\partial x}dxdydz\end{aligned} \tag{3.9}$$

Generalizing the one direction description to all directions, we will get the following mass conservation or continuity equation:

$$\frac{\partial\rho}{\partial t}+\nabla\cdot(\rho\boldsymbol{v})=0 \tag{3.10}$$

In RELAP5, each component is often modeled only in one dimension, the corresponding mass continuity equation is:

$$\frac{\partial}{\partial t}(\alpha_g\rho_g)+\frac{1}{A}\frac{\partial}{\partial x}(\alpha_g\rho_g v_g A)=\Gamma_g \tag{3.11}$$

Where

α_g/α_f = Vapor/liquid volume fraction (void fraction)

v_g/v_f = Phasic velocities

ρ_g/ρ_f = Boron densities

Γ_g/Γ_f = Gas/liquid generation terms

Generally, the flow does not include mass sources or sinks, and overall continuity consideration yields the requirement that the liquid generation term be the negative of the vapor generation:

$$\Gamma_g + \Gamma_f = 0 \tag{3.12}$$

In the case of noncondensable components existing in the gas phase, the noncondensable components are assumed to move with the same velocity and have the same temperature as the vapor phase. The additional mass conservation equation for the total noncondensable component is:

$$\frac{\partial}{\partial t}\left(\alpha_g \rho_g X_n\right) + \frac{1}{A}\frac{\partial}{\partial x}\left(\alpha_g \rho_g X_n v_g A\right) = \Gamma_n \tag{3.13}$$

Where

X_n = Total noncondensable mass fraction in the gas phase

M_{ni} = Mass of i-th noncondensable gas

M_n = Total mass of noncondensable gas in the gaseous phase

M_s = Mass of steam in the gas phase

N = Number of noncondensables

Γ_n = Total noncondensable gas generation term

For each noncondensable species the mass conservation equation is:

$$\frac{\partial}{\partial t}\left(\alpha_g \rho_g X_n X_{ni}\right) + \frac{1}{A}\frac{\partial}{\partial x}\left(\alpha_g \rho_g X_n X_{ni} v_g A\right) = \Gamma_{ni} \tag{3.14}$$

Where

Γ_{ni} = Gas generation of each noncondensable species

Momentum conservation

Within the control volume $dxdydz$, the momentum change rate is affected by flux of fluid into and out of the volume and by forces acting on the volume. The effect of fluid flux on momentum could be described mathematically in a similar way as the mass continuity equation. Body forces that act on the entire volume and surface forces that are either normal or tangential to the surfaces of the volume are the two kinds of forces acting on the volume. Generally, the momentum conservation equation is:

$$\frac{\partial}{\partial t}(\rho \boldsymbol{v}) + \nabla \cdot (\rho \boldsymbol{v})\boldsymbol{v} = -\nabla P + \nabla \cdot \boldsymbol{\tau} + \rho \boldsymbol{g} \tag{3.15}$$

Where

v = Velocity vector

τ = Stress tensor

P = Pressure

g = Gravitational vector

In RELAP5, with some assumptions and simplifications, two one-dimensional momentum equations are applied in the hydrodynamic model, one for the vapor phase and the other one for the liquid phase.

$$\begin{aligned}\alpha_g\rho_g A\frac{\partial v_g}{\partial t}+\frac{1}{2}\alpha_g\rho_g A\frac{\partial v_g^2}{\partial x} &= -\alpha_g A\frac{\partial P}{\partial x}+\alpha_g\rho_g B_x A\\ &- (\alpha_g\rho_g A)FWG(v_g)\\ &+ \Gamma_g A(v_{gI}-v_g)\\ &- (\alpha_g\rho_g A)FIG(v_g-v_f)\\ &- C\alpha_g\alpha_f\rho_m A[\frac{\partial(v_g-v_f)}{\partial t}+v_f\frac{\partial v_g}{\partial x}\\ &- v_g\frac{\partial v_f}{\partial x}]\end{aligned} \tag{3.16}$$

Where

B_x = Body force

FIG = vapor phase interface frictional drag

FIF = liquid phase interface frictional drag

FWG = vapor phase wall friction drag

FWF = liquid phase wall friction drag

In our case, there are only noncondensable gases, so the properties of the gas phase are mixture properties of the noncondensable mixture.

Energy conservation

Within the control volume $dxdydz$, the energy change rate is the net sum of energy carried into and out of the volume with the fluid flow, net heat transfers into the volume, all work done by body forces and surface forces and other energy sources and sinks within the volume. The momentum conservation equation is:

$$\frac{\partial}{\partial t}(\rho U)+\nabla\cdot(\rho U)\boldsymbol{v} = -\nabla\cdot P\boldsymbol{v}+\nabla\cdot(\boldsymbol{\tau}\cdot\boldsymbol{v})+\boldsymbol{v}\cdot\rho\boldsymbol{g} -\nabla\cdot\boldsymbol{Q}'+Q'' \tag{3.17}$$

Where

U = Specific internal energy

τ = Stress tensor

P = Pressure

g = Gravitational vector

Q' = Heat flux into and out of the volume which may include head conduction and radiation

Q'' = Internal generation of energy.

In RELAP5, with some assumptions and simplifications, the two phasic thermal energy equations used by the hydrodynamic model are:

$$\begin{aligned}\frac{\partial}{\partial t}(\alpha_g\rho_g U_g)+\frac{1}{A}\frac{\partial}{\partial x}(\alpha_g\rho_g U_g v_g A) &= -P\frac{\partial\alpha_g}{\partial t}-\frac{P}{A}\frac{\partial}{\partial x}(\alpha_g v_g A)+Q_{wg}\\ &+Q_{ig}+\Gamma_{ig}h_g^{*}+\Gamma_w h_g'\\ &-Q_{gf}+DISS_g\end{aligned} \tag{3.18}$$

$$\frac{\partial}{\partial t}(\alpha_f\rho_f U_f)+\frac{1}{A}\frac{\partial}{\partial x}\left(\alpha_f\rho_f U_f v_f A\right)$$
$$=-P\frac{\partial\alpha_f}{\partial t}-\frac{P}{A}\frac{\partial}{\partial x}\left(\alpha_f v_f A\right)+Q_{wf} \tag{3.19}$$
$$+Q_{if}+\Gamma_{ig}h_f^*+\Gamma_w h_f'+Q_{gf}+DISS_f$$

Where

Q_{wg}/Q_{wf} = Phasic wall heat transfer rates per unit volume

Q_{ig}/Q_{if} = Interface heat transfer terms

h_g^*/h_f^* = Associated with bulk interface mass transfers

$DISS_g/DISS_f$= Sums of wall friction and pump effects.

Q_{gf} = Sensible heat transfer rate per unit volume. This is the heat transfer at the noncondensable gas-liquid interface.

Again, since there are only noncondensable gases in our case, the properties of the gas phase are mixture properties of the noncondensable mixture.

Closure relationship

Besides the conservation equations introduced above, some additional relationships (closure equations) such as heat transfer within solids, heat transfer to fluids, wall fiction, equation of state, etc. are needed to be solved with conservation equations either concurrently or iteratively. Heat conduction within solids and heat transfer to fluids will be described in Section 3.3.3. Equation of state is presented below.

The final closure of the conservation equations and the constitutive relationships are the inherent physical properties of the vapor/liquid, and in our case, they are the properties of non-condensable gases. In RELAP5, the non-condensable gases are treated as ideal gases. The non-condensable state equations are:

$$P_iV_i = R_iT_g \tag{3.20}$$

$$U_i = \begin{cases} U_0 + C_0T_gT_g < T_0 \\ U_0 + C_0T_g + \frac{1}{2}D_0(T_g - T_0)^2T_g \geq T_0 \end{cases} \tag{3.21}$$

Where

P_i =Partial pressures of an individual non-condensable components

U_i = Internal energy of an individual non-condensable components

V_i = Specific volumes of an individual non-condensable components

T_g = Temperature of the non-condensable gases

T_0=250K

The $U_{0,ni}$, $C_{0,ni}$, $D_{0,ni}$ used by RELAP is listed in Table 3.1. The values of the constant were determined by the method of least squares using values from varies papers and reports [18].

Table 3.1 Values of $U_{0,ni}$, $C_{0,ni}$and $D_{0,ni}$ for various non-condensable gasses

Non-condensable Gas	R_i(J/kg · K)	$U_{0,ni}$ (J /kg)	$C_{0,ni}$ (J/kg · K)	$D_{0,ni}$ (J/kg · K^2)
Oxygen	8314.3/32.000	1641.42	639.8541	0.3537302
Carbon Monoxide	8314.3/28.010	14231.1	693.2758	0.3421647
Carbon Dioxide	8314.3/44.010	-41467.2	658.7377	0.7563373

3.3.3 Heat structure model

Heat structures in RELAP5 are designed to calculate the heat transferred across solid boundaries of hydrodynamic volumes. Main modeling capabilities of heat structures include fuel pins or plates heated by nuclear or electrical energy, heat transfer across steam generator tubes and heat transfer from pipe and vessel walls.

One-dimensional heat conduction in rectangular, cylindrical, or spherical geometry is used to represent heat structures. To convert the unit surface of the one-dimensional calculation to the actual surface of the heat structure, surface multipliers are used. Thermal conductivities and volumetric heat capacities of different materials could be provided in tabular or functional forms either from build-in or user-supplied data.

Finite difference method is used in the heat conduction calculation. The spacing, material and the internal heat source may vary over each mesh interval. The time-dependence of the heat source can be provided by reactor kinetics, tables of power versus time or a control system variable.

The integral form of the heat conduction equation is

$$\begin{aligned}\iiint C_{p,V}(T,\boldsymbol{x})\frac{\partial T}{\partial t}(T,\boldsymbol{x})dV \\ = \iint k(T,\boldsymbol{x})\nabla T(T,\boldsymbol{x})\cdot d\boldsymbol{s} \\ + \iiint S(\boldsymbol{x},t)dV\end{aligned} \tag{3.22}$$

Where

k = Thermal conductivity (W/m/K)

s = Surface (m^2)

S = Internal heat source ($\mathrm{W/m^3}$)

t = Time (sec)

T = Temperature (K)

V = Volume ($\mathrm{m^3}$)

x = Space coordinate in the x-axis(m)

$C_{p,V}$ = Volumetric heat capacity ($\mathrm{J/m^3/K}$)

Either symmetry or insulated boundary conditions could be described by one of the following methods: a heat transfer correlation package, tables of surface temperature versus time, heat transfer rate versus time and heat transfer coefficient versus time or surface temperature.

3.3.4 Radiation model

The Stefan-Boltzmann law gives the radiation intensity from an object in terms of its temperature:

$$P = A\varepsilon\sigma T^4 \tag{3.23}$$

Where

P = Total power radiated from an object

A = Surface area of the object

ε = Emissivity

σ = Stefan-Boltzmann constant that equals to $5.6704400 \times 10^{-8} J/sm^2K^4$

T = Absolute temperature of the object

The radiation model in RELAP5 calculates the radiant heat exchange among the surfaces of reactor components (i.e., fuel rod, prismatic block, side reflector, RPV, etc.). A set of surfaces, among which the radiant energy is communicated is called an enclosure. Each component surface forms one side of the enclosure and the radiation heat flux equation of each surface describes its radiation heat exchange with all existing surfaces within the enclosure (including itself if it radiates to itself). The computation method is a lumped-system approximation and all the surfaces of the enclosure are assumed to be opaque, diffuse and gray. The assumptions of these methods are as follows [18]:

- The fluid in the enclosure does not emit, absorb, or scatter radiation. i.e., it is a nonparticipating medium that is completely transparent to the thermal radiation.
- The reflectance from a surface is neither a function of incident or reflected direction nor of radiation frequency. i.e., the surfaces are diffuse and gray.
- Temperature, reflectance, and radiosity are constant over each surface.

The radiosity over a surface is the total radiant energy leaving a surface (i.e., the emitted energy and the reflected energy.). The radiosity over a surface can be expressed as:

$$R_i A_i = \varepsilon_i \sigma T_i^4 A_i + \rho_i \sum_{j=1}^{n} F_{ij} R_j A_j \tag{3.24}$$

Where

R = radiosity

A = surface area

ε = emissivity

σ = Stefan-Boltzmann constant

T = temperature

ρ = 1 –ε; reflectivity

F_{ij} = view factor from surface j to i

The net rate of radiation heat transfer from a surface i is the difference between the radiation leaving the entire surface i and the radiation incident on entire surface i, which is expressed as:

$$Q_i A_i = R_i A_i - \sum_{j=1}^{n} F_{ij}\, R_j A_j \tag{3.25}$$

Where

Q_i = net heat flux

The radiation alters the conduction solution boundary condition to:

$$\mathrm{k}\frac{\partial \mathrm{T}}{\partial \mathrm{r}}\bigg|_i = h_i(T_i - T_r) + Q_i \tag{3.26}$$

Where

k = surface conductivity

r = radius

h = convective heat transfer coefficient

T_r = reference temperature

4 Literature Review

4.1 Experimental Studies on Graphite Oxidation

4.1.1 Overview

Given the importance of graphite oxidation in HTGR severe accident analysis, it is crucial to develop models and rate correlations and then incorporated them into computer codes so that important processes such as temperature transient of graphite structures, graphite burn-off, etc. can be predicted and analyzed. The main purpose of this section is to finalize the proper models and correlations for nuclear grade graphite IG-110 after reviewing and discussing the relevant experimental studies and four commonly used system analysis codes.

Before looking into details about models and correlations, we need to firstly figure out what chemical reactions occur during air ingress accident. As depicted in Figure 4.1 the most important chemical reactions is the heterogeneous reaction called graphite oxidation. Other reactions occurring during air ingress include CO combustion which is a homogeneous reaction and Boudouard reaction which is a heterogeneous reaction. The chemical equations are listed as follow:

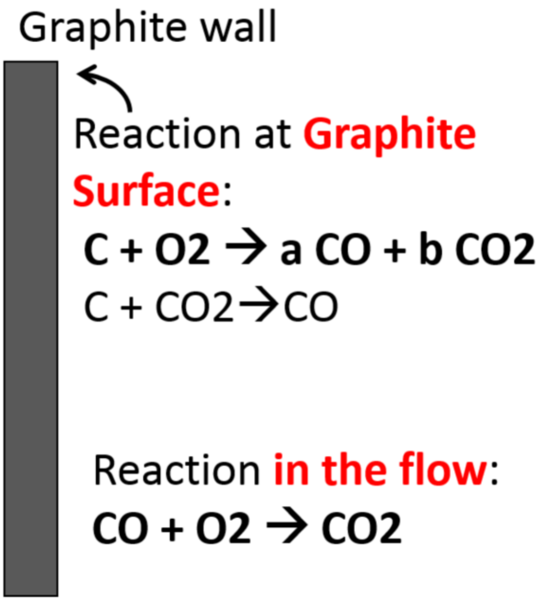

Figure 4.1 Chemical reactions during air ingress

1) Graphite Oxidation:

$$C + O_2 \rightarrow CO_2 \quad + 3.953 \times 10^5 J/mol$$

$$C + \frac{1}{2}O_2 \rightarrow CO \quad + 1.100 \times 10^5 J/mol$$

2) Boudouard Reaction:

$$C + CO_2 \rightarrow 2CO \quad - 1.725 \times 10^5 J/mol$$

3) CO combustion:

$$CO + \frac{1}{2}O_2 \rightarrow CO_2 \quad + 2.830 \times 10^5 J/mol$$

Among the three chemical reactions, graphite oxidization is the dominant reaction during air ingress. The mechanism of graphite oxidation has been studied intensively and there are many correlations available. Graphite oxidation reaction is considered in all system analysis codes used for HTGR accident analysis. Boudouard reaction has very small reaction rate compared to graphite oxidation. It is reported that the reaction rate of Boudouard reaction is fairly small at low and intermediate temperatures and it only needs to be brought into attention at high temperature regime. CO combustion occurs when H_2O presents in the system and its reaction rate is sensitive to moisture fraction. CO combustion should not be neglected when temperature excesses 850°C. Boudouard reaction and CO combustion have been implemented to some but not all system analyses codes that are capable of simulating HTGR air ingress accident.

In the following paragraphs, the above three chemical reactions will be reviewed one by one in the manner of 1) Experimental studies 2) Reaction rate equations used in system analysis codes and 3) Summaries. This review covers four most commonly used system analysis code for HTGR analysis, which are GAMMA, MELCOR, RELAP5-3D and TINTE. The chemical reactions modeled in these codes are summarized in Table 4.1.

Table 4.1 Chemical reaction in system analysis codes

Code	**Graphite oxidation**	**CO combustion**	**Boudouard reaction**
GAMMA	√	√	√
MELCOR	√	√	×
RELAP5-3D	√	×	√
TINTE	√	√	√

4.1.2 Graphite oxidation

Experimental studies

The mechanism of the homogeneous reaction between graphite and oxygen has been studied by various researchers for decades. The chemical equation is written as:

$$C + a_1 O_2 \rightarrow a_2 CO + a_3 CO_2$$

A common conclusion has been that graphite oxidation, according to its mechanisms can be classified into three regimes, namely, the chemical kinetics controlled regime, the in pore diffusion controlled regime and mass transfer controlled regime [19,20,21].

This has been introduced in section 3.1 in detail. In this section, we are going to qualitatively discuss issues regarding rate equation that obtained from various experimental studies for simulation purposes. The following issues are going to be discussed in this section:

1) Equilibrium production ratio of CO and CO_2
2) Activation energy, order of reaction and pre-exponential coefficient in Arrhenius rate relation
3) The dependency of reaction rate on burn-off in low temperature regime
4) Correlations used for mass transfer

<u>1) Equilibrium production ratio of CO and CO_2</u>

The chemical equilibrium between CO and CO_2 is temperature dependent. At high temperatures (~1050K), the chemical reaction rate is very fast and thus the concentration of O_2 at the graphite surface is very low. As there is not enough oxidant, graphite oxidation mainly produce CO. Meanwhile at lower temperature, the generation of CO_2 is dominant. The correlation of the production ratio of CO and CO_2 can be expressed in the following Arrhenius type relationship:

$$f_{CO/CO_2} = \frac{a_2}{a_3} = K_1 exp(-\frac{E_1}{RT})\ (mol/mol) \tag{4.1}$$

Where:

K_1 = Pre-exponent coefficient

E_1 = Activation energy

There are many reports available regarding the production ratio. Rossberg et al. (1956) [22] calculated the production ratio by oxidizing two electrode carbons over the temperature range of 520˚C and 1420˚C. Hinssen et al. (1983) [23] proposed another set of values obtained from the oxidation of nuclear grade graphite A3-3 at temperature ranges from 680˚C to 930˚C. Takahashi et al. (1994) [24] proposed the values for IG-110 and PGX over temperature ranging from 989K to 1310K. And recently, Kim et al. (2006) [25] derived the K_1 and E_1 for IG-110 in the temperature ranges from 700˚C to 1500˚C. The values proposed by different researchers are summarized in Table 4.2.

Table 4.2 K_1 and E_1 in CO/CO$_2$ production ratio correlation

Correlation	$\boldsymbol{K_1}$	$\boldsymbol{E_1}$	**Remarks**
Rossberg	1995 7244	59860 78300	Electrode carbon
Hinssen	500 116	50377 38537	A 3-3
Takahashi	10000	71200	IG-110
Kim	7396	69604	IG-110

The reported constants various in a wide range of value since the production ratio is depended on experimental conditions such as the catalytic effect of impurities within the graphite. In addition, different grades of graphite are also expected to have different $\mathrm{K_1}$ and $\mathrm{E_1}$. In present study, the correlation developed by Kim was adopted for the following reasons:

- It is developed for IG-110 over a wide temperature range
- It agrees well with Takahashi's data (also performed for IG-110)

2) E_a, n and K_0 pre-exponential coefficient in Arrhenius rate relation

For code implementation, several graphite oxidation models are available. Lim and NO. (2003) [26] proposed an Arrhenius correlation that is applicable for oxidation regime II. It was extrapolated down to regime I for calculation in low temperatures. For high temperatures, a rate limit is applied based on the diffusion of oxygen through the boundary layer. Luo Xiaowei et al. (2004) [27] pointed out that Arrhenius relationship could be used to describe the temperature dependence of oxidation behavior in both regime I and regime II, as long as different sets of pre-exponential coefficient and activation energy are used. Kim and NO. (2007) [25] proposed a reaction rate correlation that covers the entire temperature range of HTGRs. In their proposal, the Arrhenius equation is used to calculate the internal pores' reaction rate term and a general mass transfer model is applied for calculating the external surface reaction rate term. Based on the similarities between the parallel electrical circuit and graphite oxidation, two terms were combined, yielding a new correlation that can be applied to calculate the total reaction rate. In addition, the effects of burn-off on reaction rate had been investigated, experimentally determined and added to their correlation. However, there are several issues regarding the currently available models, which are:

- The constants of Arrhenius rate equation
- Burn-off effect on reaction rate
- Temperature limits for each regime

There are many previous reports regarding the constant values of activation energy (E_a), order of reaction (n) and pre-exponential coefficient (K_0). Various sets of constant have been proposed by researchers based on their individual measurement data. However, at a given temperature, reaction rates predicted by different correlations greatly differ from each other. The explanations include: First, correlations proposed by various researchers were developed for different grades of graphite and the differences between graphites are too significant to be ignored. And second, some correlations were developed for intermediate temperature regime but extrapolated to regime I and regime III. Naturally, when comparing, say, the regime I reaction rate with correlation developed for corresponding temperatures, the extrapolated correlation would predict a higher reaction rate.

The burn-off effect was curial for reaction rate in regime I and also have influence on regime II reaction rate. Yet, the dependency of reaction rate on burn-off has been ignored by most correlations. This detailed discussion about this issue is addressed in the next section.

The temperature limits for each regime have been discussed in several studies. Hinssen et al. (1983) [23] gave the following temperature limits for each regime: regime I: T<500˚C; regime II: 500˚C<T<900˚C; regime III: T>900˚C. Blanchard et al. (2003) [28] suggested another classification where regime II is defied from 600˚C to 900˚C. El-Genk et al. (2013) [29] mentioned that at low Reynolds number, regime III begins to affect the graphite oxidation at low temperatures (~700˚C). O'Brien et al. (1988) [21] pointed out that the temperature limits was affected by the density, impurity, microstructure and the size of the graphite specimen. All the above studies suggest that the transition temperature cannot be explicitly given and it could be a dynamic parameter depending on the flow condition (Reynolds number). Thus, it would be better if the rate correlation can smoothly transit from one regime to another without imposing transition temperature.

3) The dependency of reaction rate on burn-off

At low temperature regime, there is a strong dependence of reaction rate on graphite burn-off. The mechanism of it has been explained in Section 3.2. Luo Xiaowei et al [27] measured the oxidation rate of IG-11 with time and found out that the reaction rate first increases and then decreases with time. Fuller et al. [30] and Kim et al. [69] measured the oxidation rate as a function of burn-off for IG-110 over a wide range of values

(Fuller 0%-100%; Kim 0%-65%). Both measurements show that the maximum reaction rates for IG-110 were found at 30%-40% burn-off (Figure 4.2).

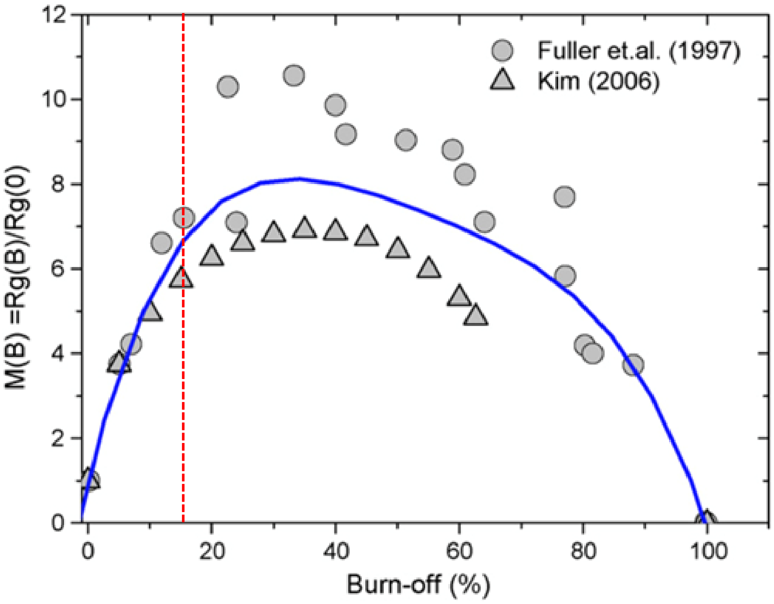

Figure 4.2 Variation of reaction rate with burn-off [12]

Even though there is not a big concern about burn-off during high temperature accident like air ingress, burn-off occurring at low temperature is crucial in long-term safety examinations since it could largely compromise the structural integrity of graphite components in HTGRs. It was reported that the compressive strength of graphite is reduced by half at 10% burn-off. [31] Over 15% burn-off, the graphite is too fragile to support the reactor. Thus, for HTGR safety analysis, we are mainly concerned with graphite burn-off from 0% to 15%. Yet, as shown in Figure 4.2, within the range of interest, the multiplication factor as a function of burn-off can only be retrieved from 5 data points. During simulations, the error introduced by using limited data points could be accumulated over large number of iterations resulting in significant deviation from actual cases.

4）Correlations used for mass transfer

The mass transfer rule and how mass flux could be calculated by adopting the heat and mass transfer analogies are introduced in section 3.2. For graphite oxidation experiments, researchers tend to choose geometries and flow conditions of which the convective heat transfer correlation is well-known, or even better, one with analytical solution. An example would be the Graetz problem where fluid flows in a circular tube when the wall of the tube is heated at a uniform temperature and the fluid enters the tube at a different uniform temperature with fully developed laminar velocity profile. The geometry (i.e. circular tube), flow condition (fully developed laminar flow at a uniform temperature) and the heating condition (uniform wall temperature) can be easily recreated in experiments. It is found that for Greatz problem, the local Sherwood number is a constant (=3.66) for fully developed region. When considering the entrance effect, the averaged Sherwood number over the total tube length can be expressed as [32]:

$$Sh = 3.66 + \frac{0.0668\left(\frac{d}{x}\right)(Re \cdot Sc)}{1 + 0.04 \cdot \left[\left(\frac{d}{x}\right) \cdot (Re \cdot Sc)\right]^{\frac{2}{3}}} \tag{4.2}$$

Where:

d = Hydrodynamic diameter of the tube

x = Total length of the tube

The reaction rate derived from the above correlation matched well with Kim et al.'s measurements. Ogawa et al. [4] adopted the same method for calculating the reaction rate and reported that the mass transfer was over-predicted by 20%. But, for some researchers who conducted graphite oxidation experiments at low Reynolds number (Re<30), they reported that in order to match with the graphite oxidation rate measurements, they used a Sherwood number an order of magnitude lower than that given by Equation (4.2)[29].

For more general cases, where analytical solutions are intractable, Sherwood number is directly derived from Nusselt number by adopting the mass/heat transfer analogy, which is:

$$\frac{h}{\rho C_p v_\infty} Pr^{2/3} = \frac{k_m}{v_\infty} Sc^{2/3} \tag{4.3}$$

For gases such as helium, air, oxygen, etc., the Prandtl number and Schmidt number have similar value of 0.7, Equation (4.3) can be simplified to:

$$\frac{h}{\rho C_p v_\infty} = \frac{k_m}{v_\infty} \tag{4.4}$$

Graphite oxidation rate equations used in system analysis codes

The models and correlations used in TINTE, RELAP-3D, INL-MELCOR and GAMMA are summarized in Table 4.3.

Table 4.3 correlations used in system analysis code

Code	Graphite Oxidation Model	Remarks
TINTE	Reaction rate: $R\left(\frac{\text{kg}}{\text{m}^3\text{hr}}\right)=720\exp\left(-\frac{1.614\times 10^4}{\text{T}}\right)P_{O_2}$ CO/CO_2 production ratio: 0.0	1. $C+O_2 \rightarrow CO_2$ 2. Rose et al. (1994)[33] 3. Pebble-bed reactor

RELAP-3D (2003)	Reaction rate: 395<T<1248: $R_1\left(\frac{\mathrm{kg}}{\mathrm{m}^2\mathrm{s}}\right)=0.2475\exp\left(-\frac{5710}{\mathrm{T}}\right)$ 1448<T<2073K: $R\left(\frac{\mathrm{kg}}{\mathrm{m}^2\mathrm{s}}\right)=\min(R_2,R_m)$ $R_2\left(\frac{\mathrm{kg}}{\mathrm{m}^2\mathrm{s}}\right)=0.0156\exp\left(-\frac{2260}{\mathrm{T}}\right)$ $R_m\left(\frac{kg}{m^2s}\right)=M_ck_mC_{O_2,\infty}$ Where: $\frac{k_m}{v_\infty}=\frac{h}{\rho C_p v_\infty}$ CO/CO_2 production ratio: 0.0	1. C+O2→ CO2 2. Oh et al. (2001)[34]
INL-MELCOR	Reaction rate: $\mathrm{R}=\min(R_1,R_2,M_cC_{O_2,\infty})$ $R_1\left(\frac{kg}{m^2s}\right)=1.57\times10^6\exp\left(-\frac{1.88\times10^5}{\mathrm{RT}}\right)\left(\frac{P_{O_2}}{0.209\times10^5}\right)^n$ $n=0.5\sim1.0$ $R_2\left(\frac{kg}{m^2s}\right)=M_ck_m\frac{2f_{CO/CO_2}+2}{f_{CO/CO_2}+2}C_{O_2,\infty}$ Where: $k_m=\left(\frac{3.66\times D_{gO_2}}{d_h}\right)\left(\frac{S_c}{P_r}\right)^{\frac{1}{3}}$ CO/CO2 production rate ratio:	1. $C+O_2\rightarrow CO+CO_2$ [22] 2. Lim & NO et al. (2003) [35] 3. IG-110; electrode carbon

	$f_{CO/CO_2} = 1995exp(-59860/RT)$	
GAMMA	Reaction rate: $\frac{1}{R_{tot}}=\frac{1}{R_I}+\frac{1}{R_{III}}$ $R_I = 2.552 \times 10^6 exp(-\frac{2.18 \times 10^5}{RT})\, P_{O_2}{}^{0.75} M(B) \times V$ $R_{III} = M_c \frac{2f_{CO/CO_2}+2}{f_{CO/CO_2}+2} k_m (C_{O_2,\infty} - C_{O_2,0}) A$ Where: $\frac{k_m}{v_\infty} Sc^{2/3} = \frac{h}{\rho C_p v_\infty} Pr^{2/3}$ CO/CO$_2$ production ratio: $f_{CO/CO_2} = 7396exp(-69604/RT)$	1. C+O2→ CO+CO2 [22] 2. Kim & NO et al. (2008)[12] 3. IG-110

Summaries: graphite oxidation

As shown in Table 4.3, INL-MELCOR and GAMMA model the graphite oxidation considering the chemically equilibrium between CO and CO$_2$ while in TINTE and RELAP-3D, it is assumed that the oxidation reaction goes completely to CO$_2$. The correlations adopted by INL-MELCOR and GAMMA were developed for IG-110. In INL-MELCOR, the correlation is applicable for regime II, therefore, when extrapolated it to a lower temperatures of regime I, INL-MELCOR would provide a conservative estimation by over-predicting the reaction rate. The correlations adopted by GAMMA combine the internal pores' reaction rate term and a general mass transfer model to achieve smooth regime transfer. The effects of burn-up on reaction rate at low temperatures were also considered.

4.1.3 CO combustion

Experimental studies

The gas-phase homogenous reaction mechanism of CO combustion in the present of H2O is well established. The chemical equation is written as:

$$CO + \frac{1}{2}O_2 \rightarrow CO_2$$

Dryer et al. [36] studied the CO combustion reaction in the present of water at atmospheric pressure and temperature ranging from 1030K to1230K, equivalence ratio ranging from 0.04 to 0.5 and water concentration ranging from 0.1% to 3.0%. On the basis of experimental data, the following over-all rate expression can be expressed as (the equation was converted into SI units):

$$R_{Dryer} = 2.24 \times 10^{12}\, exp\left(-\frac{167400}{RT_g}\right) \tag{4.5}$$

$$R_{CO} = -R_{Dryer} \times \rho_{CO} \times (\frac{\rho_{O_2}}{M_{O_2}})^{0.25} (\frac{\rho_{H_2O}}{M_{H_2O}})^{0.5} \ \ (kg/m^3 s) \tag{4.6}$$

Where:

T_g = Temperate of the bulk fluid

ρ_i = Density of species *i*

M_i = Molecular mass of species *i*

Another popular rate equation was proposed by Howard et al. [37] by summarizing the experimental data of 14 individual studies that covering the temperature range of 840K to 2360K. The rate equation is expressed as:

$$R_{Howard} = 1.3 \times 10^{8}\, exp\left(-\frac{126000}{RT_g}\right) \tag{4.7}$$

$$R_{CO} = -R_{Howard} \times \frac{\rho_{CO}}{M_{CO}} \times (\frac{\rho_{O_2}}{M_{O_2}})^{0.5}(\frac{\rho_{H_2O}}{M_{H_2O}})^{0.5}\ \ (mol/m^3s) \tag{4.8}$$

Dryer's and Howard's rate equations have different activation energy and order of reaction in oxygen. In fact, there is a considerable debate as to order in oxygen, of which the value was reported from 0 to 1. Since Howard obtained the rate equation by looking into various researchers' data, an averaged value of 0.5 was used in their rate equation. Meanwhile, the order of reaction in oxygen of Dryer's equation was obtained from their individual measurements. Both rate equations have been adopted for simulating the effects of chemical reactions during air ingress. For instance, Takeda et al. [38] used Howard's rate equation while studying the phenomena of molecular diffusion and natural convection in multicomponent gas system during air ingress. Ogawa et al. [4] conducted a graphite oxidation experiment and pointed out that the activation energy given by Howard did not match their experimental data where CO mole fraction decreased at 950°C due to CO combustion, however, a rate equation of higher activation energy like Dryer's predicted the turn-around-point of CO mole fraction very well. FLUENT also uses Dryer's rate equation to calculate CO combustion.

CO combustion rate equations used in system analysis codes

Since the reaction rate of CO combustion cannot be ignored from intermediate temperate (~850°C), CO combustion is taken into consideration by all four system analysis codes.

Both GAMMA and MELCOR adopt Dryer's rate equation for calculating CO combustion:

$$R_{GAMMA} = -2.24 \times 10^{12}\, exp\left(-\frac{167400}{RT_g}\right) \times \rho_{CO} \times (\frac{\rho_{O_2}}{M_{O_2}})^{0.25} (\frac{\rho_{H_2O}}{M_{H_2O}})^{0.5} \ \ (kg/m^3s) \tag{4.9}$$

$$R_{MELCOR} = -2.24 \times 10^{12}\, exp\left(-\frac{167400}{RT_g}\right) \times \rho_{CO} \times (\frac{\rho_{O_2}}{M_{O_2}})^{0.25} (\frac{\rho_{H_2O}}{M_{H_2O}})^{0.5} \ \ (kg/m^3s) \tag{4.10}$$

The rate equation used in TINTE is:

$$R_{TINTE} = -1.3 \times 10^{20} exp(-\frac{144000}{RT_g}) \times \frac{\rho_{CO}}{M_{CO}} \times (\frac{\rho_{O_2}}{M_{O_2}})^{0.5} (\frac{\rho_{H_2O}}{M_{H_2O}})^{0.5} \ \ (mol/m^3s) \tag{4.11}$$

Summaries: CO combustion

The activation energy, order of reaction and pre-exponential coefficient of CO combustion rate equations are summarized in Table 4.4.

Table 4.4 Constants used in CO combustion

E_a(kJ)	K_0	n_{CO}	n_{O_2}	n_{H_2O}	Developer/User
167.4	2.24×10^{12}	1	0.25	0.5	Dryer/GAMMA, MELCOR
126.0	1.3×10^{8}	1	0.5	0.5	Howard/Takeda et al.
144.0	1.08×10^{22}	1	0.5	0.5	TINTE

When temperature exceeds ~850°C, the effect of moist CO combustion cannot be ignored. Among the rate equations available, Dryer's rate equation seems to be the most reliable one for the following two reasons:

1) It was chosen by several computer codes including system analysis code such as GAMMA, MELCOR and CFD code like FLUENT.

2) It was reported that rate equation with higher activation energy like Dryer's could predict the trend of CO concentration better compared with those of lower activation energy [4].

4.1.4 Boudouard Reaction

Experimental studies

The reaction of graphite and CO_2 is called Boudouard reaction. This reaction leads to corrosion of graphite structures and generation of explosive CO gas. The chemical equation is written as:

$$C + CO_2 \rightarrow 2CO$$

Unlike the previous two reactions, Boudouard reaction didn't gain much attention from researchers due to its low reaction rate at low and intermediate temperatures. One experiment study regarding Boudouard reaction was carried out by KAIST in 2004[69] for experimental determination of the reaction rate by gas analysis method. The graphite used in the experiments is IG-110. The experiments were carried out in the temperatures ranging from 700˚C to 1500˚C and at the CO_2 mole fraction between 5% and 20%. On the basis of experimental data, KAIST concluded that：

1) The reaction rate follows the Arrhenius-type law. The active energy is 255 kJ and the order of reaction is 0.9. The reaction remains in the chemical kinetics-limited regime up to 1500°C.

2) Compared to temperature, CO_2 concentration has little effect on reaction rate.

3) The reaction rate of Boudouard reaction is approx. 3% compared to the reaction rate of graphite oxidation at 1400°C and both reaction rates would not be comparable until temperature exceeds 2000°C.

4) The following rate equation was proposed based on their measurements with RMS error of ±5%.

$$R_{KAIST} = 3950 \exp\left(\frac{-295000}{RT}\right) P_{CO_2}{}^{0.9} \left(\frac{kg}{m^3 s}\right) \tag{4.12}$$

Where:

P_{CO_2} = Partial pressure of CO_2

T = Temperature of the graphite wall

In addition, the reaction rate of NBG-17 has been experimentally determined using thermo gravimetric analysis by Schlögl B (2009) [39]. The experiments were carried out at temperatures ranging from 1150°C to 1450°C at 10%, 20% and 100% CO_2 mole fraction. Based on the measurement data, Schlögl concluded that:

1) Similar to graphite oxidation, Boudouard reaction also goes through three regimes. For NGB-17, under their experimental conditions, regime II is in the temperature range of 1175C to 1275C.

2) The active energy of NGB-17 in regime II is 202±1% kJ

3) The rate equation could be written in Langmuir-Hinshelwood-type law as:

$$R_{Schl\ddot{o}gl} = -\frac{625exp(-\frac{5000}{T})P_{CO_2}}{1-0.231exp(\frac{30000}{T})P_{CO_2}{}^{0.5}}\ (mol/m^2s) \tag{4.13}$$

Boudouard rate equations used in system analysis code

The Boudouard reaction has been implemented into TINTE, GAMMA and RELAP-3D. For GAMMA, the reaction rate of graphite A3-3 (Moorman et al 1984 [40]) was added since data for IG-110 was not available at that time. The rate equation used in GAMMA is:

$$R_{GAMMA} = \frac{0.145exp(\frac{-25000}{T})P_{CO_2}}{1+3.4\times10^{-5}exp(\frac{7000}{T})P_{CO_2}{}^{0.5}}\ (kg/m^2s) \tag{4.14}$$

In RELAP-3D, the calculation of Boudouard reaction starts at 1420K. The same rate equation developed by Moorman et al. [40] is used in RELAP-3D.

$$R_{RELAP-3D} = \frac{0.145exp(\frac{-25000}{T})P_{CO_2}}{1 + 3.4 \times 10^{-5}exp(\frac{7000}{T})P_{CO_2}{}^{0.5}}\ (kg/m^2s) \tag{4.15}$$

The rate equation (mol/m^3s) adopted by TINTE is [41]:

$$R_{TINTE} = \frac{2.2 \times 10^8 \exp\left(\frac{-35800}{T}\right) CGR \times 0.012 \times C_w(CO_2)}{1 + 8.1 \times 10^{-6} \exp\left(\frac{17000}{T}\right) \left(C(CO)\right)^{0.5} + 179\, exp\left(-\frac{9820}{T}\right) C_w(CO_2)} \tag{4.16}$$

Where:

CGR = Density of nuclear graphite in mole/m^3

$C_w(CO_2)$ = Concentration of CO$_2$ on the solid wall in mole/m^3

$C(CO)$ = Concentration of CO in the boundary layer of solid wall

Summaries: Boudouard reaction

The rate correlations given by different researchers have different units, some are in kg/s-m3 while others are in kg/s-m2. Not knowing the original geometries of the graphite specimens used in different experiments makes it very difficult to qualitatively compare the rate correlations. However, one thing that could be confirmed is that different grades of graphite have different Boudouard reaction rate. At the same temperature, some grades of nuclear graphite such as A3-3 have higher reaction rate than others and thus needed to be taken into consideration at lower temperature (~1000°C). Nevertheless, for IG-110 which is what we are primarily interested in, KAIST's measurement shows that at 1400°C, the Boudouard reaction rate is only 3% compared to the graphite oxidation reaction rate indicating that Boudouard reaction may not be a big concern when analyzing the effects of chemical reactions on IG-110 graphite component during air ingress below 1400°C.

4.1.5 Conclusions

After reviewing the literatures on the chemical reactions that take place during air ingress, the following reactions and correlations are finalized to be incorporated in RELAP5/SCDAP for analysis of HTGR severe accidents. The detailed information is given in Table 4.5.

Table 4.5 Correlations used to improve RELAP5/SCDPA

Chemical Reactions	Chemical equation	Correlations
Graphite Oxidant	$C + O_2 \rightarrow CO_2 + CO$	**Reaction rate (kg/s):** $\frac{1}{R_{tot}} = \frac{1}{R_I} + \frac{1}{R_{III}}$ $R_I = 2.552 \times 10^6 exp(-\frac{2.18 \times 10^5}{RT})\, P_{O_2}{}^{0.75} M(B) \times V$ $R_{III} = M_c \frac{2f_{co/co_2} + 2}{f_{co/co_2} + 2} k_m C_{O_2,\infty} A$ *Where:* $\frac{k_m}{v_\infty} Sc^{\frac{2}{3}} = \frac{h}{\rho C_p v_\infty} Pr^{\frac{2}{3}}$ *or* $k_m = \frac{D_{O_2,mix}}{d}(3.66 + \frac{0.0668\left(\frac{d}{x}\right)(Re \cdot Sc)}{1 + 0.04 \cdot \left[\left(\frac{d}{x}\right) \cdot (Re \cdot Sc)\right]^{\frac{2}{3}}})$

		CO/CO$_2$ production ratio: $f_{CO/CO_2} = 7396exp(-69604/RT)$ **Chemical Heat:** $H_{CO} = 1.1 \times 10^5 J/mol$ $H_{CO_2} = 3.95 \times 10^5 J/mol$
CO Combustion	$CO + O_2 \rightarrow CO_2$	**Reaction rate (kg/m^{3}s):** $R = -2.24 \times 10^{12}\, exp\left(-\frac{167400}{RT_g}\right) \times \rho_{CO} \times (\frac{\rho_{O_2}}{M_{O_2}})^{0.25}(\frac{\rho_{H_2O}}{M_{H_2O}})^{0.5}$ **Chemical Heat:** $H_{CO_2} = 2.83 \times 10^5 J/mol$
Boudouard Reaction	$C + CO_2 \rightarrow CO$	**N/A**

The above correlations are selected for the following reasons:

Graphite Oxidation Reaction:

1) The correlations were developed for IG-110, which is the grade of graphite concerned in present study.

2) The chemical equilibrium between CO and CO$_2$ is considered; The CO/CO$_2$ production ratio was also developed for IG-110.

3) The effect of burn-off has been concerned. However, the dependency of reaction rate on burn-off was derived from very limited experimental data, which needs to be improved before code implementation.

4) The rate correlation allows smooth regime transition. There is no necessity to impose transition temperatures.

5) Two mass transfer correlations are included; one is for Graetz problem, which is the condition various graphite oxidation experiments were conducted at. The other is the Chilton-Colburn heat/mass transfer analogy, which can be applied for more general cases.

CO Combustion Reaction:

1) The Dryer correlation selected for RELAP5/SCDAP improvement has been adopted for various codes, including FLUENT which is a famous CFD code as well as INL-MELCOR and GAMMA, which are two system analysis codes commonly used for HTGR analysis.

2) It was reported that rate equation with higher activation energy like Dryer's could predict the trend of CO concentration better compared with those of lower activation energy.

Boudouard reaction:

Boudouard reaction is not incorporated in RELAP5/SCADP. Because, for IG-110, it was reported that the reaction rate of Boudouard reaction is very low compared to that of the graphite oxidation reaction at temperature under 1400℃.

4.2 Graphite Emissivities and Measurement Methods

4.2.1 Overview

One important inherent safety feature of HTGR is that after accidental events, the reactor has the ability to be cooled down entirely by passive heat transfer mechanisms, which are conduction, thermal radiation and natural convection. Among these processes, conduction and natural convection vary linearly with temperature while radiation, according to the Stefan-Boltzmann equation, varies with the fourth power of temperature, making it the main heat transfer mode, particularly when temperatures are above ~700°C.

The material property that dictates its effectiveness in emitting radiant heat is emissivity, which is defined as the ratio of the thermal radiation from a surface to the thermal radiation of a black body surface at the same temperate. In core design, a conservative emissivity value of 0.8 is adopted for calculating the radiation heat transfer across the gap between the fuel rod and the wall of coolant channel [42].

From experimental point of view, emissivity is a dynamic surface property, which generally depends on temperature, wavelength and emission angle. It may also vary depending on the surface roughness, porosity of material's surface, degrees of oxidation, grain size, etc. As a result, for HTGR safety analysis, it is crucial to measure the emissivity of a particular nuclear grade graphite of interest (e.g. IG-110, NGB-17) under conditions representative to their intended application environment. The present study mainly concerns massive air ingress accident, during which graphite components would experience temperature transients and excessive corrosion (oxidation). Therefore, emissivity measurement experiments were conducted to understand the evolution of thermal emissivity of nuclear grade graphite (IG-110) at accidental temperatures before and after oxidation.

4.2.2 Measurement methods

Emissivity measurement can be generally classified into two categories that are calorimetric and radiometric methods. The calorimetric method, as could be inferred from its name, involving heating up a specimen at a given power. And then emissivity of the specimen can be calculated from the heat balance between heat input and heat removal (i.e. radiation heat transfer) [43]. If the specimen was heated up with a laser, then the emissivity at the wavelength of the laser can be determined [44] For the radiometric method, the emissivity of a specimen is determined by measuring its radiation using a pyrometer [45], spectroscope [46], radiometer [47] or Fourier Transform Infrared spectrometer [48]. If the emissivity is obtained by comparing the radiation emitting by a specimen to that of a blackbody, it is called direct radiometric measurement. If the transmissivity and reflectivity of a specimen are measured, and the emissivity is calculated from the Kirchhoff's law, then the emissivity is measured with indirect radiometric method. If the emissivity at selecting wavelength is needed, then interferential filters [49], monochromators or spectrographs [50] could be applied to achieve narrow wavebands. Otherwise, the emissivities in a wide spectral range can be measured by FTIR spectrometer. The blackbody spectrum can be obtained by a commercial blackbody or theoretical calculation. An important feature of emissivity measurement is to heat up and maintain the specimen temperature. If the specimen is a conductor, it could be heated up by Joule heating. Meanwhile, if the specimen does not conduct electricity, it could be heated up by contact (e.g. cartridge heater) or radiation heaters (e.g. furnace). The most crucial and difficult part in emissivity measurement is to determine the temperature of measuring area where blocking is not allowed. If temperature distributes uniformly within the specimen, then a contact sensor can be mounted beside the measuring area, inside or at the rear of the specimen. Otherwise, noncontact temperature sensor such as radiometer should be adopted. However, the emissivity, which is the value to be measured, needs to be previously provided to the measurement instrument.

The most state-of-the-art method for determining the normal spectral emissivity utilizes measurements of radiant from both the material of interest and that of a blackbody at the same temperature with identical optical paths connecting the specimen/blackbody to an FTIR spectrometer. This method allows high temperature measurements and can provide the most reliably emissivity measurements over the widest spectral range [50，51]. However, this kind of emissivity measurement system (Figure 4.3 [52]) is fairly complex and thus takes great effort to design, construct and calibrate.

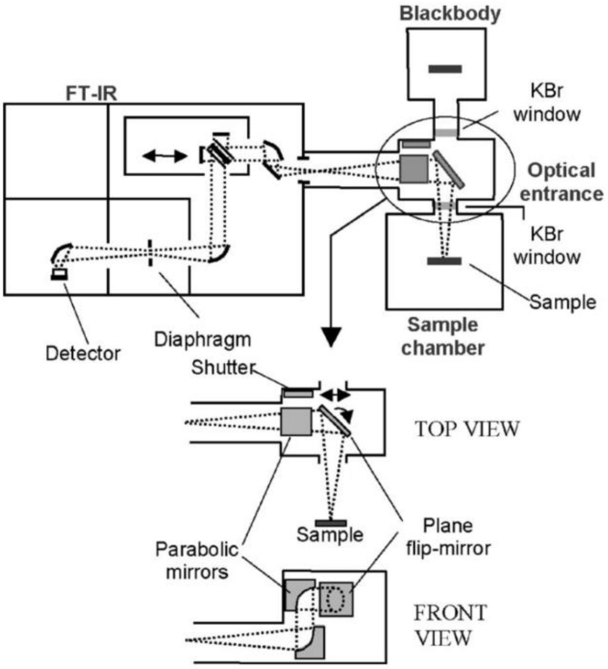

Figure 4.3. Schematic of an emissivity measurement facility consisting of sample chamber, blackbody, optical path and FTIR spectrometer [52]

4.2.3 Graphite emissivity

Several studies have been performed to measure the spectral and total emissivity of commercial graphite at elevated temperatures in 1960s [53,54] It's reported that the graphite emissivity, ranging from 0.95 to 0.70 [55], slightly decreases with increasing temperature [54]. However, it was pointed out that the decreasing trend might be an error due to temperature gradients between the location where surface radiance was measured and the location where the temperature was independently estimated. According to the reflectance measurements performed by M.R. Null et al., graphite emissivity is independent of temperature up to 3000°C [56] Figure 4.4 and Figure 4.5 show the total emissivity and spectral emissivity of graphite measured by Neuer.G in 1998 [57] The total emissivity of graphite remains at 0.87 while temperature increases from 950°C to 1300°C. A wavelength dependency of the graphite spectral emissivity could be confirmed in Figure 4.5. The emissivity decreases from 0.95 to 0.82 when the wavelength increases from 0.6um to 9um.

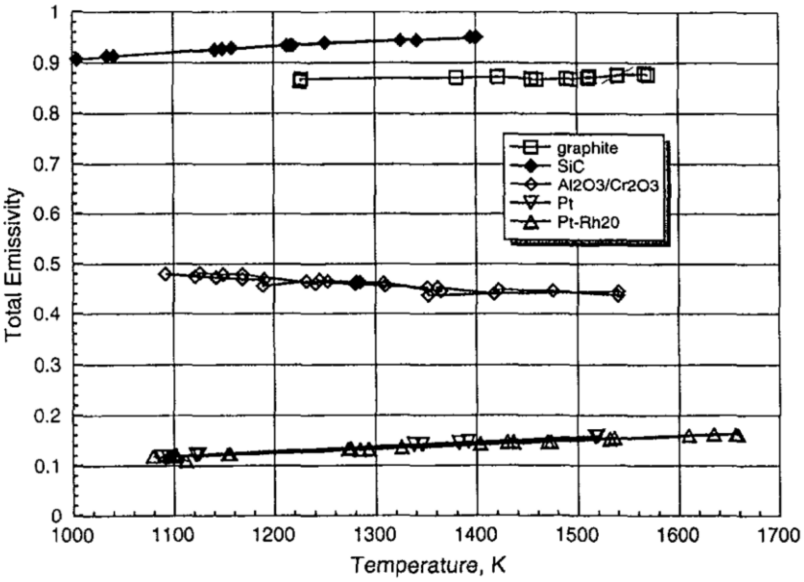

Figure 4.4 Total normal emissivity of graphite (hollow square) [57]

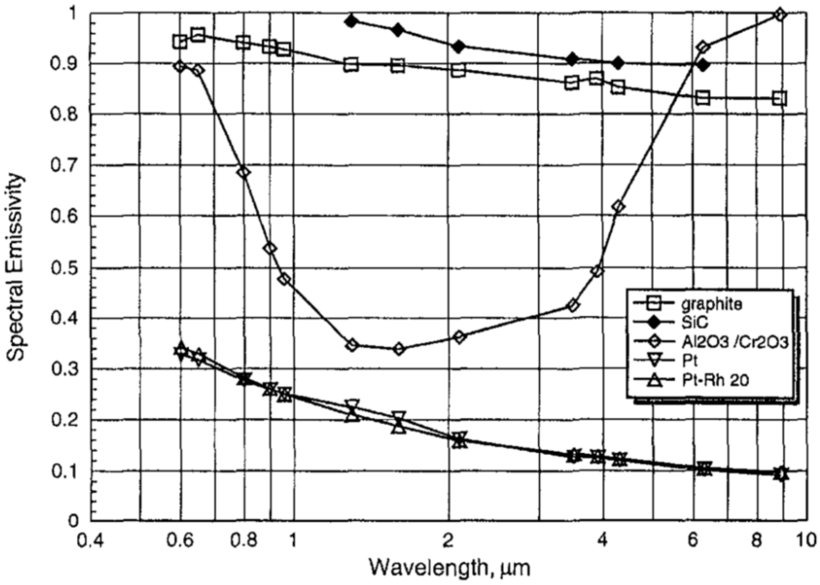

Figure 4.5 Spectral emissivity of graphite (hollow square) [57]

Wang. F et al. (2014) [58] investigated the effects of surface roughness on the emissivity of graphite. The experiments were conducted in the wavelength region from 5.5um to 17um at temperatures from 1000°C to 1600°C. The experiment results show that, firstly, the normal emissivity of graphite increased evidently with surface roughness. Secondly, the directional emissivity of graphite barley changed within a detection angle ranges from 0-60, i.e. the specimen can be treated as diffuse surface.

Nowadays, there are many commercial grade graphites being developed and manufactured. Apparently, the emissivities of different graphite grade are also different and thus, it is necessary to specify for which commercial grade graphite the emissivities were measured. According to Kostanovskii.A.V et al., the spectral normal emissivity (0.65um) of MPG-7 grade graphite is 0.87 [59] in temperature ranges from 2700K to 3000K while for DE-24 grade graphite, the values are 0.84-0.85 [60] in the same temperature range. The emissivities of several nuclear grade graphites (IG-110, PCEA, IG-430 and NBG-18) at various oxidation degrees in temperature ranges from 100°C to 500°C have been investigated by Seo. S. K et al [61,62,63] A far infrared ray was used for the measurement. The experiment results confirmed that different nuclear grade graphites have different emissivity behaviors. The author concluded that firstly, the graphite emissivity decreases with increase in temperature. Secondly, the graphite emissivity increases with increasing oxidation degrees. Lastly, the changes in density, porosity, crystallinity and surface structure are responsible for the increase in emissivity after oxidation. Specificity for IG-110, the emissivity decreases from 0.68 at 100°C to 0.56 at 500°C. Meanwhile for 10% oxidized IG-110 sample, the emissivity was 0.835 at 100°C and 0.675 at 500°C.

4.2.4 Conclusions

The method for measuring emissivity at high temperature is kept evolving in the last several decades. Nowadays, there are facilities that could perform spectral emissivities measurement in a wide spectral range with better accuracy. However, the number of the facilities is very limited and the technology is mainly utilized in measuring the emissivity of metals and alloys. For graphite, especially for the new grades of nuclear graphite, very few emissivity measurements were performed.

The focus of this study was to improve HTGR safety analysis in an event of air ingress. And the emissivity of graphite is required by all safety analysis codes to compute the radiation heat transfer. An emissivity value of 0.8 is adopted by many codes for conservative estimations. However, in order to improve the accuracy of calculation, acquiring the actual emissivity of a specific grade of graphite, both before and after oxidation, is necessary.

In present study, in order to verify whether emissivity of 0.8 is conservative for air ingress accident analysis as well as providing a range for sensitivity analysis, an emissivity measurement was conducted. The grade of graphite used in this study is IG-

110 since it has been used for both HTR-10 and HTTR, which are the only two HTGRs that are currently operating.

5. Emissivity Measurement

5.1 Apparatus and experimental conditions

In this study a direct optical method is applied to measure the normal spectral emissivity (λ=1.55μm) of IG-110 specimen before and after oxidation over a temperature range of 500℃ to 1000℃.

Figure 5.1 shows a cross sectional drawing of the essential parts of this test set-up. The apparatus mainly consists of sealed chamber, electrodes, thermocouple, IG-110 specimen, infrared thermometer, power supply and data acquisition system. The internal faces of the chamber were coated using a black paint of 0.94 emissivity. During the experiment, the chamber was filled with argon.

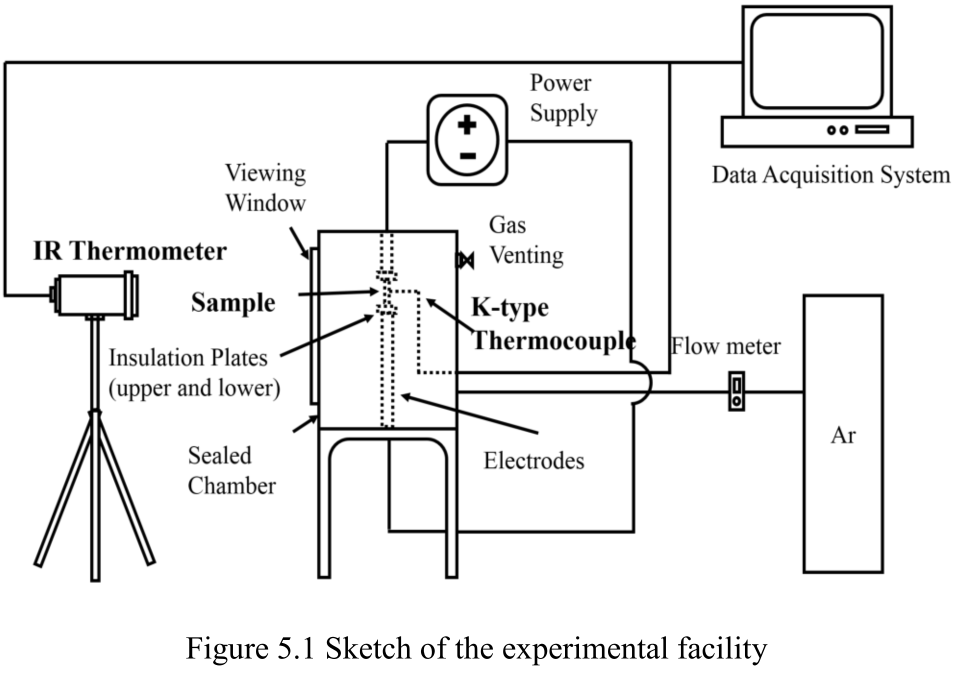

Figure 5.1 Sketch of the experimental facility

As shown in Figure 5.2, the specimen was mounted between two electrodes within the chamber and was heated by Joule heating from a current passing through it. The temperature of the specimen was controlled using a power supply. A k-type thermocouple was used to measure the specimen temperature. The thermocouple was installed in a hole drilled in the middle of the rear side of the specimen. Since the depth of the hole almost but not penetrates the specimen, it is assumed that the reading of the thermocouple can be interpreted as the external surface temperature of the specimen. An inferred thermometer is installed outside the sealed chamber, measuring the external surface temperate of the specimen on the front side through the observation window. The infrared thermometer (IR-CZQH7T) used for this study has a single-band working mode (λ=1.55μm) that measures the temperature ranging from 500℃ to 3500℃, with an accuracy of ±5°C. The measuring distance between the infrared thermometer and the sample is 40cm. With a 200 field-of-view (FOV), the target spot size is 2mm, which is approx. 20% of the specimen diameter.

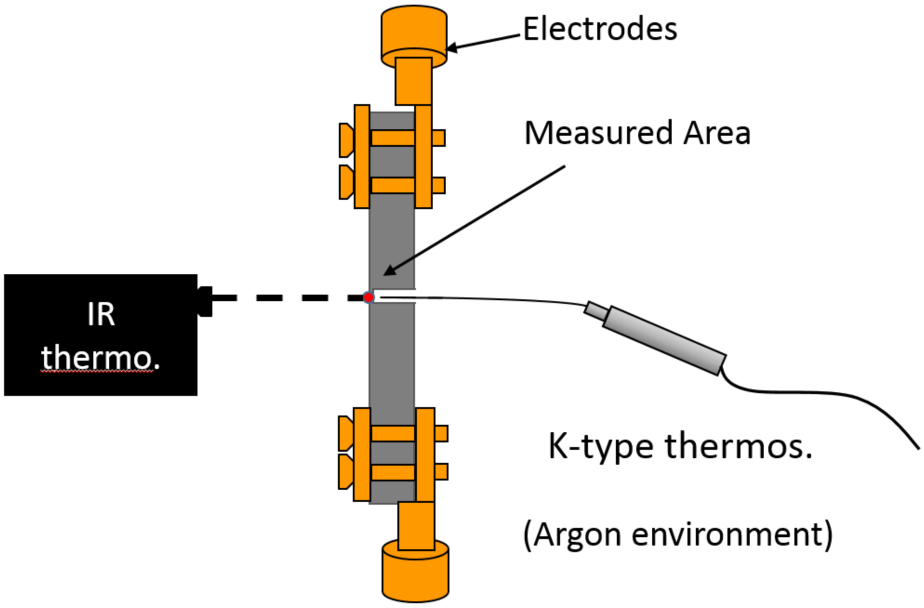

Figure 5.2 sketch of the emissivity measurement section

The specimen used in this study is depicted in Figure 5.3. The specimens were machined into rectangular bars of which the length, width and height were 10mm, 10mm and 30mm respectively. An alignment mark was imprinted on the front surface of the specimen without blocking the measurement area.

Figure 5.3 IG-110 specimen

To obtain a desired oxidation degree, the samples were preheated in an argon environment and then quickly oxidized by air at the chosen air-flow rate of 1.0 SLPM while the specimen temperature held constant at 900˚C.

Table 5.1 provides a brief summary of the specimen used in present study.

Table 5.1 Properties of the specimen

Grade	IG-110	
Size	10×10×30 mm	
Degree of Oxidation (weight loss)	--	$0.00\ g/cm^2$
	$T_{graphite} = 900^{\circ}C$ 1.0 SLPM air, 15 minutes	$0.273\ g/cm^2$

5.2 Experimental procedure

The experiment is divided into a pretest and a main test. Pretest is performed to exam the reliability of IR thermometer and see how ambient environment affects the measurements. The main test is to measure the normal spectral emissivity of IG-110 specimens before and after oxidation at temperature range from 500˚C to 1000˚C.

Before proceeding the experiment, the IR thermometer is pretested to find out if accurate and reliable readings can be provided. The procedure of checking the reliability of the IR thermometer is comparing the IR thermometer readings of a blackbody standard with its emissivity provided by the manufacturer. If it is sensitive to the ambient conditions such as the background radiation of the chamber, the presence of the observation window or the presence of certain components of the atmosphere, this kind of comparison will detect the error.

The experimental protocol used for the pretest can be summarized as follow:

1) To create a blackbody standard, the IG-110 sample is coated with a matte black paint the emissivity of which is 0.94.

2) Preheat the apparatus for half an hour and set the emissivity setting to 1.0.

3) Inject argon into the test chamber at 1.0 SLPM

4) When the oxygen concentration of the chamber drops below 0.5%, heat up the sample to target temperatures.

5) Record the readings of IR thermometer when the reading of k-type thermocouple is 600˚C, 700˚C, 800˚C and 900˚C.

6) Increase the argon flow rate to 10.0 SLPM

7) Heat up the specimen to a target temperature

8) Quickly open the observation window, record the reading of IR thermometer, and closed the window

9) Reduce the specimen temperature to 500 ˚C

10) Repeat step 7to step 9 at 600˚C, 700˚C, 800˚C and 900˚C

11) Calculate the emissivity with the following expression:

$$\varepsilon = \frac{e^{\frac{hc}{\lambda k_B T_k}} - 1}{e^{\frac{hc}{\lambda k_B T_{ir}}} - 1} \tag{5.1}$$

Where:

h = Plank constant

c = Speed of light in vacuum

k_B = Boltzmann constant

λ = Wavelength of infrared thermometer $(i.e. 1.55\mu m)$

T_{ir} = Temperature reading of the IR thermometer

T_k = Temperature reading of the k-type thermocouple

For the main test, the normal spectral emissivity measurements are focused in temperature ranges of 500˚C to 1000˚C. The experimental procedure is similar to that of the pretest (From step 2 to step 5). Specimens of two oxidation levels (i.e. 0.0g/cm2 and 0.0273g/cm2) were prepared. The experimental conditions of the pretest and main test are summarized in Table 5.2.

Table 5.2 Experimental conditions of the pretest and main test

	Pretest	**Main test**
Specimen	Black paint coated non-oxidized	Non-oxidized (0.0 g/cm2) Oxidized (0.0273g/cm2)
Temperature	600˚C~900˚C	500˚C~1000˚C
Argon flow rate	1.0/10.0 SLPM	1.0SLPM

5.2 Results and Discussion

5.2.1 Visual observation of IG-110 specimen

Figure 5.4 shows the comparison of IG-110 specimen before and after oxidation. From the photos, it can be clearly seen that the graphite specimen appears darker after oxidation. Visual observation shows that before oxidation, the surface of IG-110 specimen is fairly smooth without megascopic pores while after it is oxidized, the surface of the specimen becomes rough since small pores are developed during oxidation.

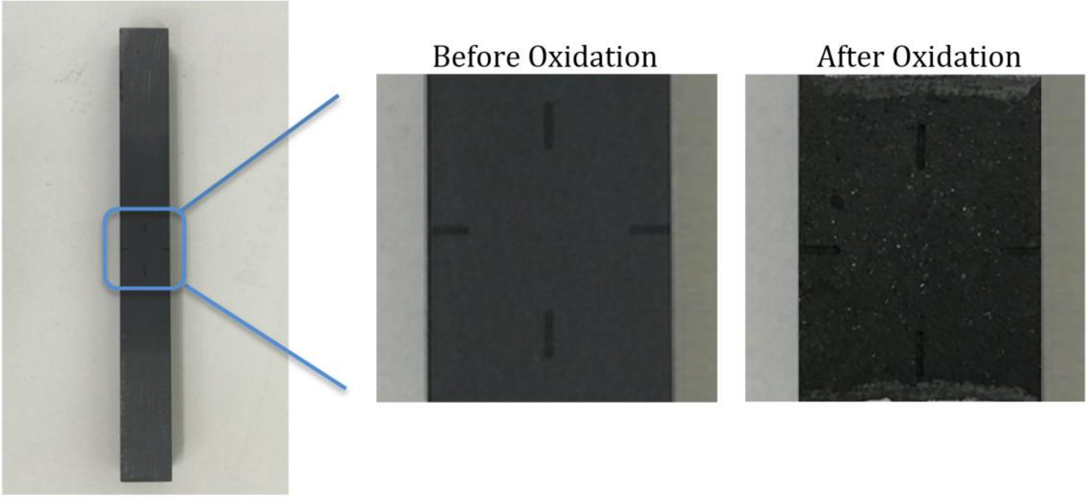

Figure 5.4 IG-110 specimen before and after oxidation

5.2.2 Effect of ambient condition

According to manufacturer [64], at wavelength of 1.55μm, the transmittance of 5mm TEMPAX window is approx. 90.0%. In other words, 10.0% of the radiation emitted (λ=1.55μm) by the graphite sample is absorbed or reflected by the TEMPAX window and only 90% of the radiation can reach the IR thermometer. This leads to a decreased value of the measured emissivity. In the pretest, the normal spectral emissivity of a black paint coated IG-110 sample was measured with and without observation window. The results are plotted in Figure 5.5. A transmittance of 89.3% is estimated by dividing the emissivity measurement with the window by the one without the window. This value is very close to the one we found in the reference. Compensated emissivities are calculated by dividing the original emissivity values measured in the main test

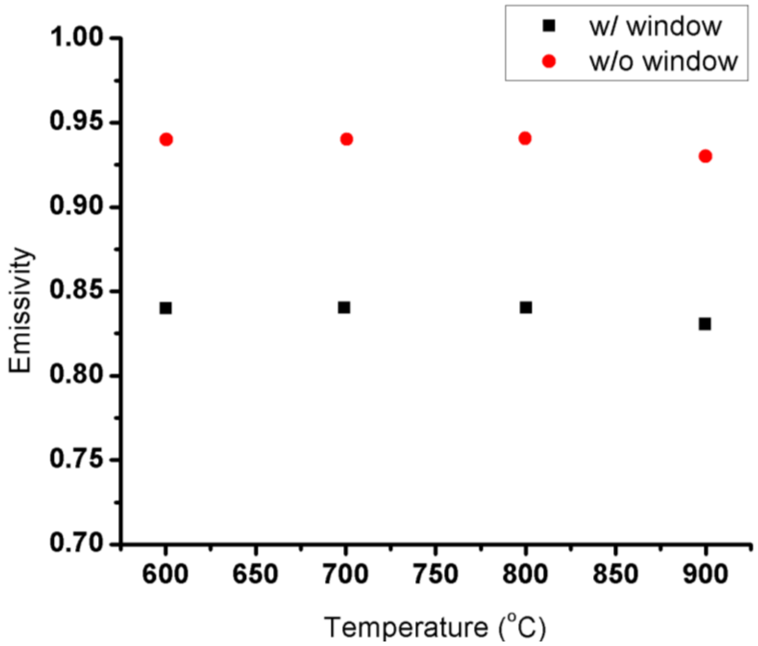

Figure 5.5 Normal spectral emissivity measurements of black paint coated IG-110 specimen with and without TEMPAX window

Moreover, without the window, the emissivity of the sample is measured to be 0.93~0.94 which agrees fairly well with the value provided by the black paint manufacturer (0.94) within an acceptable error. This indicates that other ambient factors such as the presence of air and helium on the transmission path and the radiation reflected from the internal surfaces of the chamber are negligible for this test set-up.

5.2.3 Measurement of IG-110 emissivity

Figure 5.6 shows the measured emissivity of non-oxidized IG-110 specimen. A total number of 53 measurement points were taken in the temperature range of 500˚C to 1000˚C in argon environment. As expected, the emissivity of IG-110 is quite high. The maximum, minimum and average emissivity obtained from the measurements were 0.879, 0.813 and 0.848 respectively. The normal spectral emissivity shows a slight decreasing trend as temperature increases. A linear curve has been calculated to describe the temperature dependency of non-oxidized IG-110, namely:

$$\varepsilon_\lambda = (0.881 \pm 0.025) - (4.25 \pm 3.18) \times 10^{-5} T \qquad (5.2)$$
$$\text{(95\% confidential interval)}$$

Where:

T = Temperature of the graphite in ˚C

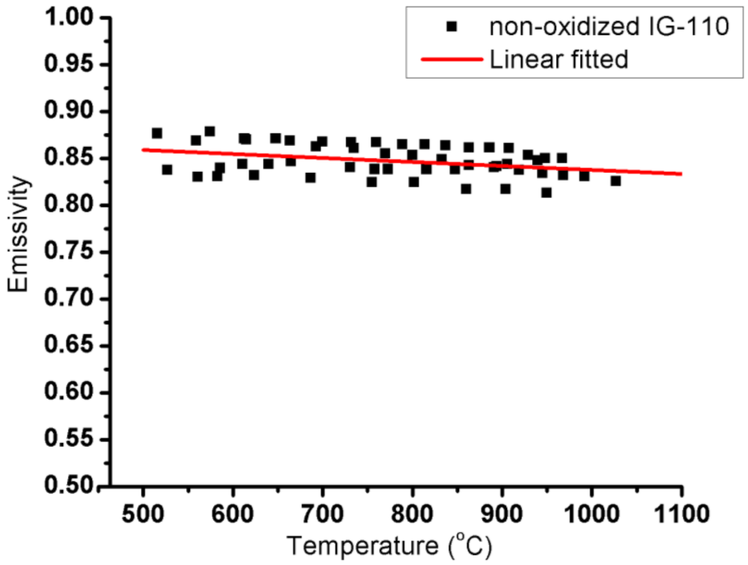

Figure 5.6 Normal spectral emissivity $(\lambda = 1.55\mu m)$ of non-oxidized IG-110 specimen

In normal operation, the fuel cladding temperature is approx. 1200˚C. And the emissivity, according to above equation, is estimated to be 0.830. In accident conditions, reactor core may experience abnormal elevated temperature. The safety criteria of HTGR is 1600˚C at which the emissivity is estimated to be 0.813.

Similar emissivity measurements were performed for oxidized IG-110 specimen. The results are summarized in Figure 5.7 54 measurement points were taken during the measurements of which the maximum, minimum and average emissivity as 0.908 0.866 and 0.889 respectively. Inspection of these experimental data shows that same temperature dependency of normal spectral emissivity was observed, i.e. emissivity decreases slight as temperature increase. The temperature dependency of oxidized specimen can be linear-fitted to:

$$\varepsilon_\lambda = (0.908 \pm 0.012) - (2.56 \pm 1.56) \times 10^{-5} T \tag{5.3}$$

(95% confidential interval)

According to the above equation, at 1600˚C, the emissivity of IG-110 is estimated as 0.867.

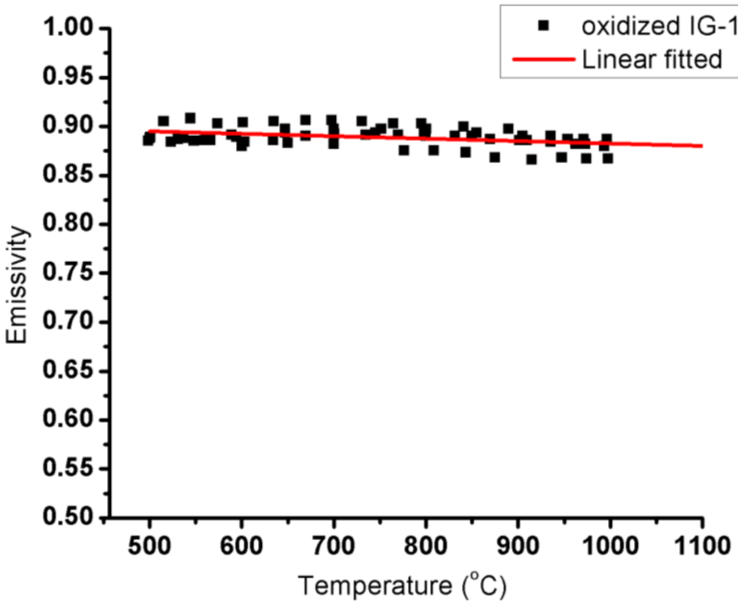

Figure 5.7 Normal spectral emissivity $(\lambda = 1.55\mu\text{m})$ of oxidized IG-110 specimen (0.0273g/cm2)

All the emissivity measurements are summarized in Figure 5.8. The black squares and red squares represent the emissivities before and after oxidation respectively. The green line is the emissivity value of 0.8, which is a conservative estimation commonly used for calculating radiation heat transfer during HTGR core design.

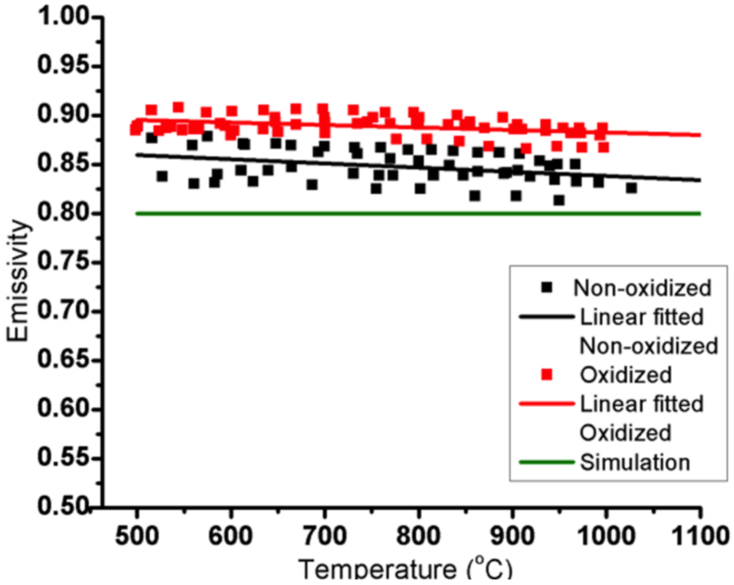

Figure 5.8 Normal spectral emissivity $(\lambda = 1.55\mu\text{m})$ of IG-110 w/ and w/o oxidation

Inspection of these experimental data shows that firstly, emissivity of the specimen increases by oxidation. Specifically, in our measurements, after being oxidized, the emissivity of IG-110 specimen increases by 4.8%. This phenomenon has also been observed by Seo S K et al. [61]. Their study suggested that the increase of porosity resulting from oxidation leads to an increase in thermal emissivity. This observation confirmed that during air ingress accident, the oxidized graphite components possess higher emissivity, which is favored for reactor cooling. Secondly, for both cases, the normal spectral emissivities show a slight decreasing trend as temperature increases. However, the changes of emissivity are fairly subtle as temperature varies. From the simulation point of view, at a certain oxidation degree, a constant emissivity could be utilized while simulating radiation heat transfer regardless of temperature. Last but not least, as shown in Figure 5.8, all the data points in our study are above 0.8, which indicates that emissivity of 0.8 is conservative for simulating either normal or air ingress condition. On the basis of experimental data, an emissivity of 0.83 is suggested for best estimation calculation during normal operation. For air ingress simulation, emissivity of 0.8 and 1.0 are suggested as the lower and upper bound respectively for parameter sensitivity analysis.

5.3 Conclusions

The normal spectral emissivity $(\lambda = 1.55\mu\text{m})$ measurements of IG-110 before and after oxidation were performed by employing the IR thermometer and K-type thermocouples in the temperature range of 500°C to 1000°C. The experimental results lead readily to the following conclusions:

1) The oxidized IG-110 has rough surface, which results in an increase in emissivity. In other words, the graphite oxidation occurs during air ingress enhances radiation heat transfer and is favored for reactor cool-down.

2) It is confirmed that the commonly used IG-110 graphite emissivity of 0.8 is conservative for normal and air ingress simulation. Emissivity of 1.0 and 0.80 are suggested as the upper and lower bound respectively for sensitivity analysis.

3) Correlations of normal spectral emissivity of IG-110 w/ and w/o oxidation as a function of temperatures were developed, which are given as ($\lambda = 1.55\mu$m, 95% confidential interval):

$$\text{Before oxidatoin: } \varepsilon_\lambda = (0.881 \pm 0.025) - (4.25 \pm 3.18) \times 10^{-5}\mathrm{T}$$

$$\text{After oxidiation: } \varepsilon_\lambda = (0.908 \pm 0.012) - (2.56 \pm 1.56) \times 10^{-5}\mathrm{T}$$

6. RELAP5/SCDAP Modification

6.1 Implementation

6.1.1 Overview

RELAP5/SCDAP was improved to simulate the thermal hydraulic behavior of HTGR. The improvements were focused on the ability to capture chemical reactions during air ingress. Firstly, the thermodynamic and transport properties for O_2, CO_2 and CO were added to RELAP5/SCDAP non-condensable database. Secondly, a graphite oxidation model considering the chemical equilibrium of CO and CO_2 as well as a CO combustion reaction were also added to the code. Rate equations selected for this study were all developed for IG-110 graphite. Two subroutines were created and six subroutines were modified to incorporate the new gas species and chemical models.

6.1.2 New non-condensable gas species

In RELAP5/SCDAP, non-condensable gases are treated as ideal gas. The gas species that are modeled in the original version includes: argon, helium, hydrogen, nitrogen, xenon, krypton, air and SF6. O_2, CO and CO_2 were added to the code to support the analysis of air ingress accident in HTGRs.

In order to model new gas species, thermal conductivity, viscosity, diffusion coefficient, internal energy, etc. are required by RELAP5/SCDAP. In fact, in 2003, Idaho National Engineering and Environmental Laboratory was working on the addition of new gas species into RELAP5-3D, and at that time, the parameters necessary for modeling O_2 CO and CO_2 were developed. Detailed information regarding the values and how they were derived were reported by Davis C.B et al. (2003). [65] The same values are adopted in present study.

Two additional variables, “ehengs” and ”moldiams”, which cannot be found in Davis’s report, are required by RELAP5/SCDAP. These variables are not related with the chemical reactions but are mandatory for program compilations. The definitions and values adopted for the variables are:

1) “ehengs”: the definition of this variable is not provided in the manuals. It appears only once in the r-level subroutine “rnoncn.ff” where it is assigned with an initial value. The data used for N2 was adopted for O_2, CO and CO_2.

2) “moldiams”: this variable represents the diameter of molecular in Angstrom $(10^{-10}m)$. The values were calculated from van der Waals equation of state by using the following expression:

$$\frac{4\pi\left(\frac{D}{2}\right)^3}{3}=\frac{b}{N_A} \tag{6.1}$$

Where:

D = Diameter of the molecular

b = Volume per mole that is occupied by the molecular

N_A = Avogadro constant

The values adopted for O_2, CO and CO_2 were 2.934, 3.152 and 3.239 respectively.

One new variable “dcono2”, defined as the diffusion coefficient of noncondensable gas in O_2, was added to the noncondensable gas database. The values derived for He, N2, CO, CO_2 and O_2 were $3.4838 \times 10^{-4}, 7.7494 \times 10^{-5}, 9.8409 \times 10^{-5} 7.6767 \times 10^{-5}\ and\ 9.8305 \times 10^{-5}$ respectively. Table 6.1 summarized the subroutines being modified to incorporate the new noncondensable gas species

Table 6.1 Description of modified subroutine

Subroutine	**Description**	**Modification**
rnoncn.ff	Processes the input data for constants needed in noncondensable gas calculations	Additional constants were added for O_2, CO and CO_2
statec.ff	Holds global variables for noncondensable gases and molten metal field	Defines global variables for new gas species

6.1.3 Chemical reactions

Chemical models and new/modified subroutines

Two chemical reactions, namely graphite oxidation and CO combustion, were incorporated to RELAP5/SCDAP. A model based on the classic graphite oxidation theory was selected for code implementation. The reaction rate equation was developed by Kim et al. (2006) [25] for IG-110 graphite. To improve the accuracy of simulation in low temperature regime, the multiplication factor, M(B), which considers the impact of change of graphite’s internal structure on reaction rate , has been modified prior to model implementation. Dryer’s rate equation is selected for computing the CO combustion reaction. The moisture fraction required by the Dryer’s equation was preset at 0.002wt% but can be changed from the source code. Table 6.2 summarized the subroutines being created or modified to incorporate the chemical reactions.

Table 6.2 Description of new/modified subroutines

Subroutine	**Description**	**Remark**
graoxi.ff	Calculates the graphite oxidation and CO combustion reactions	New subroutine
goxidat.ff	Holds global variables defined for graphite oxidation and CO combustion	New subroutine
rhtcmp.ff	Processes the input data and sets up storage for heat structures	Modification: sets up storage for the global variables defined for chemical reactions
ht1tdp.ff	Does the one-dimensional heat conduction solution	Modification: activates the chemical reaction calculation if "graphite oxidation option" is selected
majout.ff	Generates major edit	Modification: adds the chemical reaction related qualities to major edit
htadv.ff	Main driver for heat structure advancement	Modification: resets the noncondensable source term to zero before each time step

Model implementation

In the following paragraphs, the modeling of chemical reactions is elaborated from the coding perspective. The RELAP5 code structure and the flowchart for advancing one time step are depict in Figure 6.1.

As shown in Figure 6.1,"relap5.ff" is the main driver of the program. It calls "trnctl.ff" to initiate a series of transient advancement subroutines. "tran.ff" called by "trnct.ff", is the subroutine which controls the transient calculation. Major subroutines called by "tran.ff" includes "htadv.ff" and "hydro.ff" which advance the heat structure and hydrodynamic solutions respectively. "ht1tdp.ff" is a subroutine one level lower than "htadv.ff". It does the one-dimensional heat conduction. It calls the "graoxi.ff" subroutine, which was developed by present study to model the chemical reactions occurring during HTGR air ingress accident.

Graphite oxidation and CO combustion are computed at the beginning of each time step because it alters the solutions of heat structure and hydrodynamics. Specifically, the heat generated by graphite oxidation is implicitly added to the energy source of heat structure boundary mesh point before "ht1tdp.ff" solves the one-dimensional heat conduction. The heat absorbed by the CO combustion and the mass source term of O_2, CO and CO_2 are utilized by "hydro.ff" where the flow conditions are updated for current time step reflecting the chemical reactions, convective heat transfer, etc. by solving the momentum, mass, energy conservation equations with an additional set of closure relationships.

To activate the graphite oxidation model, user must define heat structures and select the graphite oxidation option from input decks. Currently the user option has not been implemented and therefore, graphite oxidation option is directly controlled from the source code.

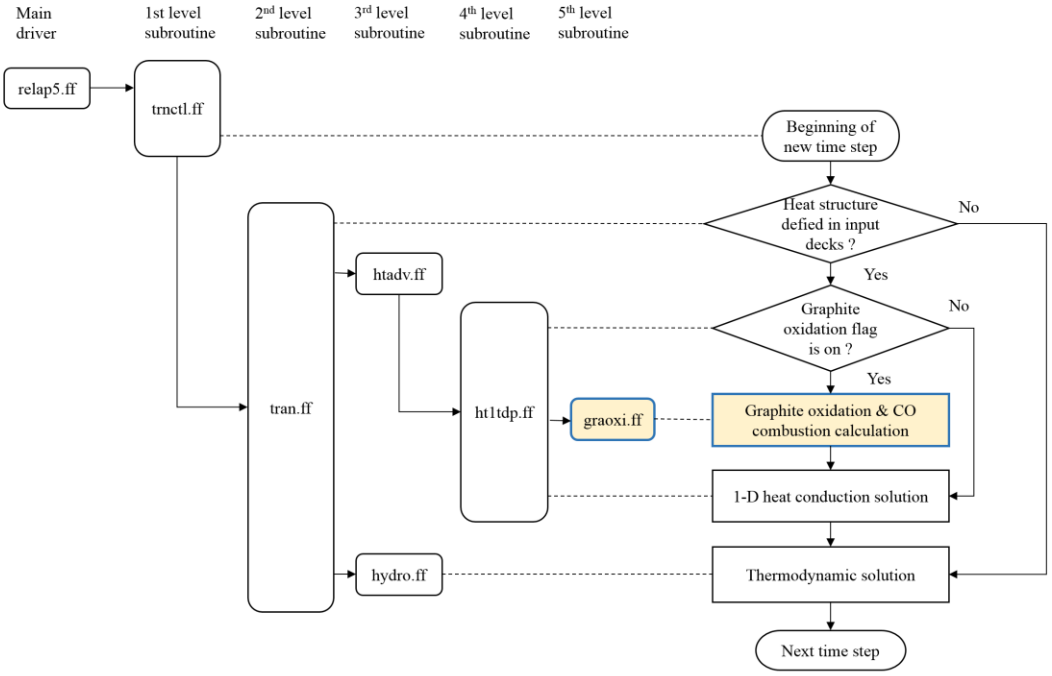

Figure 6.1 Code structure and flowchart for advancing one time step

Variable exchange between new chemical model and RELAP5 program

The exchange of information between the new chemical model ("graoxi.ff") and the rest of the RELAP5 program occurs through the medium of a module called "goxidat.ff". "goxidat.ff" contains the global variables that are used and modified in "graoxi.ff". Should the graphite oxidation model be activated, the flow of information between the "graoxi.ff" and the rest of the program occurs at every time step.

The information flowing between "graoxi.ff" and the rest RELAP5 program is shown in Figure 6.2. This figure identified subroutines in RELAP5 that exchange information with "graoxi.ff" and the names of the variables that contain the transmitted information. The information shown in orange is transferred from RELAP5 program to "graoxi.ff". The information shown in black is passed on to RELAP5 from "graoxi.ff".

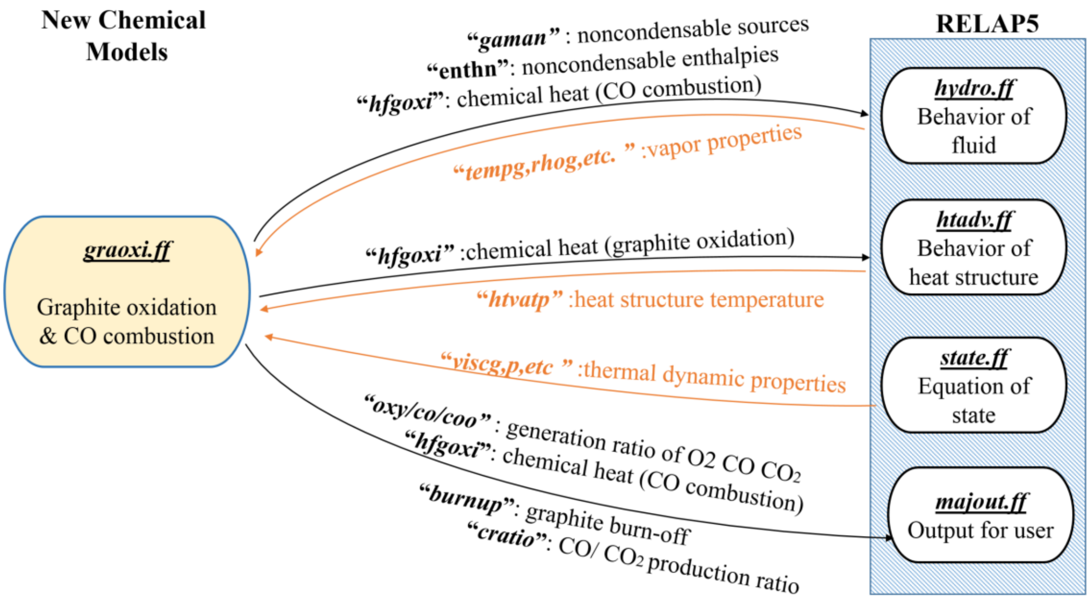

Figure 6.2 Flow of information between "graoxi.ff" and the rest RELAP5 program

The variables that are calculated in “graoxi.ff” and then passed on to the rest of the program are listed in Table 6.3.

Table 6.3 Variable calculated by “graoxi.ff” subroutine and passed on to RELAP5

Variable	Type	Definition
gaman	real	Noncondensable generation rate per unit volume (kg/m3)
enthn	real	Enthalpy of noncondensable source (J/kg)
hfgoxi	real	Total chemical heat generation/absorption (W/m)
oxy	real	Total O_2 generation rate (mole/s) per heat structure geometry
co	real	Total CO generation rate (mole/s) per heat structure geometry
coo	real	Total CO_2 generation rate (mole/s) per heat structure geometry
brnup	real	Graphite burn-off (%)of a certain heat structure geometry
cratio	real	CO CO_2 production rate ratio of a certain heat structure geometry

The impacts of these variables on the rest of RELAP5 program are discussed as follow:

1) **gaman:** The mass source terms of noncondensable gases that store for each control volume are adjust by “graoxi.ff” to account for the production and consumption of O_2, CO and CO_2 by graphite oxidation and CO combustion. The variable updated by “graoxi.ff” is vol(n)%gaman(i), which is the volumetric mass source term for the i-th type of noncondensable gas for the control volume with the index “n”. These source terms are modified by “graoxi.ff” at each time step for each control volume that associates with a heat structure geometry. This variable alters the composition of noncondensable gas species and impacts the thermodynamic solution.

2) **enthn:**“graoxi.ff” updates the enthalpy of O_2, CO and CO_2 source according to their temperature at current time step. The variable adjusted by “graoxi.ff” is

vol(n)%enthn(i), which is the enthalpy of the i-th type of noncondensable gas for the control volume with the index "n". The enthalpies are modified at each time step for each control volume that associates with a heat structure geometry. This variable alters the energy source term of the conservation equation and thus affects the fluid temperature.

3) **hfgoxi:** The exothermic heat generated by the graphite oxidation is computed in "graoxi.ff" and passed on to a RELAP5 subroutine "ht1tdp.ff" to calculate the conductive heat transfer within heat structures. This variable is named hfgoxi. hfgoxi impacts the calculated heat structure temperature as well as the convective heat transfer at the interface between the heat structure and fluid.

4) **oxy/co/coo:** The O_2, CO and CO_2 generation rate, denoted as oxy co coo, are computed by "graoxi.ff" for each heat structure geometry. The results are then pass on to a RELAP subroutine called "majout.ff" which is responsible for generating the major edit for user inspection. The gas generation rates are updated at each time step but are printed out at user specified frequency.

5) **brnup:** the variable "brnup" represents graphite burn-off (%). It is computed explicitly in "graoxi.ff" according to the graphite oxidation reaction rate of current time step and oxidation history. The updated value of "brnup" is used to calculate the reaction rate of graphite oxidation at next time step. It is passed on to the RELAP "majout.ff" for major edit.

6) **cratio:** The CO, CO_2 production ratio is computed in "graoxi.ff" for each heat structure geometry and passed on to the RELAP subroutine "majout.ff" for printing in major edit.

RELAP5 calculates several variables that are transferred to “graoxi.ff” to simulate the impacts of chemical reactions on thermalhydraulic system. The variables that are calculated in RELAP5 program and then passed on to the “graoxi.ff” are summarized in Table 6.4.

Table 6.4 Variable calculated by RELAP5 and passed on to “graoxi.ff” subroutine

Variable	**Type**	**Definition**
htvatp	real	Volume averaged temperature of heat structure (K)
p	real	Pressure at new time (Pa)
qualan	real	Noncondensable mass fraction for new time step
tempg	real	Vapor temperature (K)
rhog	real	Vapor density (kg/ms3)
viscg	real	Vapor viscosity (kg/m-s)
velg	real	Average vapor velocity at a specific control volume
dconoxy	real	Diffusion coefficient of noncondensable gas in O_2 (m2/s)
tmassv	real	Total mass per control volume (kg)
diamv	real	Equivalent flow diameter (m)
recipv	real	Reciprocal of volume (m-3)

The first variable transferred to “graoxi.ff” is htvatp which the volume averaged temperature of a heat structure geometry. “graoxi.ff” uses the RELAP5 calculated temperature to estimate the reaction rate of graphite oxidation in regime I. A set of variables regarding thermodynamic properties of fluid and flow-path geometry were passed on to “graoxi.ff”. These variables are qualan (non-condensable mass fraction), p (pressure), rhog (vapor density), viscg (vapor viscosity), diamv (equivalent flow diameter), etc. According to the geometric properties of the flow-path and flow dynamic characteristic provided by RELAP5, “graoxi.ff’ computes the concentrations, partial pressures of gas species and mass transfer coefficient, from which the reaction rates of graphite oxidation and CO combustion are determined.

6.2 Verification and Validation

6.2.1 Overview

Model verification and validation are the primary processes for quantifying and building credibility in numerical models. The definition of verification and validation are:

- Verification is concerned with building the model right. It is utilized in the comparison of the conceptual model to the computer representation that implements that conception

- Validation is concerned with building the right model. It is the process of finding out the degree to which a computer representation is accurate representation of the real world phenomena.

In the following sections, the process of verification and validation of RELAP5/SCDAP with new chemical models is elaborated. A simulation case based on the Kim et al. (2006) [25]'s experimental facility was performed in order to confirm that the graphite oxidation model has been correctly implemented into RELAP5/SCDAP.

For validation, three experiment studies of graphite oxidation (IG-110) that conducted over a wide temperature range are chosen. Simulations were performed to judge the model accuracy by comparing the simulation results to actual experimental data.

6.2.2 Verification

The verification case is created based on a graphite oxidation experiment carried out by Kim and NO in 2006. The verification is considered successful if the Arrhenius plot of reaction rate vs. temperature for graphite oxidation reaction can be recreated in simulations.

Test facility

As shown in Figure 6.3, the test section was made of a cylinder quartz tube. The IG-110 specimen was installed at the center of the test section supported by ceramic supporters. The gas mixture of O_2 and He enters the concentrate tube annulus from the bottom, flowing through a long entry region so that upon reaching the specimen section, the laminar velocity profile has been fully developed. The specimens were machined to cylindrical specifications: diameter 2.1cm and length 3 cm. The diameter of the test section was 7.6cm. The IG-110 specimen was held at constant temperature by an induction heater.

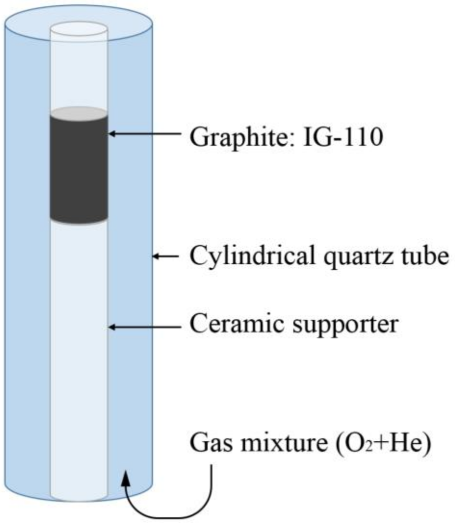

Figure 6.3 Schematic diagram of the test section

RELAP idealization and simulation conditions

A RELAP idealization has been developed based on Kim and NO’s test section. As shown in Figure 6.4, the idealization starts from ”insorc” which is a time depend volume used to model a pressure boundary. From bottom to top, the gas mixture of O_2 and He flows through the long entrance region, specimen region and exits the tube from the top. The flow path is modeled as annulus component and the specimen is modeled as heat structure. The boundary conditions used in the simulations are summarized in Table 6.5.

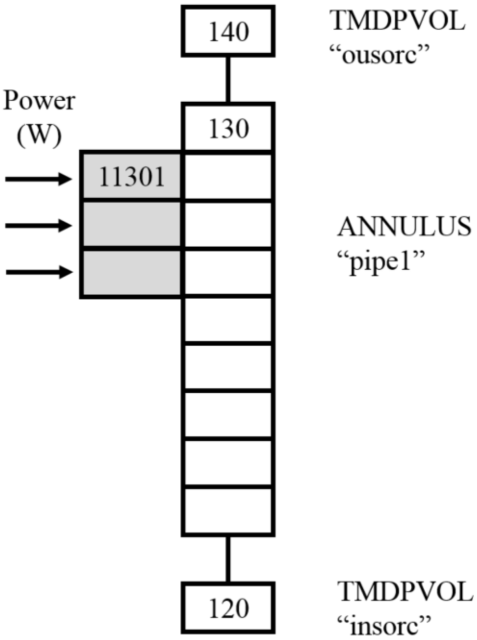

Figure 6.4 RELAP5 idealization of Kim and NO experiment

Table 6.5 Boundary condition used in the simulations

Parameter	Value
Gas mixture	He, O_2
Gas mixture pressure	0.101 MPa
Graphite temperature	400˚C~1500˚C
Inlet flow rate	0.16m/s
Inlet oxygen mole fraction	2.5%, 20%

For verification, two sets of simulations were carried out at different inlet oxygen mole fraction (2.5% and 20%). For each mole fraction, the simulations were performed for 12 times as graphite temperature varying from 400˚C to 1500˚C. The reaction rates were calculated from the simulation results of noncondensable mass fraction using the following equations:

$$\mathrm{R_g}\left(\frac{\mathrm{kg}}{\mathrm{s}}\right) = \mathrm{M_c} \times \frac{\dot{\mathrm{m}}_{\mathrm{O_2}} \times (\mathrm{X_{CO_2}} + \mathrm{X_{CO}})}{(\mathrm{X_{O_2}} + \mathrm{X_{CO_2}} + \frac{1}{2}\mathrm{X_{CO}})} \tag{6.2}$$

Where:

$\mathrm{M_c}$ = Molecular mass of carbon

$\dot{\mathrm{m}}_{\mathrm{O_2}}$ = Oxygen mole flow rate at inlet (mole/s)

$\mathrm{X_i}$ = Mole fraction of species *i* at outlet

The above equation is derived from the mass conservation of oxygen. In RELAP5/SCDAP, mass fractions of the noncondensable species are updated in the hydro subroutines, which are not executed until the very end of each time step. This is because the hydrodynamic solutions need to account for all the physical and chemical phenomena that occur during one time step. Accordingly, if the calculation of the mass fractions is correct, then it can be confirmed that the graphite oxidation model, which is executed prior to the hydro subroutines has been properly implemented.

Results and discussion

Figure 6.5 illustrates the simulation results plotted in Arrhenius format (i.e. logarithm of rate versus reciprocal absolute temperature). The reaction rate predicted by graphite oxidation theory is depicted in Figure 6.6 for comparison. Theoretically, the reaction can be classified into three regimes as temperate varies. The activation energy in regime I, II and III are E_A, $E_A/2$ and 0 respectively.

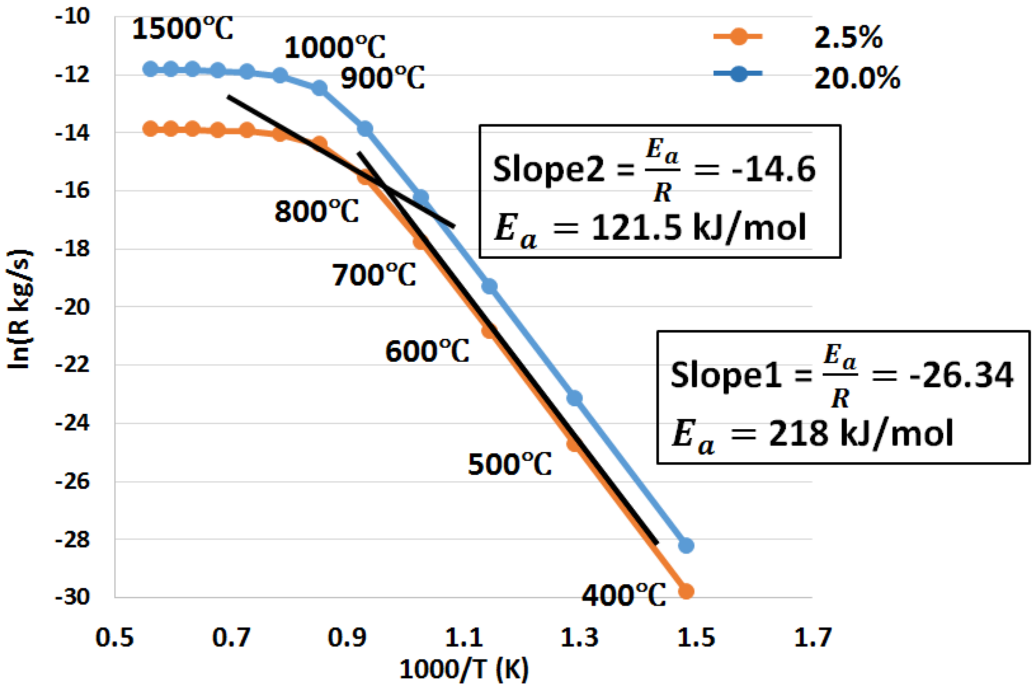

Figure 6.5 Simulation results of temperature dependence of graphite oxidation rates

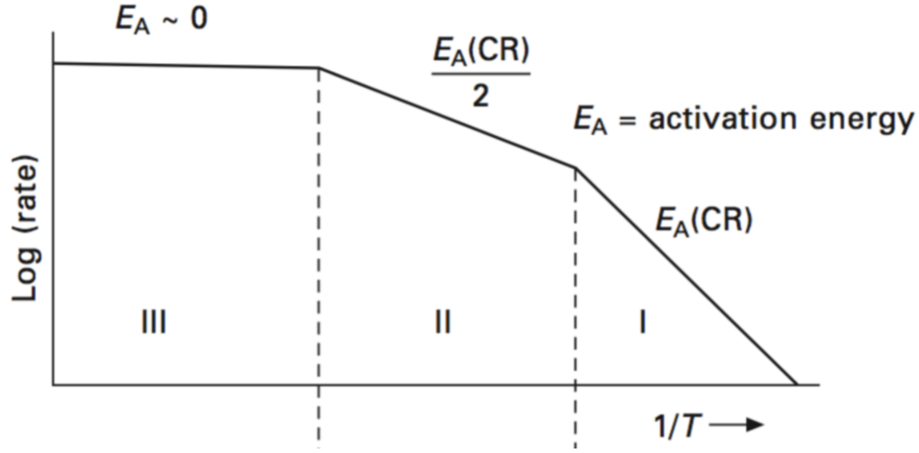

Figure 6.6 Arrhenius plot of graphite oxidation rate

Inspection of Figure 6.5 shows that:

- Three regimes can be identified as temperature varies. Regime I is from 400˚C to 700˚C, regime II is from 700˚C to 1000˚C and regime III is above 1000˚C. The reaction rate smoothly transits from one regime to another.

- In regime I, the fitting line has a -26.34 slope. When using the Arrhenius relationship to describe the temperature dependency of reaction rate, the slope is $-E_A/R$. Thus, the activation energy is $218\ kJ/mol$, which agrees well with the reaction rate equation implemented into RELAP5/SCDAP.

- As temperate increased, the increasing trend slows down and the slope of the fitting line is -14.6 and the E_A is calculated to be 121.5 kJ/mol, which is approx. half of 218 kJ/mol calculated for regime I.

- In regime III, the reaction rate remains constant as temperature increase.

- Both 2.5% and 20% cases show the same temperature dependency of reaction rate

Conclusions

Simulations were performed for the Kim and No graphite oxidation experiment at 2.5% and 20% oxygen mole fraction over a wide temperature range from 400˚C to 1500˚C. The reaction rate was calculated from the mass fraction predicted by the code after incorporated the graphite oxidation model and the trend of the reaction rate agrees well with the classic graphite oxidation theory. Therefore, it can be confirmed that the graphite oxidation model has been successfully implemented into RELAP5/SCDAP

6.2.3 Validation

To determine the accuracy of the implemented graphite oxidation model, three experimental studies were chosen for code validation. Table 6.6 listed the experiments for code validation with their corresponding temperature regimes. The selected experimental studies meet the following requirements:

- The graphite grade IG-110 used in the experiments.
- The combination of selected experiments covers all the control regimes of graphite oxidation.

Table 6.6 Graphite oxidation experiments selected for code validation

	Regime I	**Regime II**	**Regime III**
Chi and Kim graphite oxidation experiment (2008)[66]	√		
Choi and Woong-Ki graphite oxidation experiment (2010)[67]	√		
Ogawa’s circular tube experiment (1993)[4]	√	√	√

Chi and Kim graphite oxidation experiment

Test facility and experimental results

As illustrated in Figure 6.7, Chi and Kim' s test system is composed of a vertical tube furnace, a gas supplying system and an analytical balance. During the oxidation experiment, dry air was injected from the bottom of the test section at 10 SLPM. The cylindrical IG-110 specimen (D: 25.4mm H: 25.4mm) was hung under the analytical balance and the weight of the specimen was kept being measured. The graphite temperature was maintained at 603˚C during oxidation. The oxidation process lasted for approx. 40 hours until the IG-110 specimen lost 10% of its initial weight. The experimental conditions are summarized in Table 6.7.

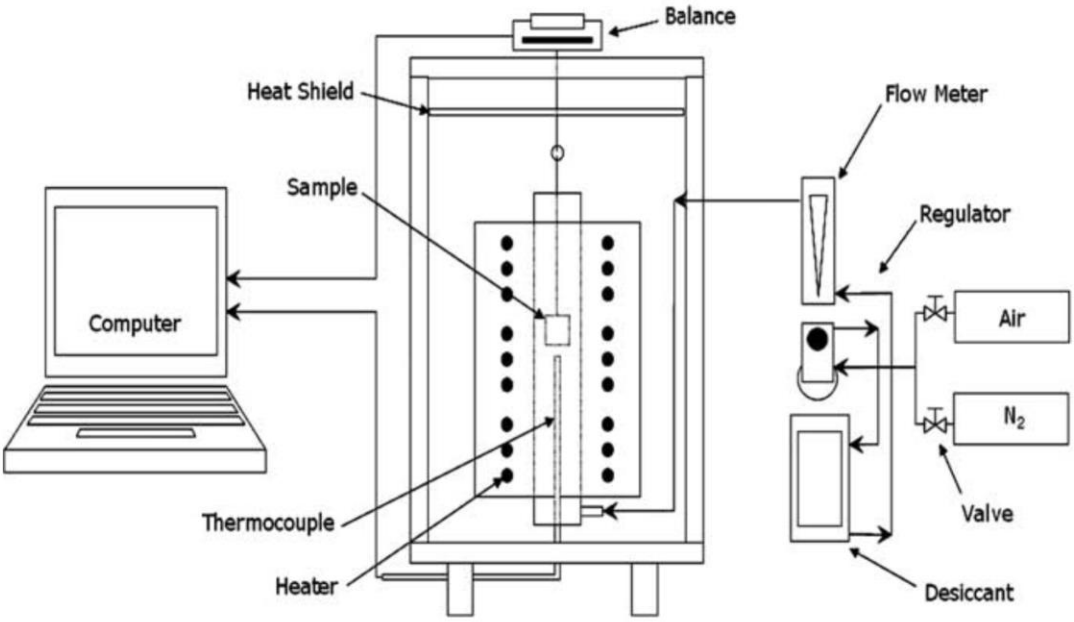

Figure 6.7 Graphite oxidation test system by Chi and Kim [66]

Table 6.7 Experimental conditions of Chi and Kim oxidation experiment

Parameter	**Value**
Gas type	Dry air
Inlet oxygen mole fraction	21%
Pressure	0.101MPa
Inlet flow rate	10 SLPM
Graphite temperature	603˚C
Specimen dimension	D: 25.4mm H: 25.4mm

The weight loss versus the time behavior of the specimen was depicted in Figure 6.8. The weight loss data was presented over a time range of 27 to 40 hour. According to the measurement, it requires 27.3 hours to reach 5.0% burn-off and 39.0 hours to reach 9.7% burn-off.

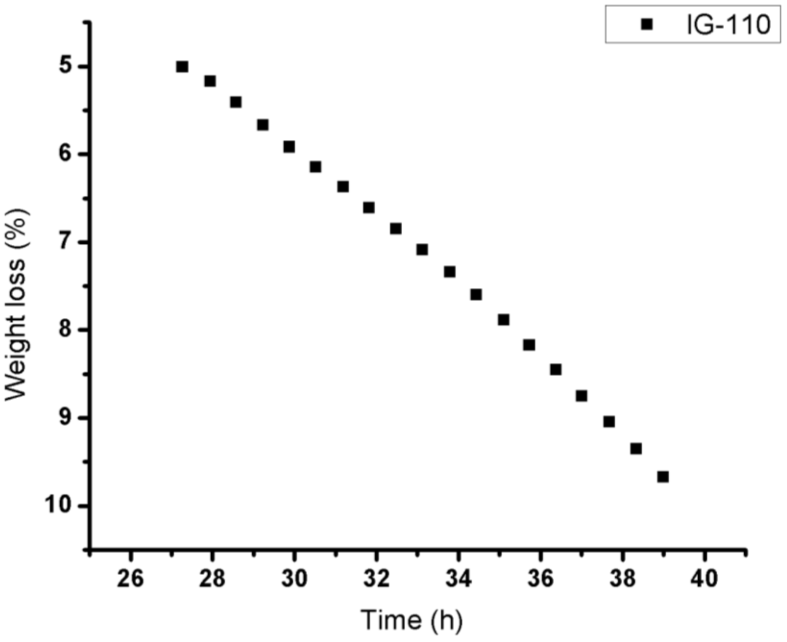

Figure 6.8 Weigh loss of IG-110 oxidized at 603˚C as a function of oxidation time (plotted from Chi and Kim's experimental data [66])

Simulation Results and Conclusions

Figure 6.9 illustrated the weight loss measured in the experiments (blue bar), estimated by Kim and NO rate equation (orange bar) and computed by RELAP5/SCDAP (grey bar, with modified M(B). The modification method is present in detail in section). Inspection of Figure 6.9 shows that:

- In regime I, at 5%~6% burn-off, Kim and NO rate equation tends to underestimate the reaction rate while with the modified M(b), whereas the graphite oxidation model in RELAP5/SCDAP tends to over-predict the amount of oxidation.

- Specifically, under the given experimental conditions, the Kim and NO rate equation underestimated the reaction rate by 28%~33% while RELAP/SCDAP over-predicted the reaction rate by approx.18%

Although the RELAP5/SCDAP simulation results did not fit the data as well as would be desired, the accuracy of predicting the weight loss was improved compared to the original Kim and NO model.

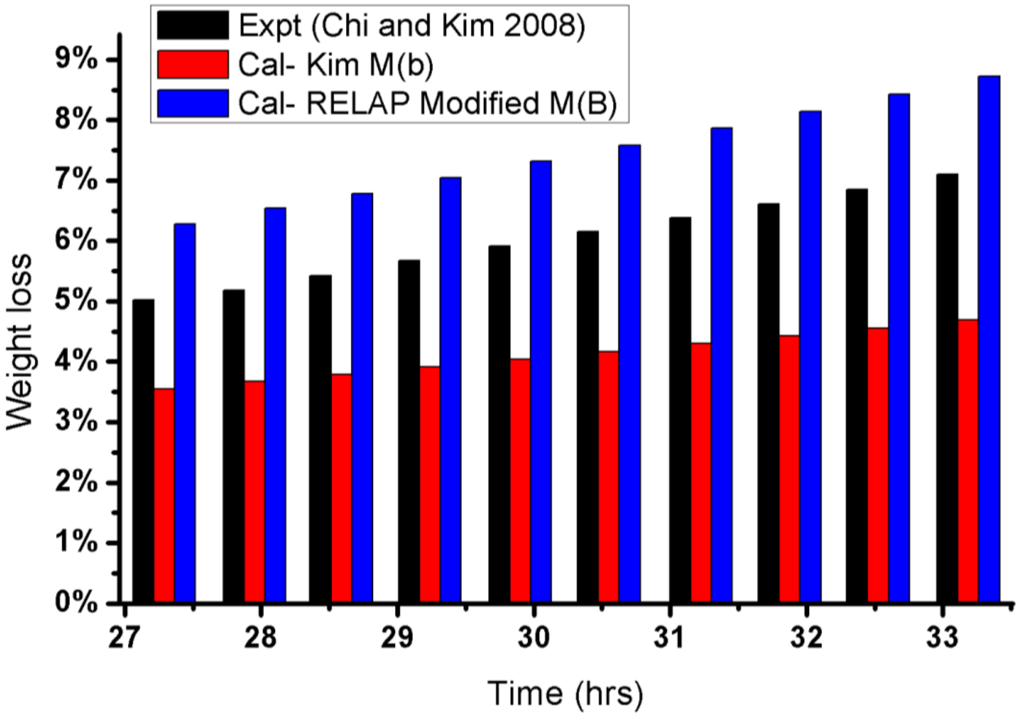

Figure 6.9 Compassion of Chi and Kim experiment, Kim and NO's correlation and RELAP5/SCDAP's results

Choi and Woong-Ki graphite oxidation experiment

Test facility and experimental results

In Choi and Woong-Ki's experiment, the IG-110 specimen was oxidized in a tube furnace at 600˚C with 300cm3/min gas flow in air. The specimen was machined into slab geometry of which the length, width and thickness are 40mm, 40mm and 5mm respectively. The IG-110 specimen was polished to a maximum roughness of 1.5μm prior to oxidation. The experimental conditions are summarized in Table 6.8.

Table 6.8 Experimental conditions of Choi and Woong-Ki oxidation experiment

Parameter	**Value**
Gas type	air
Inlet oxygen mole fraction	21%
Pressure	0.101MPa
Inlet flow rate	0.3SLPM
Graphite temperature	600˚C
Specimen dimension	40mm×40mm×5mm

The weight loss of IG-110 specimen as a function of oxidation time is depicted in Figure 6.10. The collection of data lasted for 30 hours. According to Choi and Woong-Ki, 5.67% burn-off occurred at 30.48 hours, which is comparable to Chi and Kim's experimental measurement where the same burn-off was achieved at 29.2 hours.

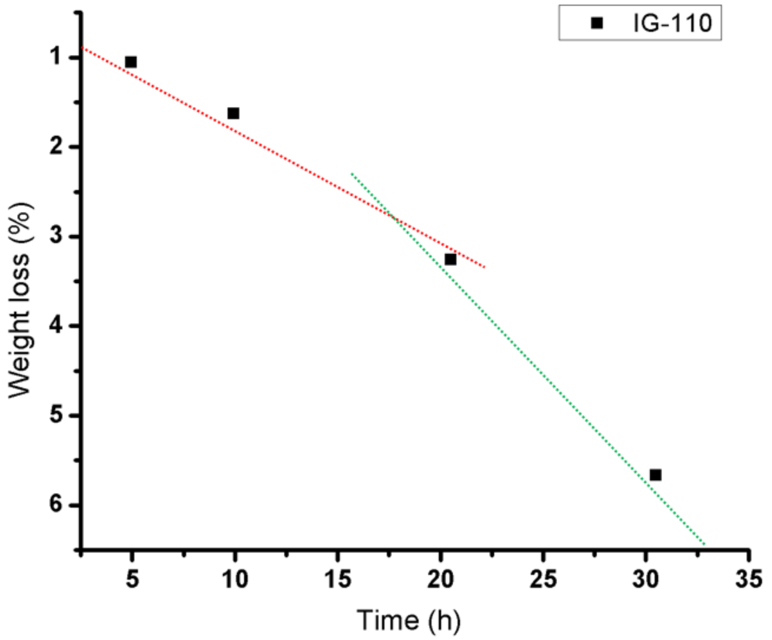

Figure 6.10 Weigh loss of IG-110 oxidized at 600˚C as a function of oxidation time (plotted from Choi and Woong-Ki experimental data [67]

The consistency of data reported by different researchers, to some degree, confirms the reliability of the data used in this valuation work. In addition, the slope of the plot, which represents the oxidation reaction rate (%/hrs), gets steeper as burn-off increase, (the red dotted line is the slope line at 5 hours and the green dotted line is the slope line at 30 hours) which indicates the impact of burn-off on the rate of reaction.

Simulation Results and Conclusions

The weight loss measured in the experiments (blue bar), calculated by Kim and NO rate equation (orange bar) and RELAP5/SCDAP (grey bar) are summarized in Figure 6.11. As shown in Figure 6.11, after 5 hours of oxidation, the weight losses estimated by the Kim & NO model and by RELAP5/SCDAP were 0.43% and 0.47% respectively, which are fairly close to each other. However, after 30 hours, the RELAP5/SCDAP predicted the weight loss to be 6.09% compared to that of 3.56% predicted by the Kim and NO model. This suggests that the modification of M(B) has profound effect on computing the graphite weight loss during long-term transients. In addition, it is clearly shown in the figure that Kim and NO model under estimated the weight loss while RELAP5/SCDAP yielded a better agreement with the experiment results.

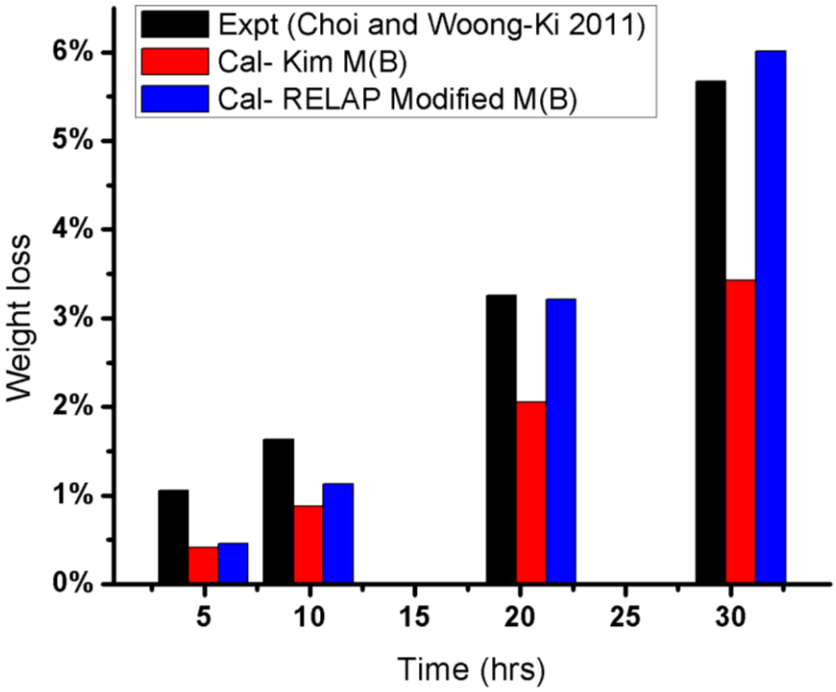

Figure 6.11 Compassion of Choi and Woong-Ki experiment, Kim and NO's correlation and RELAP5/SCDAP's results

Ogawa's Circular Tube Experiment

Test facility and experimental results

As illustrated in Figure 6.12, the test section was made of a metal tube. A hollow cylindrical specimen of 200mm length and an inner and outer diameter of 20.9mm and 44.9mm respectively was mounted on the metal tube. A gas mixture of He and O_2 was injected from the bottom of the tube, flowing upwards through the entrance region, specimen region and eventually exited the tube. The gas mixture was then collected and analysis by a gas component analysis system. It must be emphasized that hydrodynamically fully developed laminar flow was obtained in the long entrance before reaching the specimen. The oxidation experiments were repeated for several times as specimen temperature varies from 600˚C to 1030˚C. The experimental conditions are summarized in Table 6.9.

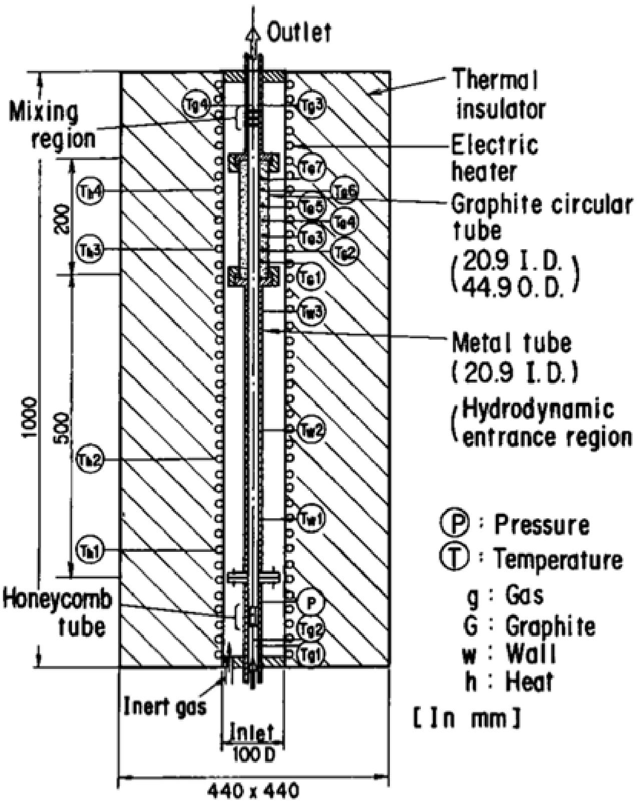

Figure 6.12 Graphite oxidation test section by Ogawa [4]

Table 6.9 Experimental conditions of Ogawa experiment

Parameter	Value
Gas mixture	He, O_2
Inlet oxygen mass fraction	20%
Pressure	~0.105MPa
Inlet Reynolds number	80
Graphite temperature	600˚C~1030˚C
Specimen dimension	ID: 20.9mm OD: 44.9mm H: 200m

The gas compositions measured at the tube outlet were depicted in Figure 6.13. The dots represent the measured data, whereas the analytical solutions given by Ogawa et al. are plotted in dash lines.

At 600˚C and 700˚C, only a small amount of oxygen was consumed by graphite oxidation due to the low reaction rate. The oxygen mass fraction at tube outlet was approx. 20% similar to the value at inlet. As temperature increases, the reaction rate increases. More oxygen was consumed while the gas mixture flow through the specimen region. Consequently, at the tube outlet, the oxygen mass fraction declined and the CO and CO_2 mass fraction increased. When temperature exceeds 1000˚C, the oxygen mass fraction remains unchanged regardless of graphite temperature indicating that the chemical reaction was in the mass transfer controlled regime (regime III). For the CO/CO_2 generation rate ratio, the chemical reactions were in favor of generation CO at first. However, as temperature increases, CO combustion proceeds more rapidly, resulting in a decrease of CO concentration after 950˚C.

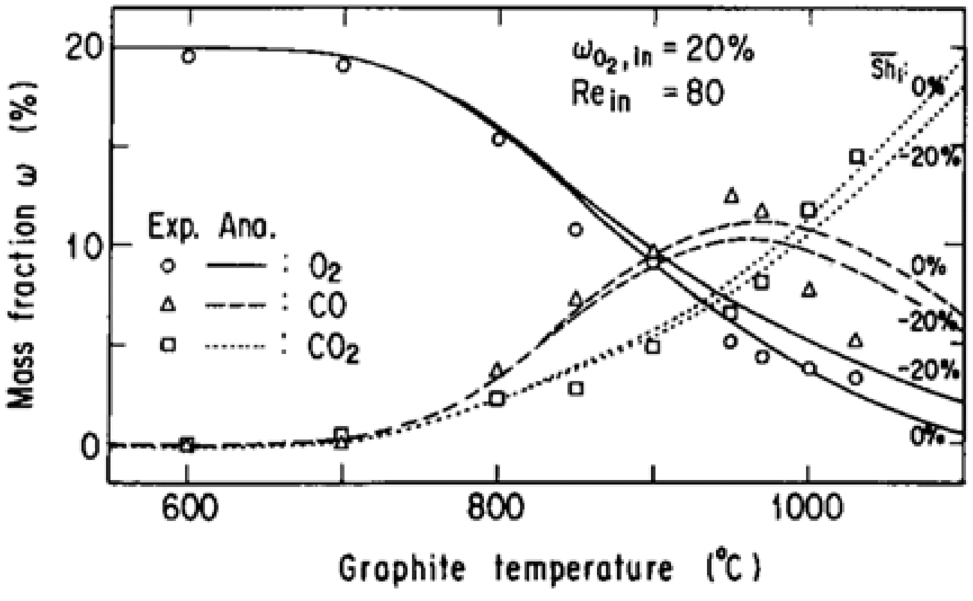

Figure 6.13 Gas compositions measured in Ogawa experiment [4]

Simulation Results and Conclusions

A RELAP idealization was created based on Ogawa's test section. A moisture fraction of 0.002wt% was assumed for simulations. Figure 6.14 shows a comparison between the simulation and experiment. The dotted lines are the mass fraction of O_2, CO and CO_2 predicted by RELAP5/SCDAP and the dots represent experimental data. Because of the short oxidation period and extremely low reaction rate, over the temperature range 600~700˚C, the impacts of chemical reactions were not well reflected in the mass fraction measurements. Thus comparisons of computed and experimental results are focused on regime II and regime III.

Inspection of Figure 6.14 shows that:

- The trends of the mass fraction of O_2, CO and CO_2 can be captured by RELAP5/SCDAP. Particularly the turn-around-point of CO at 950℃ is well reproduced by the code.

- In regime II and III, the oxygen mass fraction predicted by the code was lower than the experiment results whereas the CO and CO_2 mass fraction were higher than that of the experiment. This suggests that RELAP5/SCDAP tends to over-estimate graphite oxidation at intermediate and high temperatures.

- The greatest deviation between the simulation and experiment was found at 900˚C, where RELAP5/SCDAP under estimated the oxygen mass fraction by approx. 44%.

- It is found that if the mass transfer coefficient decreases by 20%, the oxygen mass fraction predicted by the RELAP5/SCDAP fits well with those points measured in regime III.

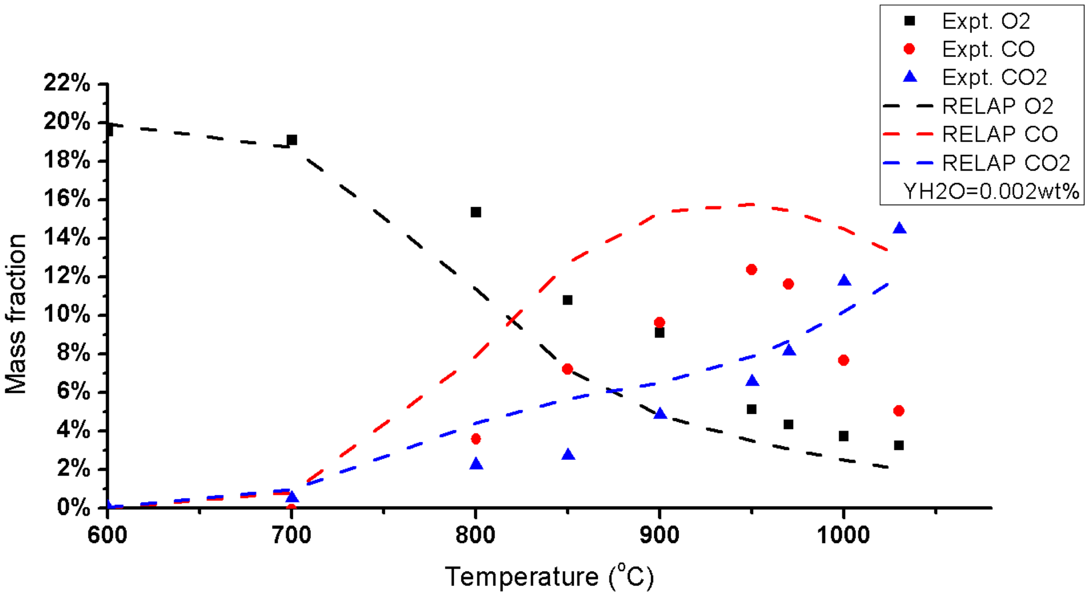

Figure 6.14 Simulation results of the mass fraction of O_2, CO and CO_2 at tube outlet as a function of temperature

On the basis of comparison with experimental data, it can be concluded that the graphite oxidation and CO combustion models implemented in RELAP5/SCDAP are valid. In regime III, the Graetz solution utilized for calculating the mass transfer gives predictions within 20% of observed values, of which the accuracy is acceptable for a system analysis code. For regime II, the deviation of simulation results from the experiment was larger than one would desire, however, the temperature of regime II is far below the safety criteria of 1600°C and therefore of less concern to an event of HTGR air ingress.

6.3 Modification of M(B)

6.3.1 Overview

As mentioned previously, burn-off, which is defined as a certain percent of weight loss due to oxidation of graphite, has great impact on the reaction rate of graphite oxidation in chemical kinetic controlled regime. Thus, a multiplication factor, M(B), which describes the dependency of reaction on burn-off was applied to the Arrhenius-type law of reaction rate. The multiplication factor can be expressed in the following way:

$$M(B) = \frac{R(B)}{R(0)} \tag{6.3}$$

Where:

B = Burn-off (%)

R(B) = Reaction rate at burn-off of B

R(0) = Reaction rate at zero burn-off

M(B) can be experimentally determined and may varied among graphite grades. For HTGR safety analysis, we are mainly concerned with graphite burn-off from 0% to 15%, however within the range of interested, the multiplication factor proposed by Kim et al. (2006) was derived from very limited data points. Accordingly, when incorporating his M(B) into a computer code, the accuracy of the resulting simulation becomes questionable over a large number of iterations.

In present study, the function of multiplication factor with respect to burn-off was developed based on the reported measurements of six oxidation experiments. The experimental conditions are summarized in Table 6.10.

Table 6.10 Experimental conditions of graphite oxidation experiment

Reference	Graphite	Temperature	Gas type
Kim (2006)	IG-110	1200˚C	CO_2, He
Fuller (1997)	IG-110	750˚C	Air
Contescu (2012)	IG-110	600˚C	Air
Wang (2012)	IG-110	600˚C	Air
Chi (2008)	IG-110	603˚C	Air
Choi (2011)	IG-110	600˚C	Air

As summarized in the table, graphite grade IG-110 was used in all six measurements. Five out of six measurements were obtained from the graphite oxidation reaction (C/O_2 reaction) except Kim's of which the M(B) was derived from the Boudouard reaction (i.e. C/CO_2). Kim explained that graphite oxidation and Boudouard reaction share similar patterns regarding the changes of internal surfaces with burn-off and hence, the M(B) derived from Boudouard reaction is applicable to the case of graphite oxidation.

Regarding the temperature, M(B) should be measured in "low" temperate regime (i.e. chemical kinetic controlled regime) where oxidation occurs uniformly through the whole depth of penetration. All experiments satisfy this requirement, except Fuller's, of which the reaction occurred in the in-pore diffusion controlled regime. In addition, Boudouard reaction has much higher activation energy than that of graphite oxidation. Hence, the 1200˚C in Kim's experiment is considered belonging to the chemical kinetic controlled regime of Boudouard reaction.

6.3.2 Modification of M(B)

Figure 6.15 shows the variation of graphite oxidation rates with the degree of oxidation measured by Contescu et al. (2012) [68]. The measurement was preformed according to ASTM standard method for air oxidation of graphite in regime I [68]. As shown in the figure, the measurement was highly fluctuated but the trend and the averaged values of reaction rate can be identified.

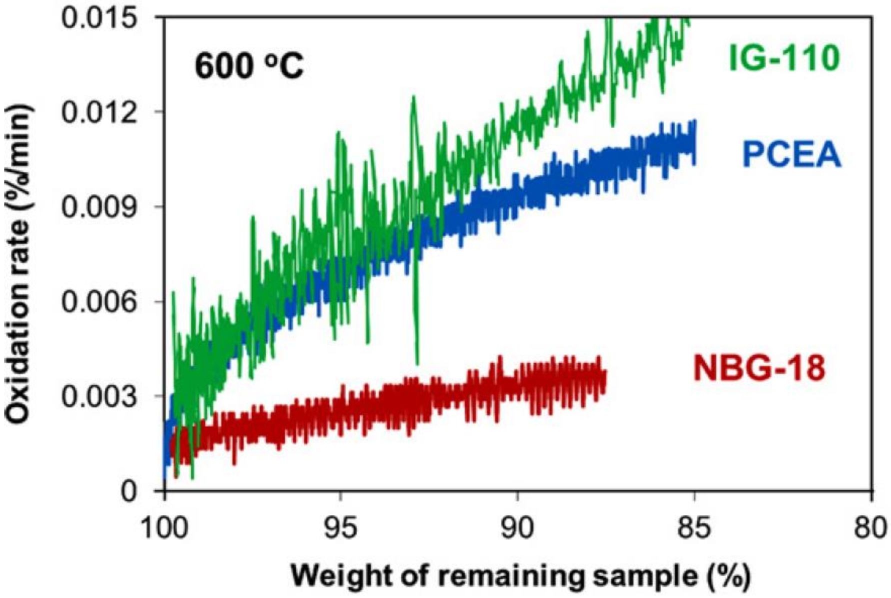

Figure 6.15 Oxidation rate measured by Contescu et al. (2012) [68]

M(B) can be calculated by divided the reaction rate by the initial reaction rate (i.e. reaction rate at 0.0% burn-off). The M(B) calculated from Contescu's data [68]is plotted in Figure 6.16. The M(B) of Kim (2006) [69] and Fuller (1997)[30] are also plotted for comparison. The blue line is a fitted curve proposed by Kim (2006) on the basis of his and Fuller's measurements. Figure 6.16 shows the good agreement among the three groups of data implying that the measurement of Kim, Fuller and Contescu are of good reliability.

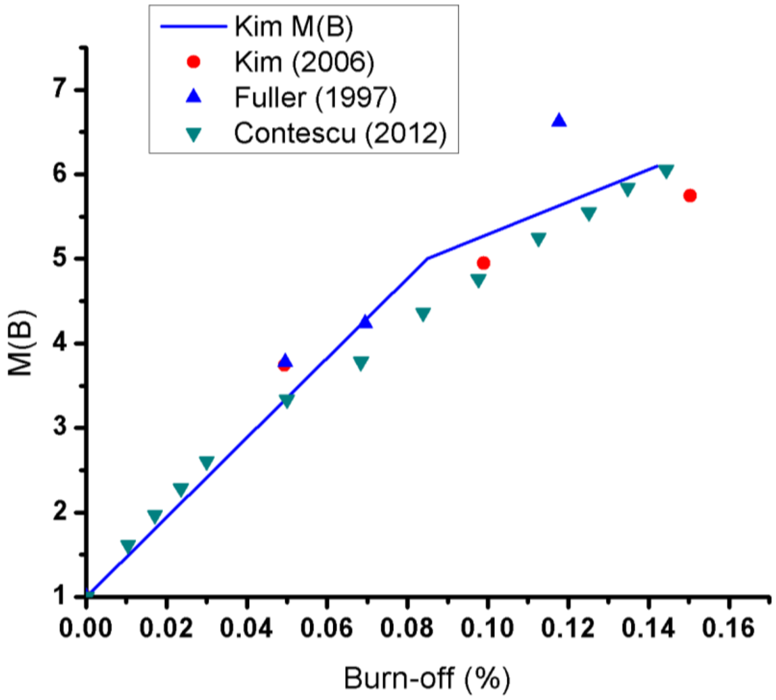

Figure 6.16. Variation of graphite oxidation rate with time (plotted from Fuller [30], Kim [69] and Contescu [68]'s experimental data)

Figure 6.17 illustrated the graphite weight loss measured by Wang et al. (2012) [70], Chi et al. (2008) [66] and Choi et al. [67]. Although the data were collected in similar experimental conditions, the results were scattered widely. Specifically, after 5 hours of oxidation, the weight loss measured by Choi was more than twice as high as that of Wang's. Starting from 10 hour, Wang's measurement deviated considerably from the other two groups of data. After 30 hours of oxidation, both Chi and Choi measured the weight loss of graphite to be approx. 6% whereas, in Wang's measurement, the weight loss reached almost 10%. One possible explanation is that the reaction rate is very low at 600˚C and thus any random disturbance during the experiment may have altered the oxidation rate leading to subtle variations of weight loss. The variations, however, will be accumulated and amplified over long time period (hours), resulting in significant deviations.

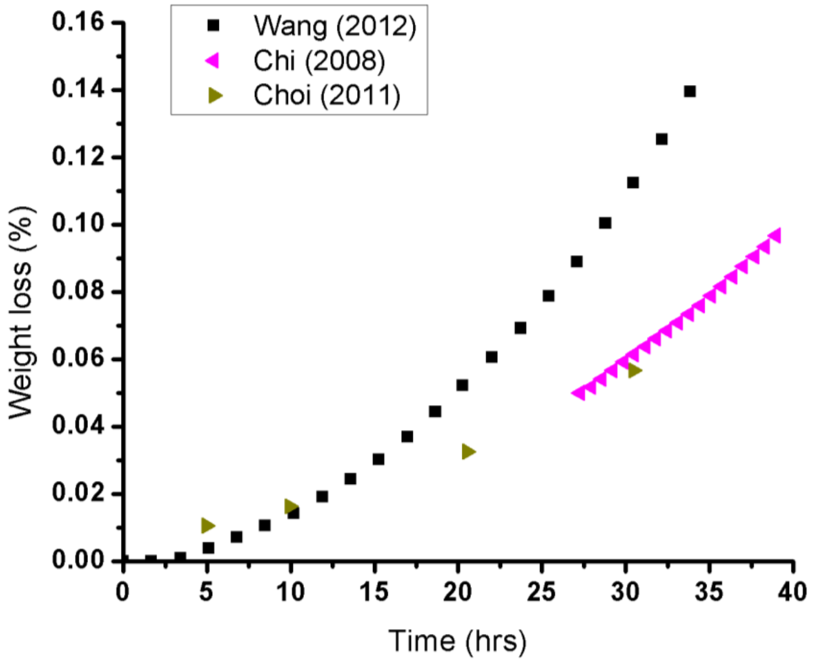

Figure 6.17. Weigh loss of graphite oxidized at 600˚C as a function of oxidation time (plotted from Wang, Chi and Choi's data [70,66,67])

The weight loss data in Figure 6.17 were fitted by polynomial expression of the form y = $a \cdot x^2 + b \cdot x +$ c. And the reaction rate (%/hrs.) is calculated by taking the derivative of the fitting function:

$$\text{Reaction rate}(\%/\text{hrs.}) = \frac{\Delta\text{weight loss}(\%)}{\Delta\text{time}} \tag{6.4}$$

Using Wang (2012)'s data as an example, after taking the derivative of the fitting function, we obtained the function of reaction rate over time as depicted in Figure 6.18. Then the x-axis (which represents time) was replaced by the corresponding weight loss (i.e. burn-off), which gave us the relationship between reaction rate and burn-off, (shown in Figure 6.19). Then M(B) could be computed by dividing the reaction rate to the initial reaction rate (reaction rate at 0% burn-off). The same method was adopted for calculating the M(B) utilizing Chi and Choi's data.

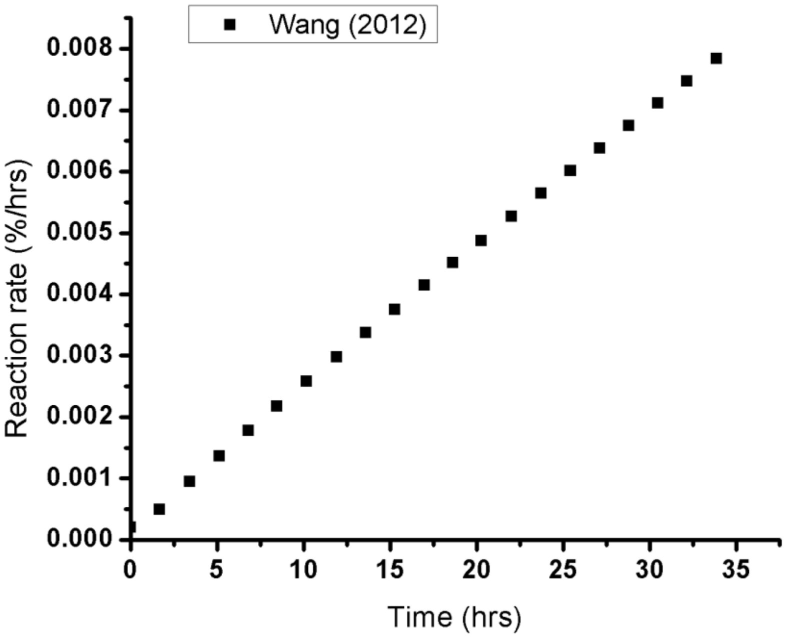

Figure 6.18 Reaction rate of graphite oxidized at 600˚C (computed from Wang's [70]'s experimental data)

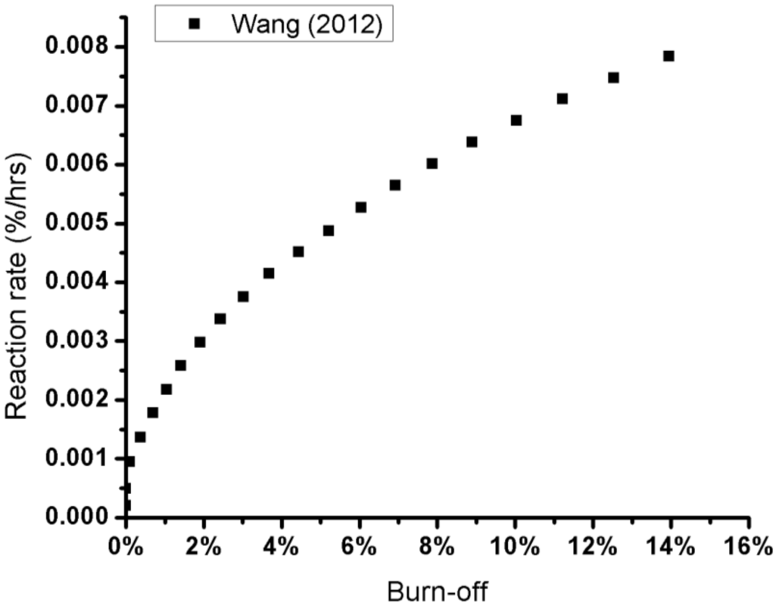

Figure 6.19. Variation of graphite oxidation rate with burn-off (plotted from Wang [70]'s experimental data)

Since the data points of weight loss were very limited in the initial period of oxidation, initial reaction rate calculated by taking derivatives of weight loss with respect to time may be not accurate, which may lead to biased results. As both Kim (2006) and Fuller (1997) reported that M(B) was approximately 3.75 at 5.0% burn-off, (3.75, 5.0%) was used to normalize these calculated M(B) data, of which the values are summarized in Figure 6.20.

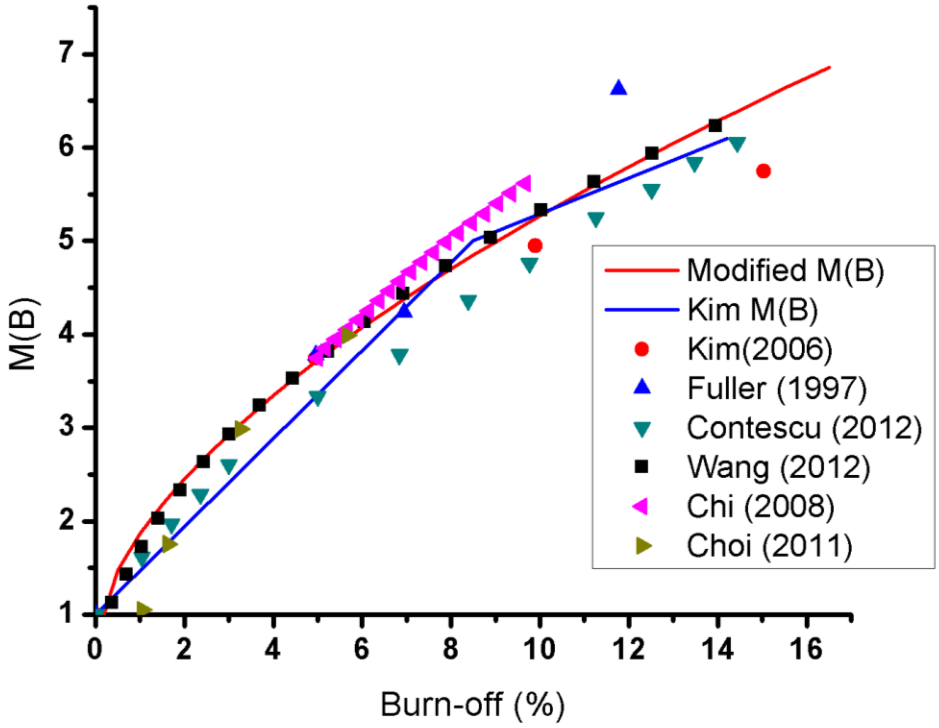

Figure 6.20 M(B) calculated from literatures

Finally, M(B) as a function burn-off was obtained by fitted to a power function which can be expressed as:

$$\text{Modified M(B)} = 18.0816 \times \text{burn} - \text{off}^{0.5988} + 0.7163 \tag{6.5}$$

Where

$$0 \leq \text{burn} - \text{off} \leq 15\%$$

In case of 0% burn-off, M(B) becomes 1.0. Since the above function was derived by fitting experimental data reported by various researchers, the modified M(B)does not go through the (0.0, 1.0) point. A minor correction was made to incorporate the point of (0.0,1.0). The final expression of modified M(B) is given as:

$$\text{Modifed M(B)} = \max(18.0816 \times \text{burn} - \text{off}^{0.5988} + 0.7163, 1.0) \tag{6.6}$$

7. Transient Oxidation Experiment

7.1 Experiment

7.1.1 Apparatus and experimental condition

Figure 7.1 illustrated the essential parts of the test setup. The apparatus mainly consists of stainless steel sealed chamber (20cm×20cm×40cm), electrodes, gas supply system, power supply system and data acquisition system. The sealed chamber had previously been filled with argon for providing an inert atmosphere. The IG-110 graphite specimen (denoted as inner graphite) was machined into cylindrical specifications of which the diameter and length were 9mm and 30mm respectively. In order to install the electrodes, cone-shaped holes were drilled on both the top side and bottom side of the inner graphite. Specifications of the graphite specimen and the pin-shaped electrodes were shown in Figure 7.2. A graphite tube (denoted as outer graphite) of 30mm length and an inner and outer diameter of 30mm and 46mm respectively were placed outside the inner graphite for the purposes of estimating the thermal energy radiated from the inner graphite and providing a stable gas flow boundary during the oxidation experiment. The inner and outer graphites were sandwiched between two ceramic isolation plates as shown in Figure 7.3.

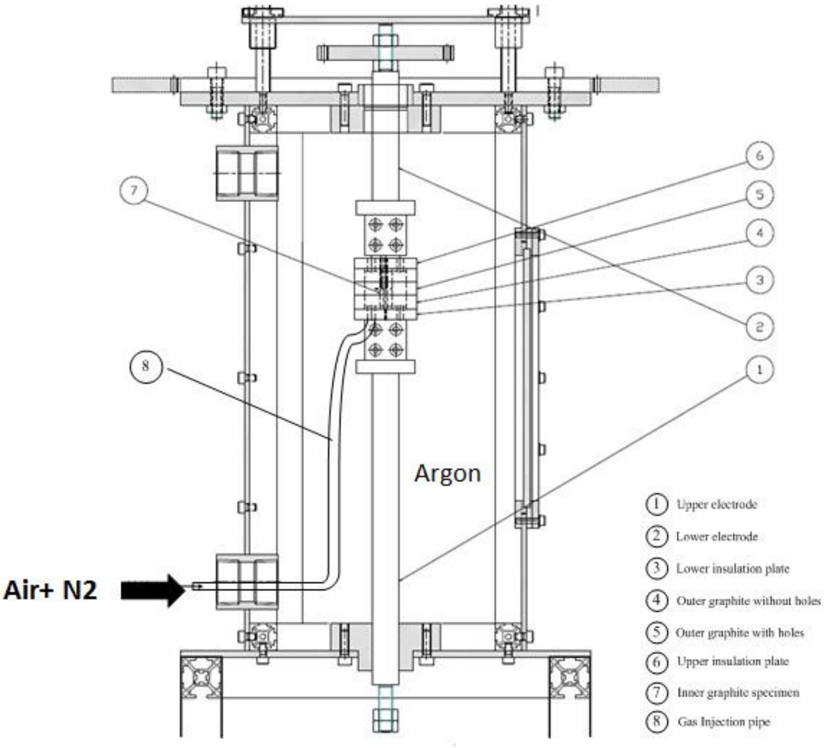

Figure 7.1 Schematic diagram of the experimental setup

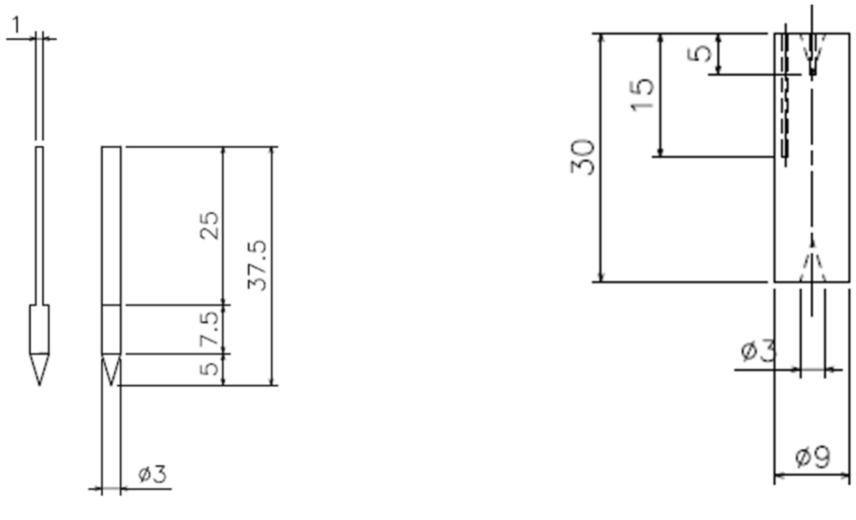

(a) Pin-shaped electrode (b) Inner graphite

Figure 7.2 Geometry specification of pin-shaped electrode and inner graphite

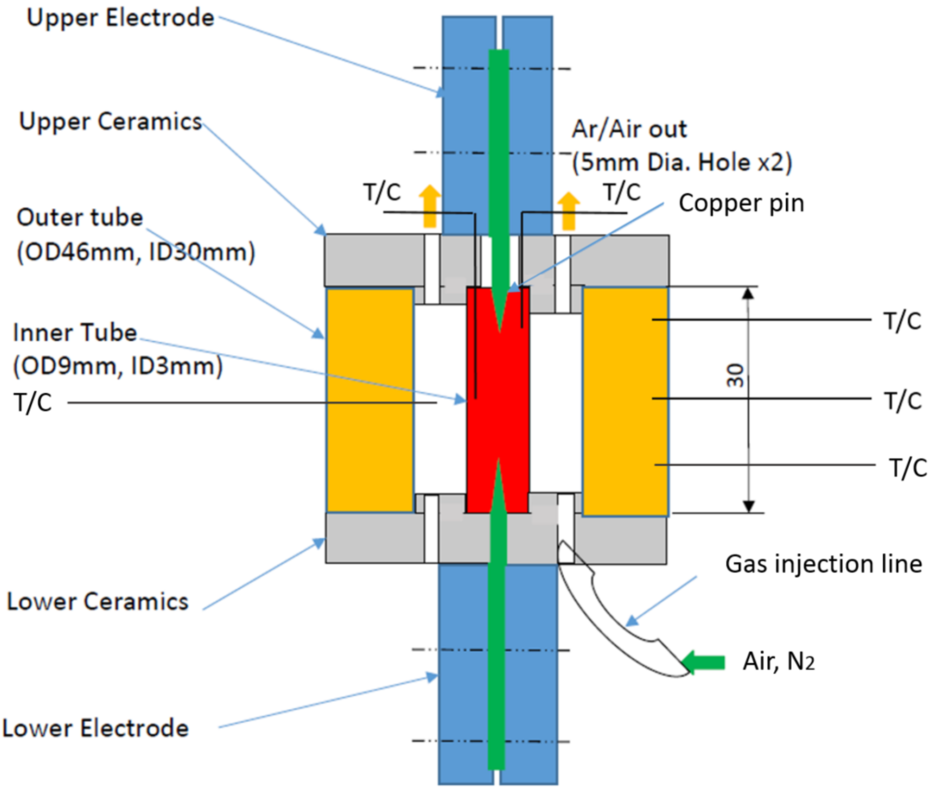

Figure 7.3 Schematic diagram of the test section

Three sets of k-type thermocouples were installed to measure the temperate of the test section. The first set was installed on the inner graphite (center and top) to measure the temperatures and to estimate the power dissipation due to heat losses in axial direction. Likewise, another set of thermocouples was installed on outer graphite. The last set of thermal couples was used to measure the temperature of gas mixture that flows through the annular region between the inner and outer graphite.

The design of the test section allows the two major phenomena that occur during air ingress to be captured. One is the graphite oxidation and the other is the thermal radiation. The total amount of graphite being gasified was estimated by the weight loss of graphite specimens. Joule heating generates heat solely in the inner graphite without affecting the gas mixture and outer graphite and hence radiation heat transfer can be calculated utilizing the temperate of inner and outer graphite.

During the experiment, the gas mixtures of air and N2 were injected from the bottom of the test section after a steady state temperature condition was attained. The total oxidation period lasted for 5 minutes. The temperature and oxygen concentration were selected as the main experimental variables. The experimental conditions are summarized in Table 7.1.

Table 7.1 Experimental conditions of the transient graphite oxidation experiment

Parameter	**Value**
Gas type	Air, N2
Inlet oxygen mole fraction	0%, 5%, 10%, 15%, 20%
Pressure	0.101 MPa
Flow rate of oxidant gas	1.0 SLPM
Flow rate of argon (environment)	25.0 SLPM
Graphite temperature	950˚C, 1150˚C
Oxidation period	5min

7.1.2 Experimental procedure

Preparation

Graphite:

The weights of inner graphite specimen were individually measured and recording utilizing electronic balance. White rubber gloves were worn whenever specimens were handed.

Argon environment:

Argon was continuously injected into the chamber at the flow rate of 25.0 SLPM. The oxygen concentration was monitored using an oxygen sensor (COSMOS XO-2200). Experiment starts after the oxygen concentration was stabilized below 0.5vol%.

Main test

During the experiment, after the injection of gas mixture, N2 of the same flow rate was injected into the test section to estimate the convective cooling induced by the flow. The experimental protocol used for the main test can be summarized as:

1) Heat up the inner graphite to target temperature, wait until the system reaches steady state.

2) Gas mixture injection: reactant gases of desired concentration (air and N2 mixture) were injected into the test section. The injection lasted for 5 minutes.

3) Adjust the voltage so that the inner graphite temperature recovers to the pervious steady state temperature.

4) N2 injection: N2 was injected into the test section. The injection lasted for 5 minutes.

5) Switch off the power supply.

6) Measure and record the weight of inner graphite. Calculate the weight loss.

7.2 Results and discussion

7.2.1 Weight loss

A total number of seven cases were conducted in present study. The experimental conditions are summarized in Table 7.2. The weight analyses of inner graphite before and after oxidation are presented in Table 7.3.

Table 7.2 Transient graphite oxidation tests

Case No.	Temperature (˚C)	O_2 mole fraction (%)	Oxidation period (mins)
1	950	21%	5
2	950	15%	5
3	950	10%	5
4	950	5%	5
5	1150	21%	5
6	1150	15%	5
7	1150	10%	5

Table 7.3 Weight loss of inner graphite

Case No.	Before (g)	After (g)	Weight loss (g)	Burn-off (%)
1	3.3614	3.2245	-0.1369	-4.1%
2	3.3694	3.2742	-0.0952	-2.8%
3	3.3590	3.2967	-0.0623	-1.9%
4	3.3658	3.3266	-0.0392	-1.2%
5	3.3634	3.1640	-0.1994	-5.9%
6	3.3493	3.1863	-0.1630	-4.9%
7	3.3682	3.2296	-0.1386	-4.1%

As shown in Table 7.3 Weight loss of inner graphite, the burn-off of inner graphite ranges from 1.2% to 5.9% after the 5 minutes oxidant gas injection. As expected, the highest burn-off was observed in Case 5 where the graphite temperature and O_2 mole fraction were 1150˚C and 21% respectively, whereas the lowest burn-off was found in Case 4 where the graphite temperature and O_2 mole fraction were 950˚C and 5% respectively.

7.2.2 Temperature transient

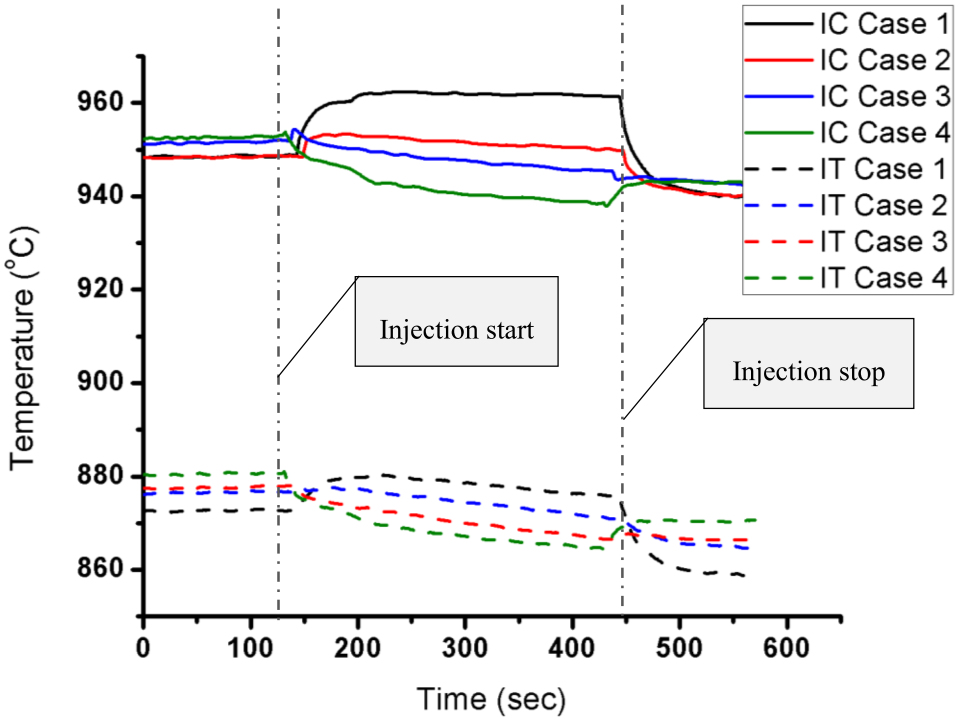

Figure 7.4 Temperature transient of Inner graphite during oxidant gas injection (950˚C)

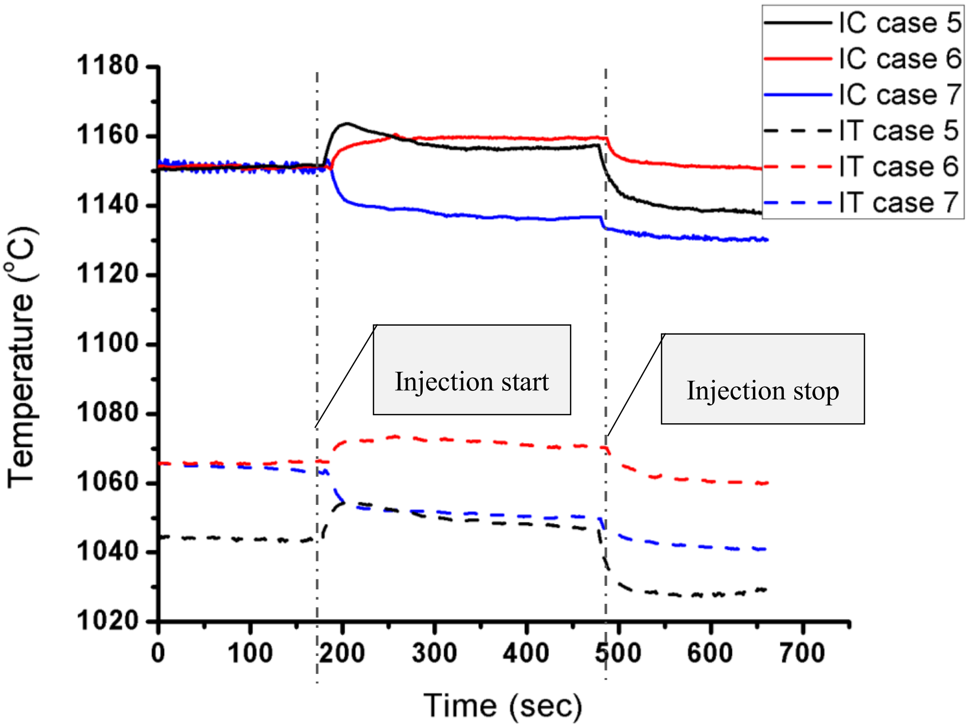

Figure 7.5 Temperature transient of Inner graphite during oxidant gas injection (1150˚C)

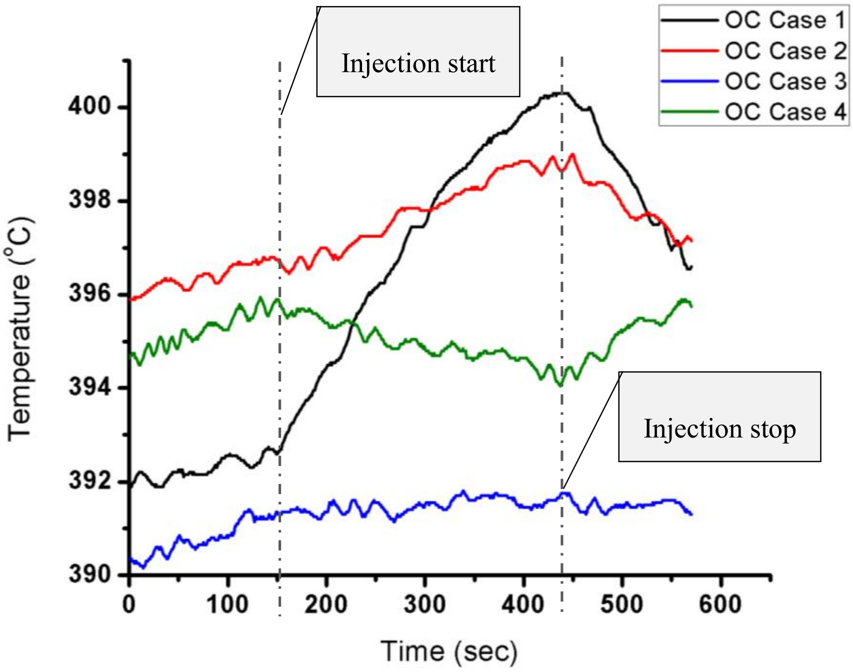

Figure 7.6 Temperature transient of Outer graphite during oxidant gas injection (950˚C)

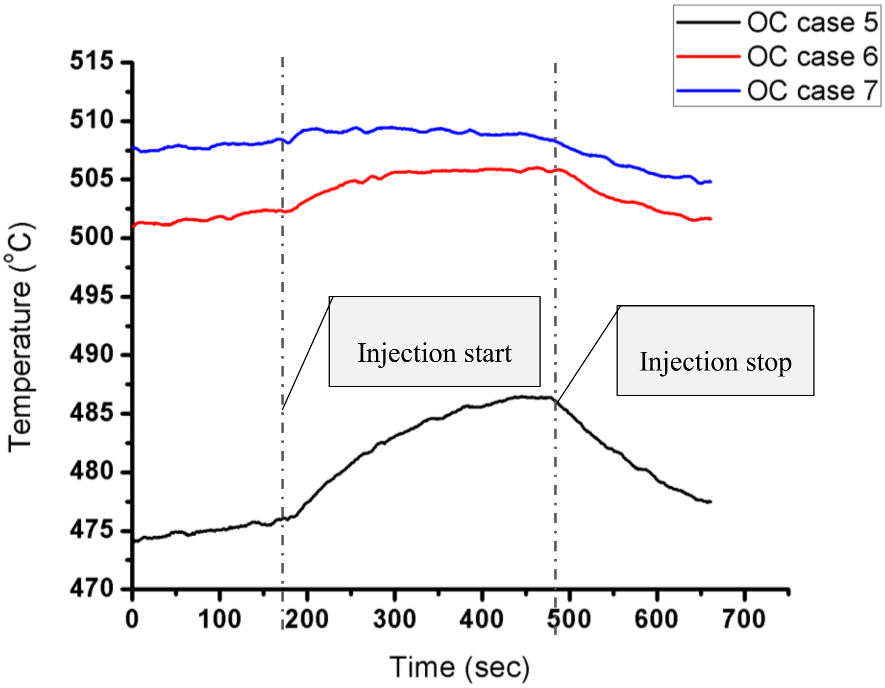

Figure 7.7 Temperature transient of Outer graphite during oxidant gas injection (1150˚C)

Figure 7.4 and Figure 7.5 illustrate the temperature transient of the inner graphite. The temperature transients of outer graphite are summarized in Figure 7.6 and Figure 7.7. “IC” indicates that the temperature was measured at the center of inner graphite. Likewise, “IT” and “OC” specify that the temperatures were measured at the top of inner graphite and the center of outer graphite respectively.

As shown in Figure 7.4, before the injection, the temperatures of the inner graphite were maintained at 950˚C. The injection started from 135sec and ended at 435sec. As injection started, the graphite temperature either increased, remained unchanged or degreased depending on the O_2 concentration. The inner graphite transient temperature behaviors are the result of heat balance of the power introduced by Joule heating, chemical heat generation, thermal radiation, convection and conduction, among which Joule heating and thermal radiation are believed to be the main heat generation and heat removal mechanisms. Among the four cases conduced at 950˚C, Case 1 and Case 2 of which the O_2 mole faction was 21% and 15%, experienced a temperature increase of

12.9˚C and 1.3˚C respectively. Meanwhile in Case 3 and Case 4 of which the O_2 mole faction was 10% and 5%, the temperature of inner graphite decreased by 6.0˚C and 14.3˚C respectively. For the three cases conducted at 1150 ˚C (Figure 7.5), the temperature measured at the center of inner graphite increases by 5.4˚C and 8.4˚C respectively for the 21% oxygen case and 15% oxygen case while decreases by 16.0℃ for the 10% oxygen case.

The temperate transients of outer graphite share the similar trends to their corresponding inner graphite. To be specific, as shown in Figure 7.6 and Figure 7.7, in Case 1 (O_2 21%, 950 ˚C), Case 2 (O_2 15%, 950˚C), Case 5 (O_2 21%, 1550 ˚C) and Case 6 (O_2 21%, 1150˚C) the outer graphite temperatures increased during gas injections, whereas in Case 3 (O_2 10%, 950˚C), Case 4(O_2 5%, 950˚C) and Case7 (O_2 10%, 1550 ˚C), the outer graphite temperatures slightly decreased or barely changed during the injections. This is because the primary heat source of outer graphite is the radiant energy emitted by inner graphite. And the increase/decrease of thermal radiation from the inner graphite led to the increases/decreases in temperature of outer graphite. The changes of graphite temperatures during the oxidant gas injection were summarized in Table 7.4.

Table 7.4 Change of graphite temperature during oxidant gas injection

Case No.	**Temp. (˚C)**	**O_2 mole fraction (%)**	**Inner graphite Center(˚C)**	**Inner graphite Top(˚C)**	**Outer Graphite Center(˚C)**
1	950	21%	12.9	3.5	7.7
2	950	15%	1.3	-5.3	2.2
3	950	10%	-6.0	-10.9	0.8
4	950	5%	-14.3	-15.9	-0.9
5	1150	21%	5.4	4.0	10.7
6	1150	15%	8.4	4.4	3.4
7	1150	10%	-16.0	-13.7	0.8

As shown in the table, compared to the 950 ˚C cases, the temperature of graphite spacemen in 1150 ˚C cases did not necessary experiencing more rapid temperature changes during oxidant gas injection. Even though the rate of exothermic oxidation reaction become faster, the thermal radiation rate was also capable of removing more heat for the graphite specimen at higher temperature.

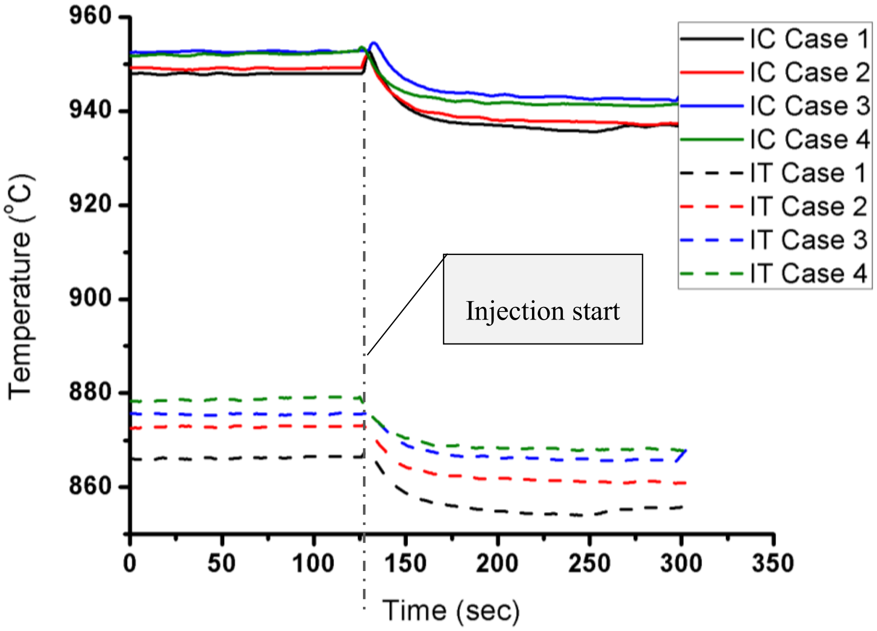

Figure 7.8 Temperature transient of Inner graphite during N2 injection (950˚C)

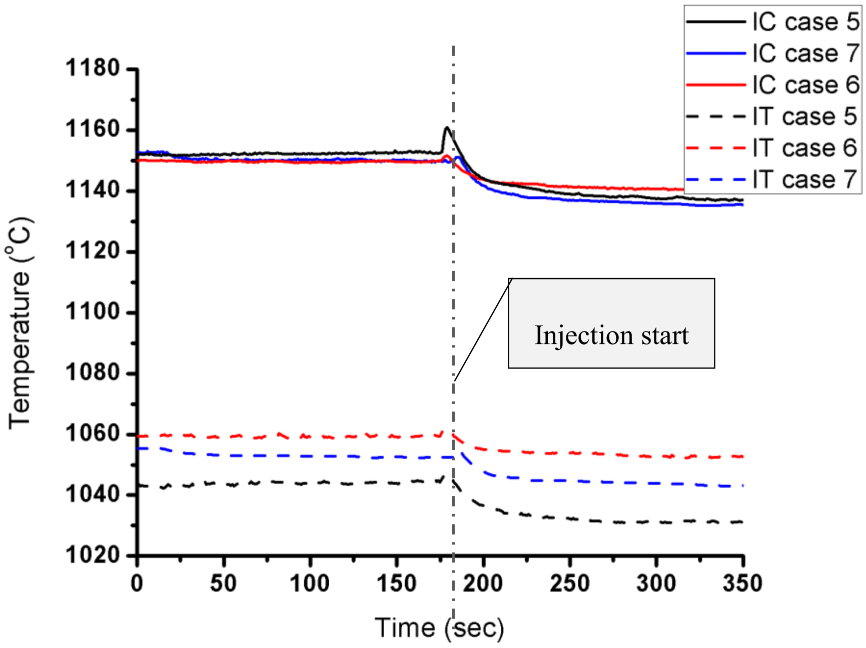

Figure 7.9 Temperature transient of Inner graphite during N2 injection (1150˚C)

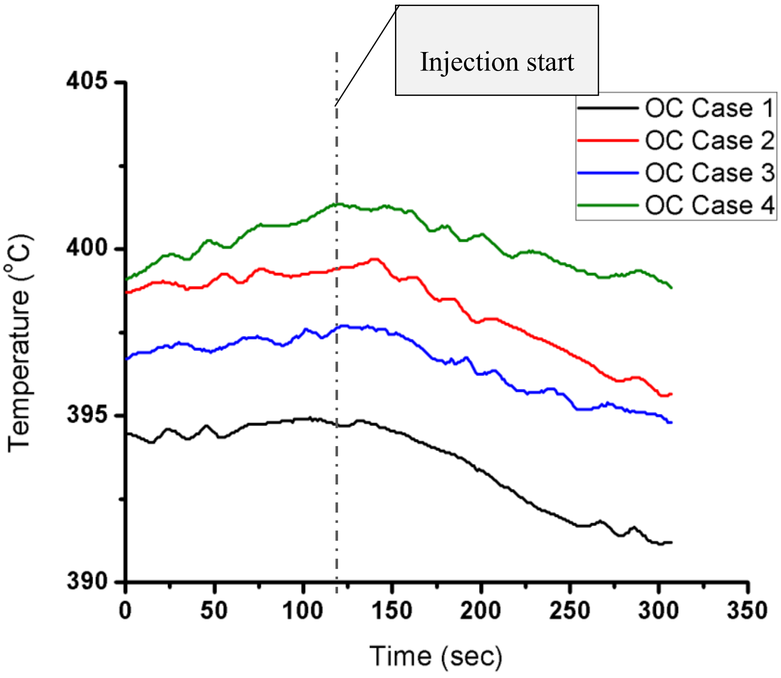

Figure 7.10 Temperature transient of Outer graphite during N2 injection (950˚C)

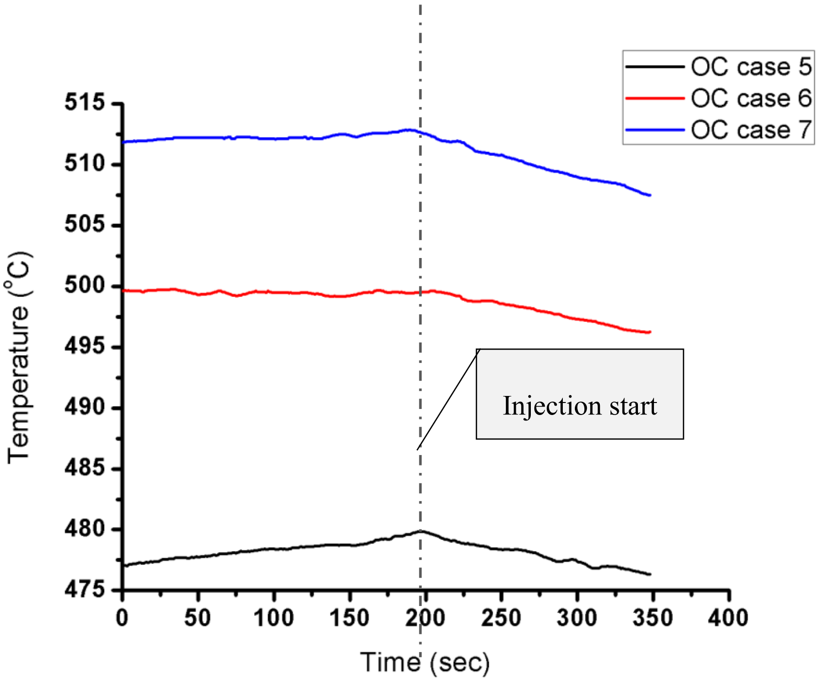

Figure 7.11 Temperature transient of Outer graphite during N2 injection (1150˚C)

N2 has similar thermodynamic properties to air but it is chemically inert to graphite. Therefore, after the oxidant gas injection, N2 of the same flow rate was injected into the test section to evaluate the convective cooling induced by the flowing fluid. Figure 7.8, Figure 7.9, Figure 7.10 and Figure 7.11 show the temperature transients of inner and outer graphite during the N2 injection. Inspection of figures shows that as soon as the injection started, temperature decrease was observed for both inner and outer graphite. For the inner graphite, the temperature decreased by approx. 12˚C whereas for the outer graphite, the temperature declined an average of 3.5˚C.

Table 7.5 Change of graphite temperature during N2 injection

Case No.	**Temp. (˚C)**	**Inner graphite Center(˚C)**	**Inner graphite Top(˚C)**	**Outer Graphite Center(˚C)**
1	950	-10.9	-10.7	-3.3
2	950	-11.7	-11.8	-3.0
3	950	-10.1	-9.8	-2.0
4	950	-11.8	-10.5	-1.3
5	1150	-15.1	-11.8	-3.8
6	1150	-9.4	-6.8	-4.1
7	1150	-15.2	-10.2	-6.7

In addition, there was a small amount of oxygen left in the injection pipe after the injection of oxidant gas. During the subsequent N2 injection, the residual oxygen carried by the N2 flow oxidized the inner graphite again which explains the temperature peaks found at the beginning of N2 injection.

7.2.3 Power input

As mentioned previously, the inner graphite was heated up by Joule heating which is the process by which the passing of an electrical current through a conductor produces heat. During oxidant gas injection, the inner graphite was gasified from external and thus its cross section area decreased with time. Consequently, the electrical resistance of inner graphite increased and the current passing through decreased. The power output of power supply decreased almost linearly with time as shown in Figure 7.12(950˚C) and Figure 7.13(1150˚C). Inspection of figures show that for case of higher oxygen concentration, the slope is also steeper which indicates the oxidation is more rapid. Figure 7.14 illustrates the power delivered to the test facility during N2 injection. The power remained constant since no reaction occurred.

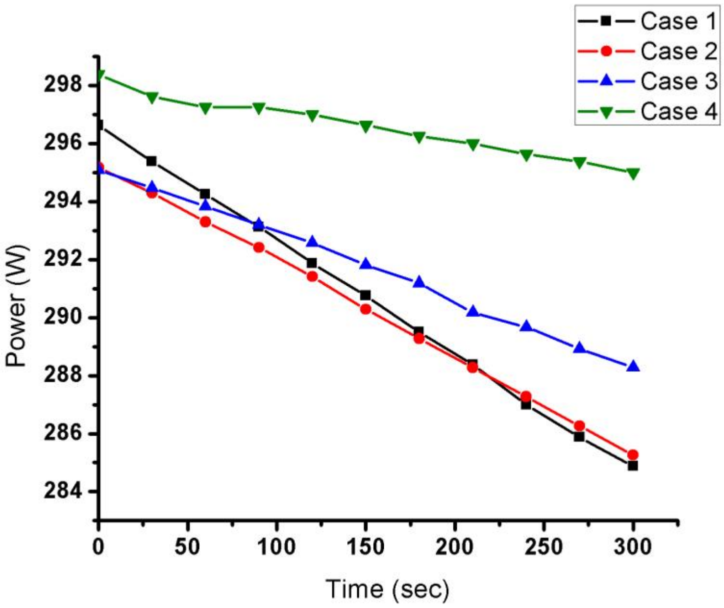

Figure 7.12 Power output from power supply during oxidant gas injection (950 ˚C)

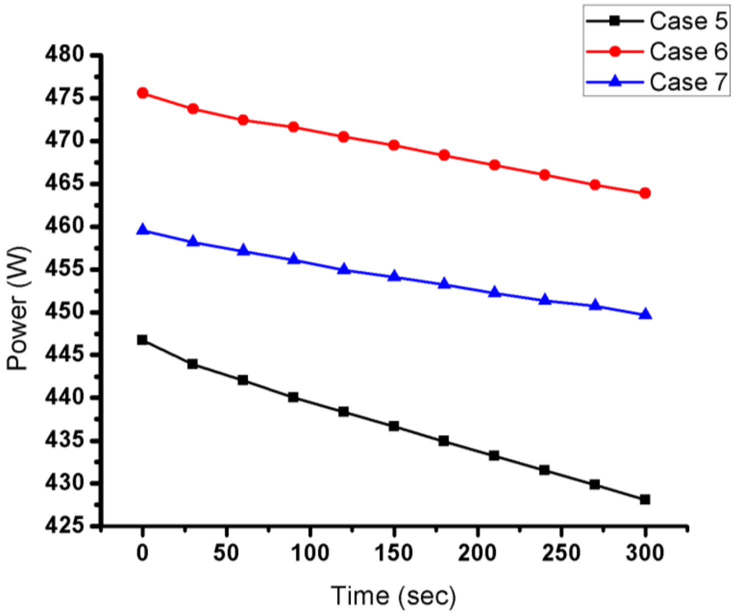

Figure 7.13 Power output from power supply during oxidant gas injection (1150 ˚C)

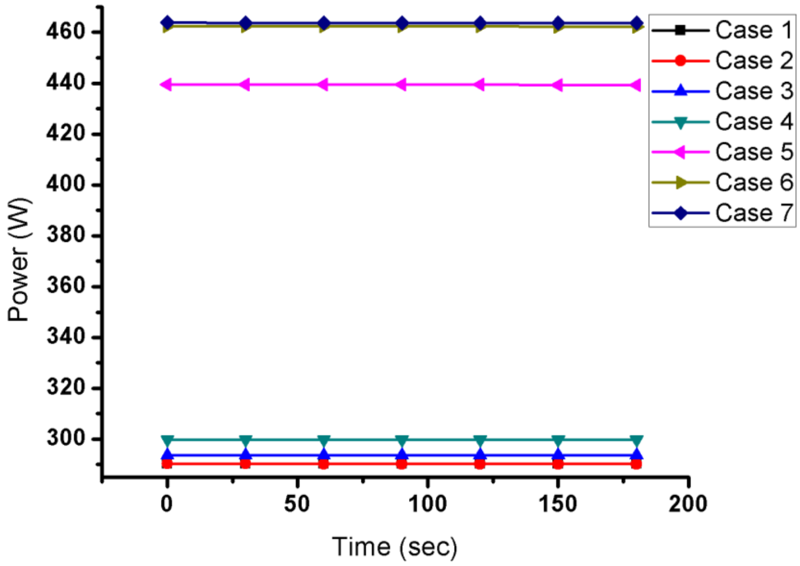

Figure 7.14 Power output from power supply during N2 injection

However, it needs to be pointed out that electrical resistance exists everywhere along the test facility and what we are concerned about is the power applied to the inner graphite. The heat dissipated by Joule heating in the inner graphite is estimated in the following manner (An example calculation is performed for the case of which the O_2 mole fraction is 21% and the temperate is at 1150℃):

According to Adachi.M et al. (1991) [71] the electrical resistivity of IG-110 is 829.17μΩ·cm at 950℃ and 855.62μΩ·cm at 1150℃.

The electrical resistance of the inner graphite prior to oxidation is:

$$R_{IG} = \rho \frac{L}{A} = 855.62\mu\Omega \cdot \mathrm{cm} \times \frac{3\mathrm{cm}}{\pi \times (0.9/2)^2} \\ = 4.035 \times 10^{-3}\Omega \tag{7.1}$$

The total electrical resistances of the system before oxidation is:

$$R_{tot} = \frac{U}{I} = \frac{1.55}{288.2} = 5.378 \times 10^{-3}\Omega \tag{7.2}$$

By subtract Equation (7.1) from Equation (7.2), the electrical resistance excluding inner graphite (denoted as system resistance) is expressed as:

$$\begin{aligned} R_{sys} &= R_{tot} - R_{IG} = 5.378 \times 10^{-3} - 4.035 \times 10^{-3} \\ &= 1.343 \times 10^{-3} \Omega \end{aligned} \tag{7.3}$$

The system resistance is assumed to be constant during the experiment. A summary of the inner graphite electrical resistance, system resistance and total electrical resistance is given in Table 7.6. As shown in the table, the system resistance, which is affected by specimen installation, was not constant in all cases. The electrical resistance of inner graphite at 950˚C and 1050˚C is 3.910mΩ and 4.035mΩ respectively, whereas the system resistance ranges from 1.327 mΩ to 2.217 mΩ. Approx. 65% to 75% of electrical resistance comes from the inner graphite, while the rest was produced by the other components of the test facility.

Table 7.6 Electrical resistance

Case No.	**Total (mΩ)**	**System (mΩ)**	**Inner graphite (mΩ)**	$\frac{\boldsymbol{Inner\ graphite}}{\boldsymbol{Total}}$ (%)
1	5.268	1.357	3.910	74.2%
2	5.336	1.426	3.910	73.3%
3	5.380	1.470	3.910	72.7%
4	5.273	1.327	3.910	74.2%
5	5.378	1.343	4.035	75.0%
6	5.690	1.655	4.035	70.9%
7	6.252	2.217	4.035	64.5%

And finally, the power applied to the inner graphite during gas injection is estimated using the following expression:

$$Pwr_{IG} = I^2(\frac{U}{I} - R_{sys}) \tag{7.4}$$

The power applied to the inner graphite during oxidant gas injection is plotted in Figure 7.15(950 ˚C) and Figure 7.16(1150 ˚C). The power applied to the inner graphite during N2 are illustrated in Figure 7.17. The power variation during the oxidant gas and N2 injection are summarized in Table 7.7.

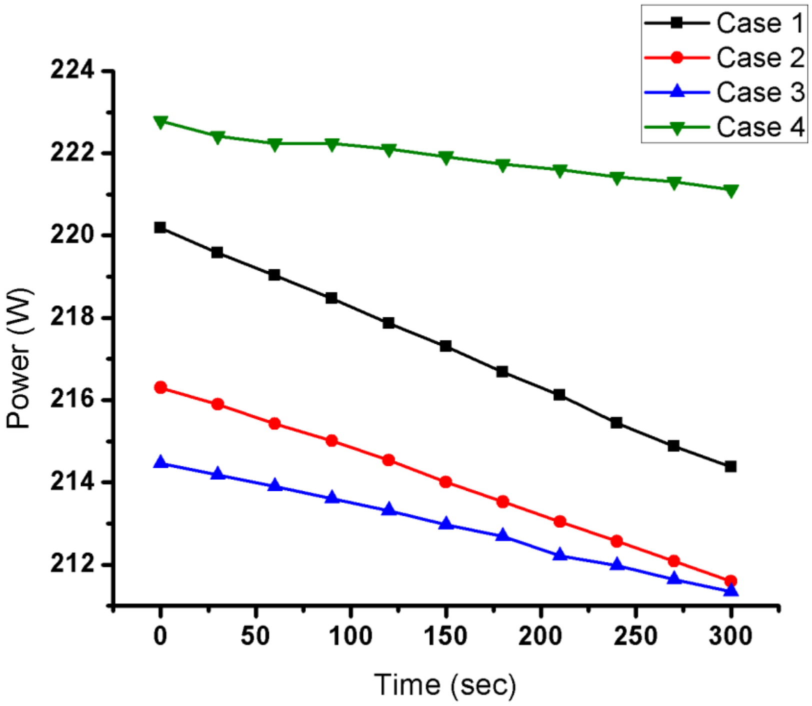

Figure 7.15 Power applied to the inner graphite during oxidant gas injection (950 ˚C)

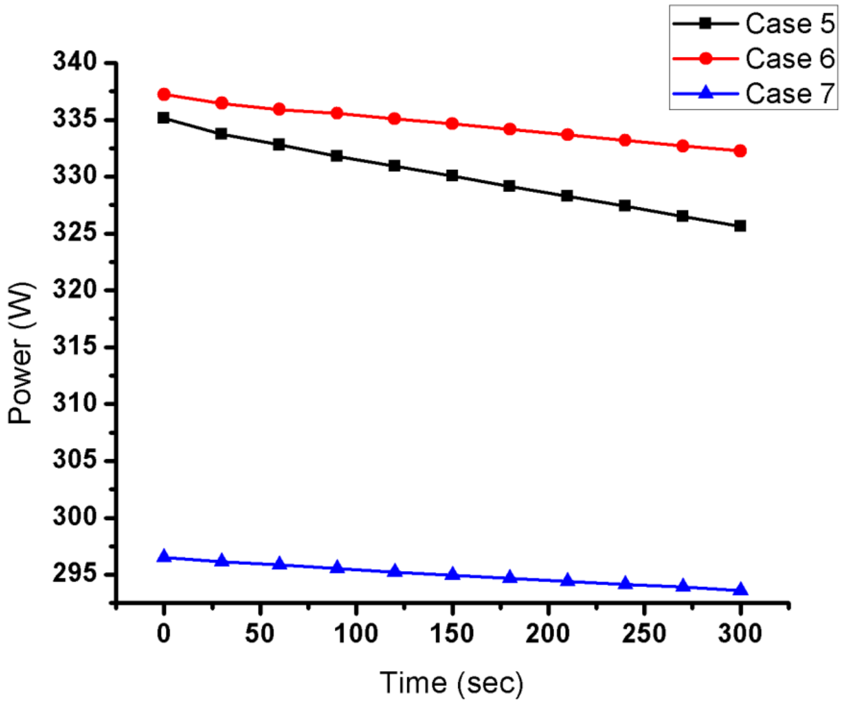

Figure 7.16 Power applied to the inner graphite during oxidant gas injection (1150 ˚C)

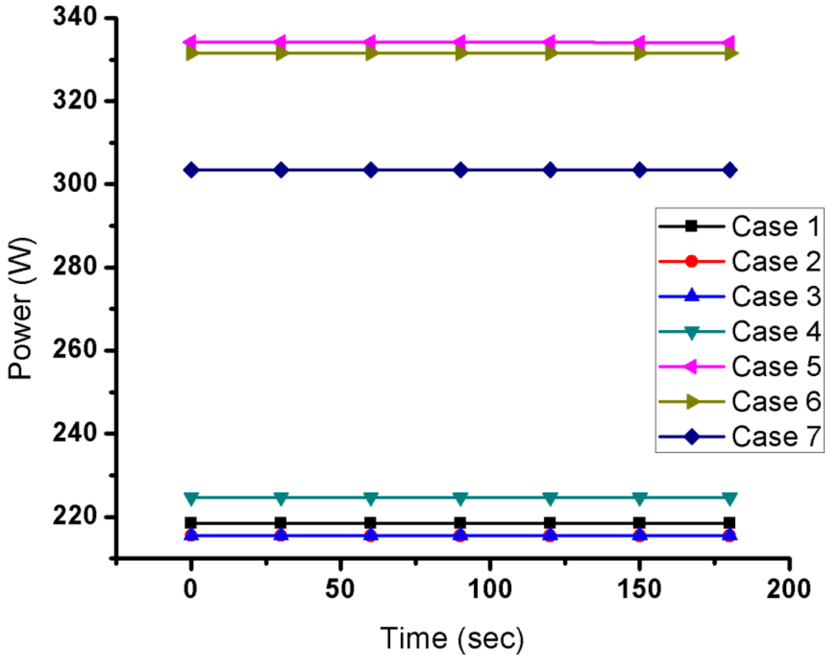

Figure 7.17 Power applied to the inner graphite during N2 injection

Table 7.7 Power variation during oxidant gas and N2 injection

Case No.	**Oxidant gas injection**		**N2 injection**	
	P_{tot} **(W)**	P_{IG}**(W)**	P_{tot}**(W)**	P_{IG}**(W)**
1	299.6~284.9	220.2~214.4	290.3	218.5
2	295.2~285.3	216.3~211.6	290.3	215.4
3	295.1~288.3	214.5~211.3	293.7	215.4
4	298.4~295.0	222.8~221.1	299.8	224.7
5	446.7~428.1	335.1~325.6	439.4	334.2
6	475.6~464.8	337.2~332.3	462.4	331.6
7	459.5~449.7	296.5~293.6	463.6	303.5

As summarized in the table, for the cases conducted at 950˚C, the power dissipated in the inner graphite was approx. 218W which composes 74% of the total input power whereas for the cases conducted at 1150 ˚C, an average of 323W was applied to the inner graphite, which accounts for approx. 71% of total input power.

7.3 Simulation

7.3.1 Overview

Simulation of the graphite oxidation experiment was performed in the following manner:

1) Star CCM+: Estimate the test section heat balance (especially the conduction in the axial direction) during N2 injection. Two cases were performed: one at 950˚C and another at 1150˚C.

2) RELAP5/SCDAP: Transient simulation with mass flow rate and pressure boundary conditions

As a 1-D system analysis code, the spectral dimension of conduction heat transfer calculation of RELAP5 is performed along the radial coordinate of cylindrical geometry whereas no temperature variations along the axial coordinate were estimated. However during the experiment, the conduction in the axial direction, including that from the inner graphite to the pin-shaped electrodes, from the inner and outer graphite to the ceramic plates cannot be ignored. The values of these heat losses were estimated in star CCM+ and removed from RELAP5/SCDAP simulation as heat sinks.

The simulations of graphite oxidation were performed using RELAP5/SCDAP in the following manners. Firstly, a steady state calculation was executed for the period before the gas injection using the mass flow rate and pressure as the inlet and outlet boundary conditions with additional inputs from star CCM+ including axial heat loses and ceramic plate temperatures. This would provide initial conditions for the transient calculation. The transient oxidation process was simulated by the code as the mass flow rate of the oxidant gas increased to 1.0 SLPM. The numerically predicted weight loss and transient temperature of graphite specimen were compared to the experimental measurement for complete model validation.

7.3.2 Star CCM+

Geometry

Star CCM+ was used to solve the problem numerically. The N2 flow was assumed steady and laminar. The laminar model, segregated flow and the segregated fluid temperature were used. For the solid domain, segregated solid energy and S2S (surface to surface) radiation model were used. An overview of the test section geometry is illustrated in Figure 7.18. The geometry consists of seven parts including the inner graphite, outer graphite, top/bottom ceramic plates, top/bottom pin-shape electrodes and the N2 flow.

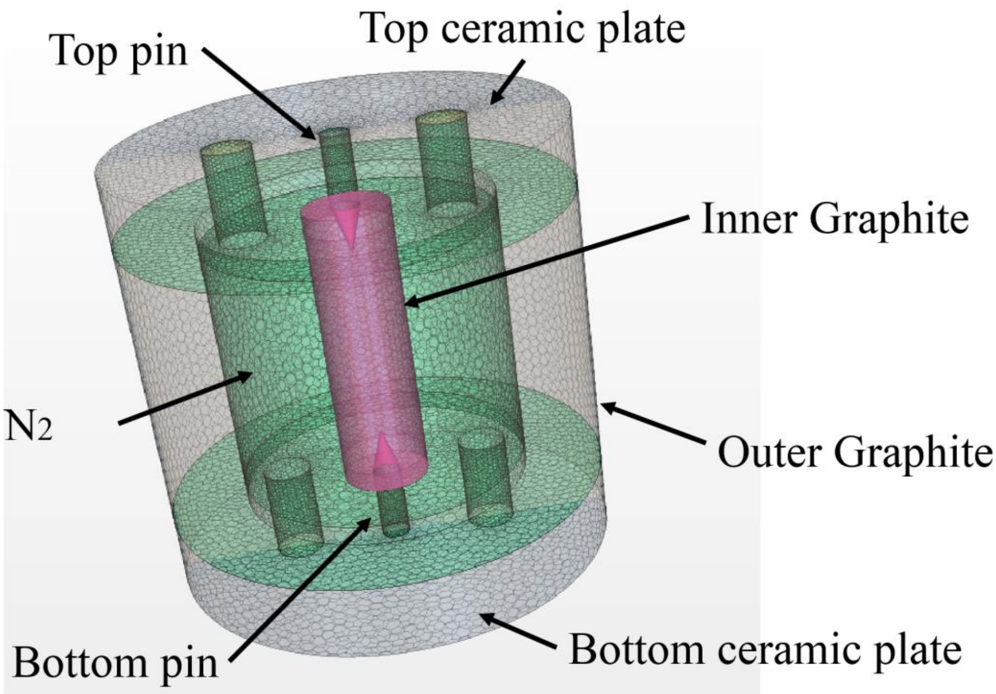

Figure 7.18 Geometry of the test section

Computational mesh

Figure 7.19 shows the computational mesh for both the solid domain and the fluid domain. The mesh used to solve this problem consisted of 116908 cells for the solid domain and 71100 cells for the fluid domain respectively after performing a grid independent study. Specifically, for the solid domains, we opted for the polyhedral cells, whereas in the fluid domain, a volume mesh composed of prismatic cell layer next to the wall boundaries and a polyhedral mesh elsewhere were created. The prismatic cell layers created on the interface of the solid and fluid will help capture the boundary layer effects and heat transfer near wall boundaries. The meshes are fully conformal at all interfaces which enable a faster and more accurate computation.

For the fluid domain, the mass flow rate based on the experimental measurements was applied to the inlet. Static atmospheric pressure was considered at the outlet. For the solid domains, environmental boundary was used for the surfaces of outer graphite, top and bottom ceramic plates which were exposed to the argon environment. Table 7.8 and

Table 7.9 summarize the boundary conditions and initial conditions applied. The interface settings are summarized in Table 7.10. Default material properties of N2, glass and copper provided by star CCM+ material library were used for the domains of N2, ceramic plates and pin-shaped electrodes whereas, custom material properties, which are summarized in Table 7.11 [72], were defined for inner and outer graphites. Volumetric heat source was applied within the volume of inner graphite domain, of which the values were 215W and 331W for the 950˚C case and the 1150˚C case respectively.

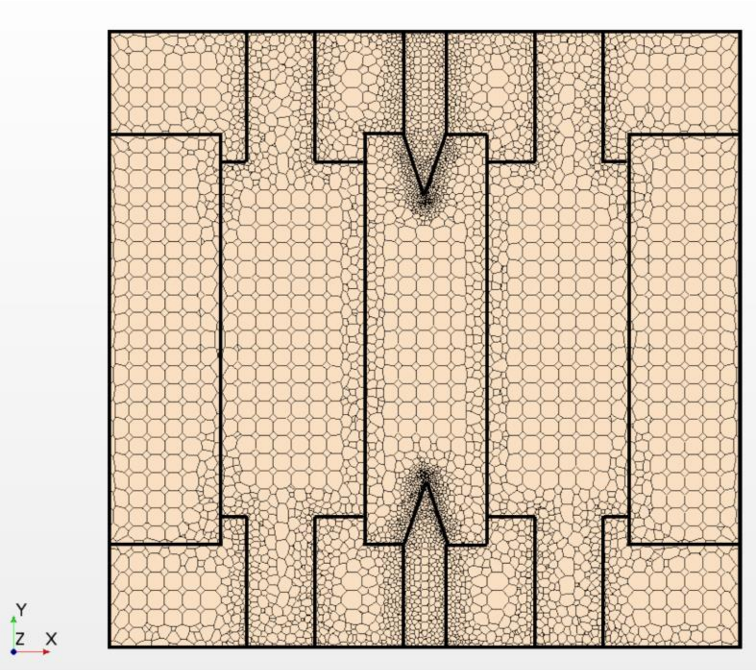

Figure 7.19 Cross sectional view of the mesh

Table 7.8 Boundary conditions

Parameter	Value
Flow inlet	$\dot{m} = 1.8908 \times 10^{-5} kg/s \quad T_g = 300K$
Flow outlet	$P = 0.101\ MPa$
Environmental boundary	$h_{conv} = 0.0 W/m^2K \quad T_{Env.} = 309K$

Table 7.9 Initial conditions

Domains	**Value**
Inner graphite	1223K
Outer graphite Top/Bottom ceramic plates Top/Bottom pins	$773K$
N2 flow	$T_g = 300K \quad \dot{m} = 1.8908 \times 10^{-5} kg/s$

Table 7.10 Interface settings

Type	**Location**	**Setting**
Solid/Solid (conduction)	Inner graphite/ceramic plates Outer graphite/ceramic plates	$r_{contact} = 0.002 m^2K/W$
	Inner graphite/pins Ceramic plates/pins	$r_{contact} = 0.000 m^2K/W$
Solid/Fluid (convection)	Inner graphite/N2 flow Outer graphite/ N2 flow	Default
Solid/Fluid/Solid (radiation)	Inner graphite/outer graphite Inner graphite/ ceramic plates Outer graphite/ ceramic plates	$\varepsilon_c = 0.950$ $\varepsilon_{ig} = 0.832$

Table 7.11 Material properties of graphite [72]

Parameter	**Value**	
Density (kg/m^3)	1750.0	
Heat capacity (J/kgK)	1100.0	
Thermal conductivity (W/mK)	580K	88.3
	676K	78.6
	777K	70.1
	876K	64.7

	975K	60.0
	1073K	56.3
	1172K	52.6
	1277K	49.3
	1388K	46.3
	1519K	43.9

Results: Temperature

During the experiments, N2 injection was performed for seven times: four times were conducted at the inner graphite temperature of approx. 950˚C (denoted as 950˚C case) whereas three times were conducted at the inner graphite temperature of approx. 1150˚C (denoted as 1150˚C case). Figure 7.20 shows the simulation results of the temperature fields. The locations of the thermocouple as well as their temperatures computed by star CCM+ are shown in the figure. A comparison between the code-simulated temperatures and experimentally measured temperatures are summarized in Table 7.12.

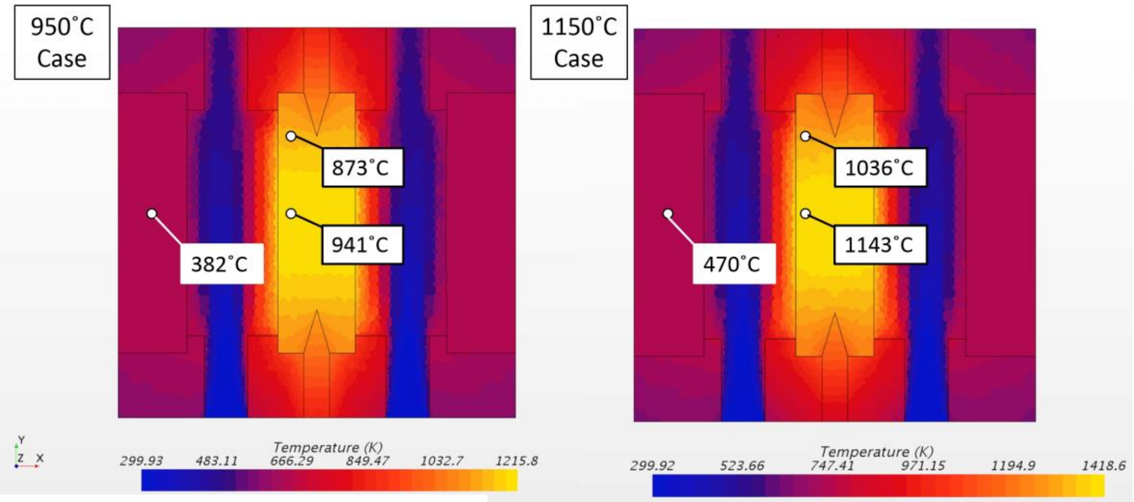

Figure 7.20 Temperature field of the test section (with thermocouple locations)

Table 7.12 Comparison between the code-simulated and experimentally measured temperature

Location		Experiment (˚C)	Star CCM+ (˚C)
950 ˚C case	Inner Graphite center	937.1~940.3	941.0
	Inner Graphite Top	855.6~868.5	873.0
	Outer Graphite Center	391.6~399.25	382.2
1150˚C case	Inner Graphite center	1134.8~1137.4	1142.6
	Inner Graphite Top	1032.3~1052.4	1036.1
	Outer Graphite Center	475.0~505.8	470.0

As shown in the table, the comparisons show a good quantitative similarity between the star CCM+ and the experimental data. However, with the given power input (Joule heating) the inner graphite temperature profile indicated by star CCM+ calculation was higher than that of the experimental data. Meanwhile the predictions of outer graphite temperature was lower than that of the experimental data. The maximum deviation between the CFD and experimental data was within 10 ˚C.

Results: Heat balance

The heat balance of the inner and outer graphite are illustrated in Figure 7.21 (950˚C case) and Figure 7.22 (1150˚C). The heat source of the inner graphite was the current-induced Joule heating whereas the heat removal mechanisms include conduction heat transfer to the pins and ceramic plates, thermal radiation to the outer graphite and ceramic plates and convective heat transfer to the N2 flow. The outer graphite did not have internal heat source, instead, the energy addition was due to the thermal radiation from the inner graphite. The heat removal was by means of conductive heat transfer to the ceramic plates, thermal radiation to the environment and the convection cooling of the N2 flow.

The percentages of heat loss via various heat transfer mechanisms at 950˚C were similar to that of 1150˚C. For the inner graphite, the majority of the heat loss, i.e. 68% ~72%, was due to conduction, wherein approx. 10% was through the ceramic plates and 90% was through the pin-shaped electrodes. 26%~30% of heat removal was contributed by radiative cooling while convections only accounted for approx. 2% of heat removal. For the outer graphite, the percentage of heat removal via thermal radiation was 73%~78%. The rest was mostly by conductive heat transfer to the ceramic plates. The cooling effect of flow was very weak and could be generally ignored.

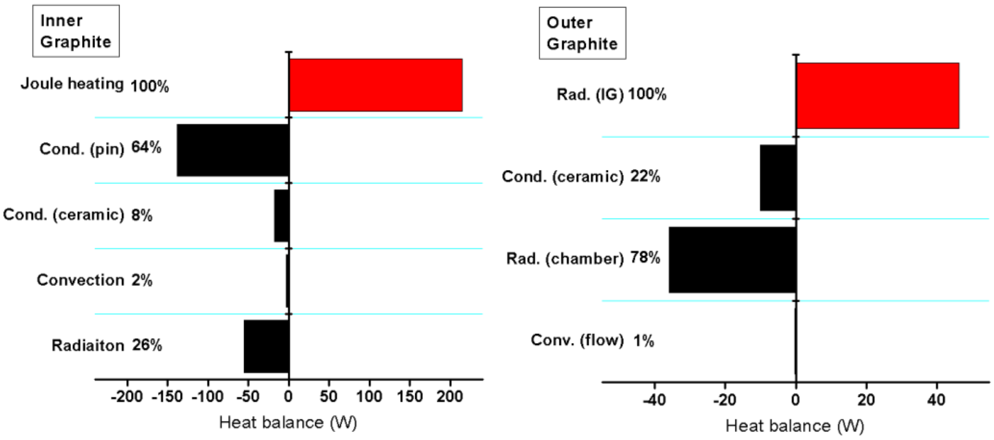

Figure 7.21 Heat balance of inner and outer graphite (950 ˚C)

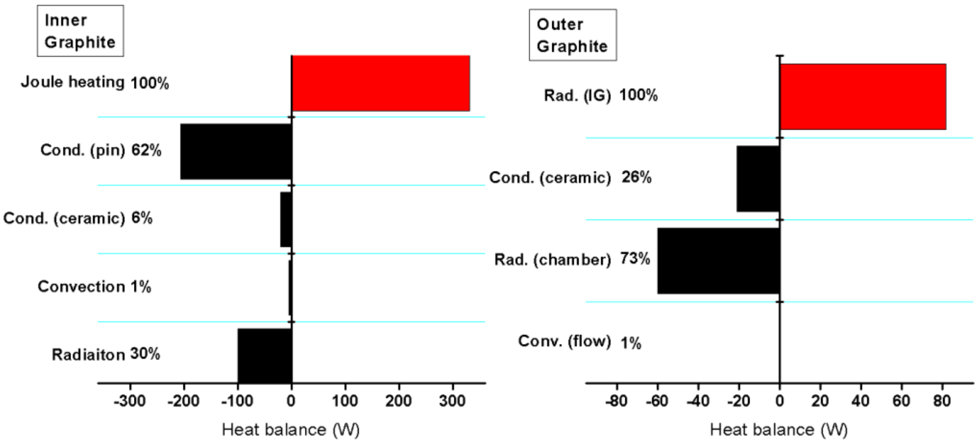

Figure 7.22 Heat balance of the inner and outer graphite of the (1150 ˚C)

7.3.3 RELAP5/SCDAP

RELAP idealization and simulation conditions

A RELAP idealization was constructed based on the test section. As shown in Figure 7.23, the annular flow path between the inner and outer graphites was represented by an ANNULUS component, split into 3 equally sized control volumes 0.01m in length. The argon flow path (i.e. argon environment), which was between the outer surface of outer graphite and inner surface of metal chamber, was modeled as a PIPE component. The inner graphite was represented by a single HEAT STRUCTURE consisting of three axial and five radial nodes, with its outer radial surface attached to the thermal hydraulic ANNULUS components. Similar to the inner graphite, the outer graphite was also represented by a HEAT STRUCTURE of three axial and five radial nodes, of which the inner radial surface was coupled to the ANNULUS component whereas the outer radial surface was attached to the PIPE component. The properties of IG-110 graphite were input as shown in Table 7.13. A power table was coupled to the axial node of inner graphite of which the values were estimated by subtracting the conductive heat losses from Joule heating. The top and bottom ceramic plates were also included in the model. An 8×8 view factor matric was defined in the input decks for capturing the two dimensional radiation heat transfer among the inner graphite, outer graphite and ceramic plates. I should be noted that the temperatures of the ceramic plate were not computed in RELAP due to the complex geometry. Instead, the temperatures were estimated by star CCM+ and then applied to RELAP. The metal chamber was modeled as a HEAT STRUCUTRE component. The temperature was set to 309K, which was the temperature measured on the metal chamber inner wall during the experiments. A 6×6 view factor between the surfaces of outer graphite and metal chamber was input to RELAP for computing the one dimensional radiation exchange. Emissivities of 0.832, 0.95 and 0.99 were used for the graphite specimens, ceramic plates and metal chamber respectively.

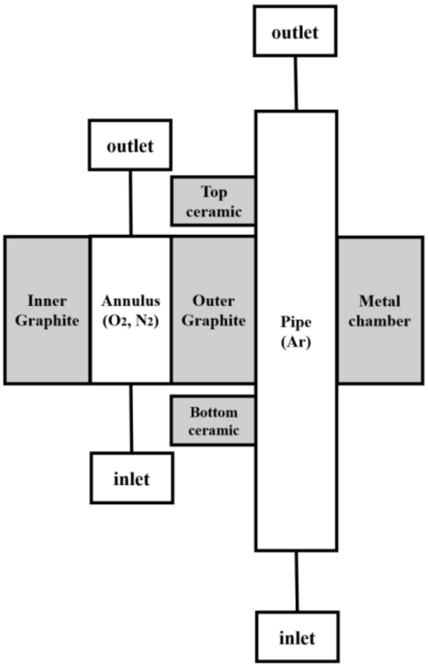

Figure 7.23 Thermal hydraulic idealization of the test section (grey: heat structure; white: thermal hydraulic volume)

Table 7.13 IG-110 material properties input to RELAP

Temperature (K)	Thermal conductivity (W/mK)	Volumatic heat capacity (J/m^{3}K)
573.15	88.9	2361172.01
773.15	71.9	2793362.97
973.15	60.2	3053849.36
1173.15	52.2	3222829.66
1373.15	46.8	3339250.10
1573.15	43.1	3423273.45
1773.15	40.8	3486132.68
1973.15	40.0	3534499.44

The conditions of the experiment were input into the RELAP model by setting the values of boundary conditions of the thermal hydraulic and heat structure components corresponding to the experimental data and star CCM+ results. The inner graphite power, as mentioned previously, could not be measured directly, and therefore, was calculated based on the voltage and current data measured in the experiment, the conduction heat losses estimated by star CCM+ and then slightly adjusted for matching the REALP temperature predictions with that of the experimental measurements. A mass flow rate of $0.5908 \times 10^{-5} kg/s$ was adopted for the annulus to represent the vertical natural convection occurring during the steady state phase and it is found that any further decrease of mass flow rate no longer change the convective heat transfer coefficient. The values applied are shown in Table 7.14.

A steady state calculation (i.e. the period before gas injection) was performed first, which was used as the initial conditions for the transient calculation (i.e. the period during gas injection). The transient calculation started as the mass flow rate of the oxidant gas in the annulus channel increased to $1.8908 \times 10^{-5}\mathrm{kg/s}$ and was continued for 300sec.

Table 7.14 Steady state boundary conditions for the experiment

Parameter	**Value**	
Inlet mass flow rate	Annulus channel	$0.5908 \times 10^{-5} kg/s$
	Argon channel	$6.74 \times 10^{-4} kg/s$
Inlet pressure	0.101 MPa	
Inlet gas composition	Annulus channel	O_2: 5%, 10%,15%,21%
	Argon channel	Ar: 100%
Outlet pressure	0.101 MPa	
Inner graphite power	950˚C case	69.0W

		(Joule heating: 215.0W; Conduction heat losses: -146.0W*)
	1150˚C case	127.0W (Joule heating: 331.0W; Conduction heat losses: -204.0W*)
Outer graphite conduction heat loss in axial direction	950˚C case	-10.0W*
	1150˚C case	-21.1W*
Top ceramic plate temperature	950˚C case	451˚C*
	1150˚C case	542˚C*
Bottom ceramic plate temperature	950˚C case	443˚C*
	1150˚C case	533˚C*

Asterisk indicates that the parameter were computed in star CCM+

Results: N2 injection

To ensure that the simulation scheme discussed above was validated for analyzing the experiments, steady-state and transient simulations were firstly preformed for N2 injection where no oxidation reaction occurs. The temperature transients of inner graphite (center) are depicted in Figure 7.24

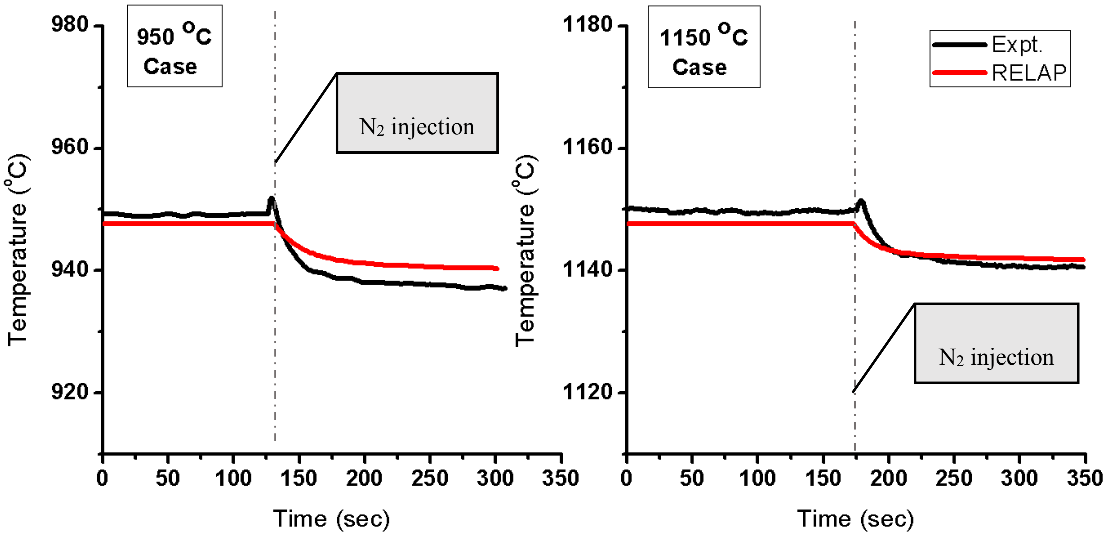

Figure 7.24 Temperature transient of inner graphite (center) during N_2 injection

When the injection started, the temperature of inner graphite decreased due to the convective cooling of the N2 flow, which could be observed in the simulations. According to the measurement, temperature of inner graphite (center) was decreased by 10˚C ~12˚C in the 950˚C case and 10˚C~15˚C in the 1150˚C case whereas in simulations, for both cases, the temperatures declined by 8˚C. Although the N2 flow was of very low Reynold number (due to the low flow rate and small length scale of the test section), certain levels of turbulence exist due to the change of cross section areas of inlet, annulus and outlet which leads to a higher convective heat transfer rate in the experiments compared to that of predicted by RELAP using the correlation developed for laminar flow. This is believed to be the reason why RELAP predicted smaller temperature variations compared to that of the experiments.

A comparison between the RELAP simulated temperatures and experimentally measured temperatures are given in Table 7.15. As shown in the table, for the inner graphite, the temperatures predicted by RELAP5 are in consistent with the experiment data whereas for the outer graphite, at the given experimental conditions, the temperature predicted by RELAP was 20˚C ~ 40˚C lower than that of measured in the experiments. To provide an insight into why RELAP under predicted the outer graphite temperatures, comparisons of the heat balance computed by star CCM+ and RELAP were depicted in Figure 7.25 (950˚C case) and Figure 7.26 (1150˚C case).

Table 7.15 Comparison between the RELAP5 predicted and experimentally measured temperature

Location		**Experiment (˚C)**	**RELAP5/SCDAP (˚C)**
950 ˚C case	Inner Graphite center	937.1~940.3	940.0
	Inner Graphite Top	855.6~868.5	861.2
	Outer Graphite Center	391.6~399.25	355.1
1150˚C case	Inner Graphite center	1134.8~1137.4	1141.0
	Inner Graphite Top	1032.3~1052.4	1051.1
	Outer Graphite Center	475.0~505.8	454.0

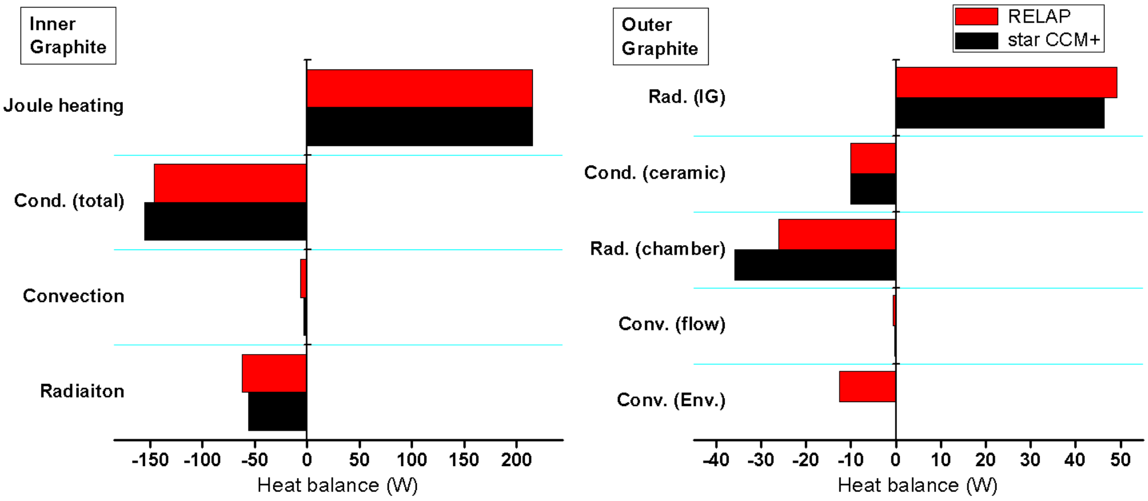

Figure 7.25 Comparison between the RELAP5/SCDAP and star CCM+ predicted heat losses (950˚C)

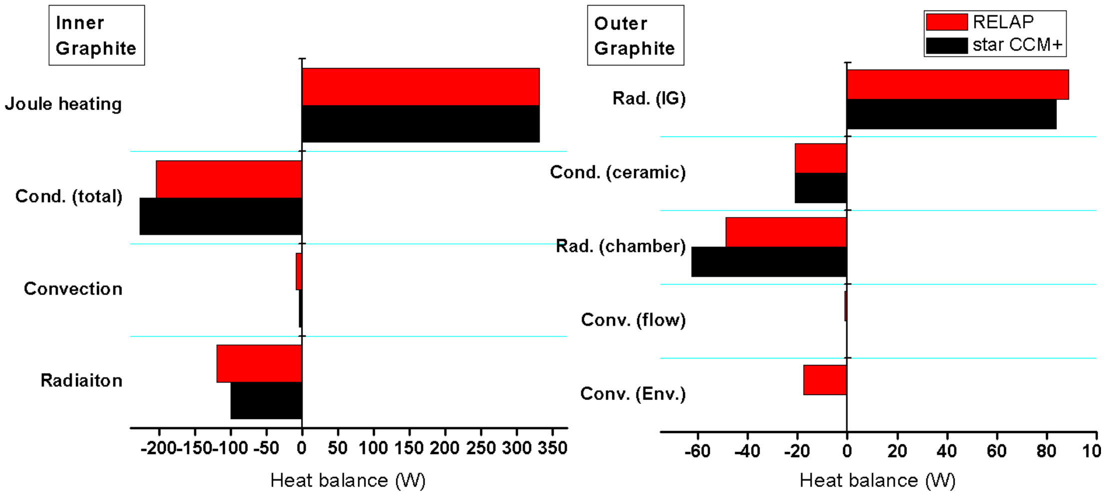

Figure 7.26 Comparison between the RELAP5/SCDAP and star CCM+ predicted heat losses (1150˚C)

As shown in the figures, for inner graphite, the simulation results of RELAP (red bar) and star CCM+ (black bar) agree well with each other, except for the radiation heat transfer, which was slightly larger in RELAP compared to star CCM+ due to the lower outer graphite temperatures in the RELAP cases. Consequently, the vertical conductive heat losses to the ceramic plates and pins were also lower in RELAP to compensate the heat loss through radiation. On the other hand, for outer graphite temperatures, there were more significant differences between two codes. The heat balance difference was mainly found in the convection heat transfer from outer graphite to the argon environment. According to star CCM+, the effect of convective cooling on the outer surface of outer graphite by Argon was generally negligible whereas in RELAP, the cooling effect of argon accounted for approx. 20% to 25% of the total heat losses of outer graphite, which is apparently too significant to be ignored. In star CCM+, an environment boundary condition was applied to the outer radial surface of outer graphite and thus, a convective heat transfer coefficient needs to be manually assigned before the code could compute the temperature fields. A sensitivity analysis regarding the convective heat transfer coefficient at the outer surface of outer graphite was carried out in star CCM+ and it was found that the code had difficulty in matching up with the temperature measured in the experiment unless the coefficient was decreased to 2W/m2K or below. However, in RELAP, this value was estimated to be approx. 10W/m2K. As a matter of fact, both values fall in the range of typical values of natural convection of gases over a hot vertical cylinder, however, the value used in RELAP was five times larger compared to that used in star CCM+, which results in the deviation of other graphite temperatures predicted by RELAP and that predicted by star CCM+ and measured in the experiments.

In addition, we noticed that in the cases of low Reynold number, RELAP would adopt a constant Nusselt number to estimate the convective heat transfer coefficient. Actually, in our case, we found that further reduce the mass flow rate of argon to one-tenth its initial values did not have any effect on the code estimation of convective heat transfer coefficient. In fact, for system analysis code, when the flow is of low Reynold number, it is a common strategy of estimating the convection by adopting a constant Nusselt number (the constant Nusselt number is 4.36 in RELAP and may vary among different codes). Nevertheless, it also has to be admitted that such method could only provide a rough estimation and in our case, the accuracy of the results was limited which leads to the unsatisfying simulation results of outer graphite temperatures. However, it needs to be pointed out that the phenomena that we are interested in are the progression of graphite oxidation accompanied by multimode heat transfer which occur primarily at the inner graphite. Hence, the deviation of outer graphite temperature would not have much effect (it would only slightly alter the radiation heat transfer from inner to outer graphite, as can be confirmed in Figure 7.25 and Figure 7.26, left) on the temperature transient of inner graphite during the gas injections.

Results: Oxidant gas injection

Figure 7.27 illustrates the burn-off computed by RELAP and that measured in the experiments. The weight loss of inner graphite after oxidant gas injection, the burn-off (%) and the percentage error which represents the deviation of the simulation from the experiments are summarized in Table 7.16.

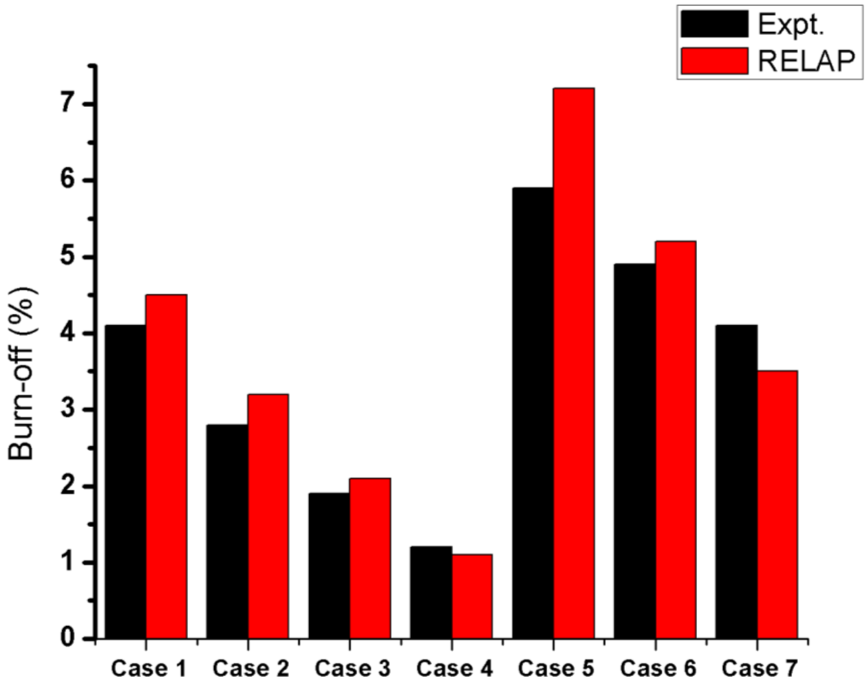

Figure 7.27 Comparison of the code simulated and experimentally measured burn-off

Table 7.16 Weigh loss comparison

Case No.	**Experiment**		**RELAP5/SCDAP**		**Error (%)**
	Weight loss (g)	**Burn-off (%)**	**Weight loss (g)**	**Burn-off (%)**	
1	-0.1369	-4.1%	-0.1508	-4.5%	10.2%
2	-0.0952	-2.8%	-0.1070	-3.2%	12.4%
3	-0.0623	-1.9%	-0.0717	-2.1%	15.1%
4	-0.0392	-1.2%	-0.0367	-1.1%	-6.3%
5	-0.1994	-5.9%	-0.2407	-7.2%	20.7%
6	-0.1630	-4.9%	-0.1734	-5.2%	6.4%
7	-0.1386	-4.1%	-0.1166	-3.5%	-15.9%

As shown in the figure and the table, the simulation results agree fairly well with the experiments. RELAP over predicted the burn-off in five cases (i.e. Case 1, 2, 3, 5 and 6) whereas under predicted the burn-off in only two cases (i.e. Case 4 and 6). The over estimations mainly happened in the cases where the oxidant gas had higher oxygen mole fraction and under estimations of burn-off are more likely to occur if the oxidant gas was of lower oxygen mole fraction. The highest percentage error was 20.7% which was found in Case 5 of which the graphite temperature and oxygen mole fraction were 1150°C and 21% respectively, which were the highest values among all the cases carried out in the experiments. For the other cases, the percentage errors range from 6.3% to 15.9%.

Figure 7.28 shows the temperatures of inner graphite (center) during the oxidant gas injection. Both the results obtained from simulations and experiments were depicted for comparison. The figure on the left shows the temperature transient occurred at 950˚C whereas the figure on the right illustrates the temperature transients occurred at 1150˚C. Inspection of the figures shows that during the gas injection, RELAP tends to overestimate the inner graphite temperature. Specifically speaking, from Case 1 to Case 4, the gas injections were carried out at the inner graphite temperature of approx. 950˚C. In the experiments, an increase in graphite temperature was observed in Case 1 and Case 2 of which the oxygen mole fraction were 21% and 15% respectively. For Case 3 (O2 10%), the inner graphite temperature barely changed and for Case 4, the temperature decreased since the heat removal by the gas flow surpassed the exothermic heat of graphite oxidation. On the other hand, in the simulations, an increase of temperature was found in Case 1(O2 21%), Case 2 (O2 15%) and Case 3(O2 10%), whereas in Case 4 (O2 5%) the heat removal and generation were balanced and temperature remained unchanged. The code predicted temperatures were higher than that of the measurements on an average of approx. 6.2˚C. For the 1150˚C cases, the simulations and experiments matched fairly well on Case 5 (O2 21%) and Case 6 (O2 15%). But for Case 7(O2 5%), a decrease of temperature was observed in the experiments, however, on the contrast, the code predicted that the temperature would slightly increase.

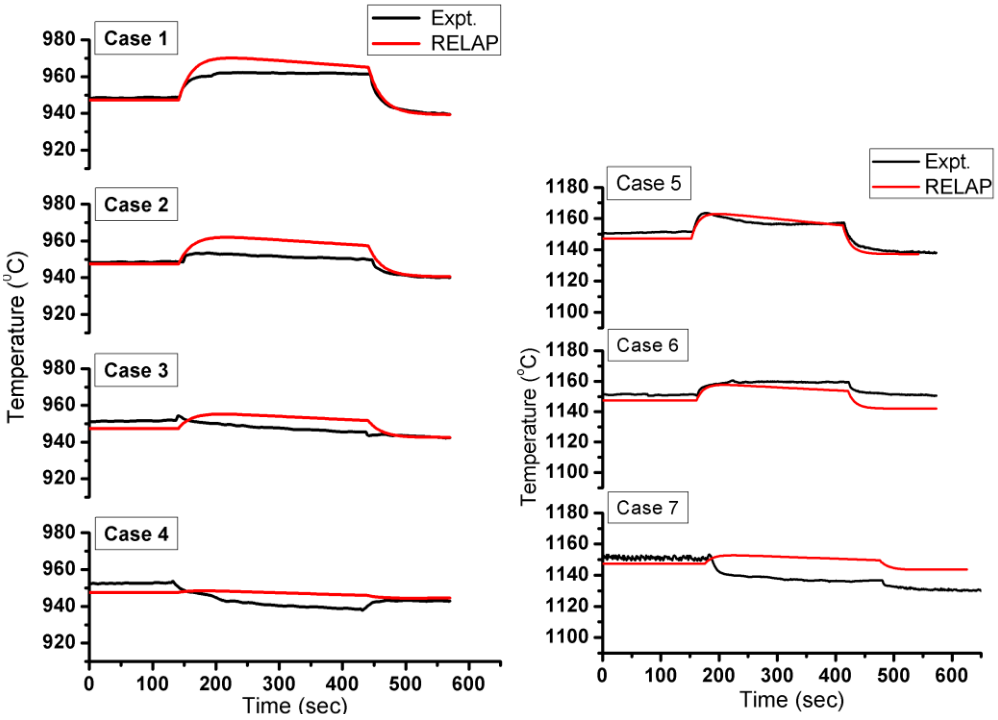

(a) 950˚C cases (b) 1150 ˚C cases

Figure 7.28 The temperature transient of inner graphite (center) during oxidant gas injection from simulations and experiments

There are several reasons why the code predictions somewhat deviated from the measurements. Firstly, it is because of the turbulence in the flow. This is already confirmed by the N2 injection simulations. In RELAP, the flow in this problem was treated as laminar flow (Re: ~20). However, in the experiments, certain level of turbulence existed due to the variation of cross section area of the flow path and thus the cooling effect of convection is larger in experiments than that predicted by the code. Secondly, it was because of over prediction of the exothermic heat. As mentioned previously, RELAP tends to overestimate graphite oxidation in cases with relatively high oxygen mole fraction. This may explain why in Case 1, 2 and 3, the predicted temperature was higher than the measured temperature. Third, in the experiments, the chemical heat generated can be transferred to ceramic plates and pins by conduction in vertical direction. However, in RELAP, this was not taken into account since the code does not compute conduction in the axial direction. As mentioned previously, the conduction in axial direction was computed in star CCM+ and the results was input into RELAP input decks by the means of heat sinks. Nevertheless, those values was computed for the N2 injection case and therefore did not provide insight into how the chemical heat generated was transferred vertically by conduction.

7.4 Conclusions

A transient oxidation experiment was designed and carried out with IG-110 grade graphite. In the experiment, the major phenomena occurring during an event of air ingress, i.e. the oxidation process of graphite accompanied by radiative, convective and conductive cooling were induced and captured. The temperature transient of graphite specimen and its weight loss after the oxidation were measured, from which, a transient graphite oxidation database was established. The database includes seven cases in which the graphite was oxidized at elevated temperature of 950˚C and 1150˚C over an oxygen mole fraction ranging from 5% to 21%. The database derived from the experiment conducted in present study can be used for quantitatively evaluation of transient graphite oxidation analysis of HTGR safety analysis codes.

A RELAP5/SCDAP idealization was constructed for the above test section to assess the capability of the code to model the progression of graphite oxidation while multimode of heat transfer takes place. This study represents the first step in the potential future effort in using RELAP5/SCDAP in HTGR safety analysis.

The thermal hydraulic model was created using the data measured in the experiments with additional inputs (i.e. conductive heat transfer in axial direction and ceramic plate temperatures) calculated by star CCM+. A steady state simulation was firstly performed, generating initial conditions for the transient calculation which was executed afterwards. This simulation scheme was adopted for both N2 and oxidant gas injections. Compared with the experiments, the RELAP5/SCDAP predictions on graphite weigh loss are considered to be within reasonable error bounds (6.3%~20.7%). Nevertheless, it should be noted that REALP5/SCDAP is likely to overestimate the weight loss when the oxidant gas is of higher oxygen concentration and vice versa. The variation of graphite temperature was also compared with the experiments during gas injection. RELAP5/SCADP calculation could predict the general trends during the transient, but the temperature of the graphite was over predicted, especially in the cases conducted at 950˚C, by approx. 6˚C. The additional convective cooling due to the turbulence in the injected flow, the overestimation of graphite oxidation rate and lack of heat removal by means of conduction in axial direction all tend to account for the temperature deviation.

8. Summary and Conclusion

8.1 Summary

The primary objective of this study was to improve the safety analysis of HTGR in an event of air ingress. To accomplish this goal, the present study was carried out in the following three aspects:

1) Validation experiment: Validation experiment plays a key role in quantitative accuracy assessment of safety analysis codes. In present study, a transient graphite oxidation experiment was conducted with grade IG-110 graphite. The experiment is designed to induce the major phenomena occurring during an event of air ingress, which includes the oxidation process of graphite accompanied by multiple modes of heat transfer such as thermal radiation and convective cooling. During the experiment, the gas mixtures of air and N2 were injected from the bottom of the test section after a steady state temperature condition was attained. Graphite temperate (950˚C, 1150˚C) and oxygen mole fraction (5%~21%) were selected as the main experiential variables.

2) IG-110 emissivity measurement: To investigate how oxidation could affect the radiation heat transfer among graphite components, the normal spectral (λ=1.65μm) emissivity of non-oxidized and oxidized IG-110 specimen was measured in a temperature range of 500˚C to 1000˚C utilizing an inferred thermometer and a K-type thermocouple. The measurements provide the HTGR safety analysis codes with the emissivities of oxidized and non-oxidized IG-110 graphite in a wide temperature range, which enables accurate prediction of thermal radiation heat transfer among graphite components during air ingress.

3) REALP5/SCDAP code modification: RELAP5/SCDAP code was improved for analysis of HTGR. Specifically, the thermodynamic and transport properties of O_2, CO_2 and CO were added to RELAP5/SCDAP non-condensable database to support the analysis of air ingress. Major chemical reactions and their rate equations were finalized after extensive literature review. A chemical equilibrium graphite oxidation model (of IG-110) and a CO combustion model were incorporated into the code. For the graphite oxidation model, the multiplication factor M(B), which is a correlation between burn-off and reaction rate, was modified based on six individual graphite oxidation experiments. The code was validated against three experiments, which were conducted by Chi et al., Choi et al. and Ogawa et al., that cover the entire temperature range of HTGR. An assessment of the code performance (i.e. with the correct trends and magnitudes) with respect to the transient analysis of graphite oxidation in conjunction with multiple modes of heat transfer was carried out by comparing the simulation with the validation experiment conducted in present study.

8.2 Conclusion

As mentioned previously, the present study was carried out in three aspects of validation experiments, IG-110 emissivity measurement and RELAP5/SCDAP code improvement. The conclusions of each part are summarized in the following section.

Validation experiment

A transient graphite oxidation experiment was successfully designed and carried out. In the experiment, two major phenomena occurring during an event of air ingress, which are the process of graphite oxidation and radiation heat transfer, were induced and adequately captured. Two forms of data, namely the transient temperature and the weight loss of IG-110 graphite specimen were measured to support the retrospective analysis of the experiment. Moreover, a transient graphite oxidant database was established based on the seven cases conducted at the high temperature regime (950˚C and 1150˚C) over a wide range of oxygen concentration (5% ~21%). The experimental data can be used for validation of numerical modeling of transient graphite oxidation process in conjunction with multimode heat transfers and quantitative evaluation of HTGR safety analysis code in transient graphite oxidation analysis.

IG-110 emissivity measurement

The normal special emissivity (λ=1.65μm) of IG-110 graphite was measured over a temperature range of 500˚C to 1000˚C. The measurement was performed for both non-oxidized and oxidized rectangular bar specimen. The experimental results lead to the following conclusions:

- Oxidized IG-110 graphite is of rougher surface and higher emissivity. This implies that during an event of air ingress, the graphite core components oxidized by the ingress air are of higher emissivity, which means that they can be more efficiently cooled down by radiation heat transfer.

- IG-110 graphite has weak negative temperature dependency of emissivity.

- It has been made clear that the commonly used IG-110 graphite emissivity of 0.8 is conservative for air ingress simulations. Emissivity of 1.0 and 0.80 are suggested as the upper and lower bound respectively for sensitivity analysis.

- Correlations between normal spectral emissivity and temperature were developed for non-oxidized and oxidized IG-110 graphite, which are given as ($\lambda = 1.55\mu$m, 95% confidential interval):

$$\varepsilon_\lambda = (0.881 \pm 0.025) - (4.25 \pm 3.18) \times 10^{-5}\mathrm{T} \quad (\mathrm{non-oxidize})$$

$$\varepsilon_{\lambda} = (0.908 \pm 0.012) - (2.56 \pm 1.56) \times 10^{-5}\mathrm{T} \qquad \text{(oxidized)}$$

According to the above correlations, at 1600°C, which is the safety criteria of HTGR, the emissivity of non-oxidized and oxidized graphite are estimated to be 0.813 and 0.867 respectively.

RELAP5/SCDAP code modification

RELAP5/SCDAP code was improved for analysis of HTGR. The improvements include adding new non-condensable gas species, incorporating relevant chemical reaction models and improved the multiplication factor M(B) for the reaction rate calculation of graphite oxidation. The improved RELAP5/SCDAP code was validated against several steady state and transient graphite oxidation experiments. Comparison between the code's prediction and experimental data leads to the following conclusions:

- The trends of gas mole fractions can be predicted by RELAP5/SCDAP. Specifically, the code predicts that as temperature increases, the graphite oxidation is in favor of generation CO, but as temperature further increases, the CO mole fraction starts to decreases due to CO combustion.

- Compared to the original M(B) proposed by Kim, the graphite oxidation simulation preformed with the modified M(B) agreed better with graphite weight loss data. In other words, the accuracy of the graphite oxidation model in low temperature regime was improved.

- Steady state validation shows that the graphite oxidation model in RELAP5/SCDAP tends to over predict the reaction rate. In Regime III, which is the high temperature regime where oxidation proceeds most, the deviation of simulation results from the experiment was within 20%. On the other hand, for transient validation, the simulation results confirmed that in most cases, the codes would overestimate the reaction rate. But it needs to be noted that slightly under prediction of reaction rate also occurs in the cases of low oxygen concentration. Compared to the experiments, the code predictions on graphite weigh loss were within reasonable error limits of 6.3%~20.7%, which were inconsistence with the steady state validation results. The variation of graphite temperature was compared with the experiments during gas injection. RELAP5/SCADP calculation could predict the general tends during the transient, but the temperature of the graphite was over predicted for approx.6˚C. All in all, the simulation results demonstrate the capability of the improved RELAP5/SCDAP to model the graphite oxidation in an event of air ingress. Nevertheless, the results given by the code would be on the conservative side.

8.3 Recommendation

Validation experiment

In present study, the validation experiments were conducted up to 1150˚C. However, during an event of air ingress, the fuel temperature would rise to 1500˚C or even higher. To measure the oxidation process of graphite under accident temperature would be of great importance for developing and validation of HTGR safety analysis code.

HTGR air ingress simulation

To improve the HTGR safety analysis is the primary goal of present study. The RELAP5/SCDAP, which was validated against both steady state and transient graphite oxidation experiments, is readily to be used. However, the code is not capable of simulating molecule diffusion during the early phase of air ingress. If not coupled with a molecular diffusion code, the assumptions such as the onset time of natural circulation, the flow rate of ingress air, etc. need to be made accordingly.

Acknowledgement

First and foremost, I would like to thank my Supervisor, Dr. Okamoto Koji, for providing me with the opportunity to perform this study. This work would not have been possible without his input and guidance throughout the entire process.

I would like to specifically thank Dr. Kondo and Dr. Erkan. For sharing their opinions, spending time answering my questions and allowing me to take advantage of their knowledge and experience.

At Tokai, my most sincere thanks go to Dr. Sagawa. Thank you for always being supportive and patient. It is your genuine kindness that helped sustain a positive atmosphere in which we overcame numerous difficulties and obstacles.

I would also like to thank to the consultants from Innovative Systems Software, Dr. Chris Allison, Marina, Zheng and Victor, for their assistance with the RELAP5/SCDAP and code modification. It is impossible to imagine how much longer it may have taken without their help.

Also, I give my heartfelt gratitude to all my friends and colleagues at University of Tokyo. Thank you for the fun time in the last three years and for providing me with helpful comments and valuable suggestion on my project.

Finally, a most deserved thanks to my family. None of this would literally have been possible without you and I know I can always count on your support.

References

---

1 Sterbentz, J. W., Sant, R. L. “Neutronics Point-Design of a Prismatic Very High Temperature Reactor.” Proceedings of Global 2003: Atoms for Prosperity. November 2003, New Orleans, pp. 300 – 311.

2 International Atomic Energy Agency. IAEA-TECDOC-1198. Current Status and Future Development of Modular High Temperature Gas Cooled Reactor Technology. February 2001.

3 Hishida M, Fumizawa M, Takeda T, et al. Researches on air ingress accidents of the HTTR[J]. Nuclear engineering and design, 1993, 144(2): 317-325.

4 Ogawa M. Mass transfer with graphite oxidation in gas mixture laminar flow through circular tube[J]. Nippon Genshiryoku Gakkai-Shi, 1993, 35(3): 245-252. (1988).

5 Somiya S. Handbook of advanced ceramics: materials, applications, processing, and properties[M]. Academic press, 2013.

6 Allison C M, Hohorst J K. Role of RELAP/SCDAPSIM in nuclear safety[J]. Science and technology of Nuclear Installations, 2010, 2010.

7 STAR-CCM. (n.d.). Retrieved May 01, 2017, from https://mdx.plm.automatio

n.siemens.com/star-ccm-plus

8 (n.d.).Retrieved May 01, 2017, from http://www2.cd-adapco.com/l/14592/

2016-08-23/6m1v4r

9 Walker P L, Rusinko F, Austin L G. Gas reactions of carbon[J]. Advances in catalysis, 1959, 11: 133-221.

10 Blyholder G, Eyring H. Kinetics of graphite oxidation[J]. The Journal of Physical Chemistry, 1957, 61(5): 682-688

11 Nuclear corrosion science and engineering[M]. Elsevier, 2012.

12 Kim E S, No H C, Kim B J, et al. Estimation of graphite density and mechanical strength variation of VHTR during air-ingress accident[J]. Nuclear Engineering and Design, 2008, 238(4): 837-847.

13 Moormann R. and Hinssen H.-K. (2002), advanced graphite oxidation models in: Basic studies in the field of high temperature engineering, NEA-OECD, Paris.

14 Welty J R, Wicks C E, Rorrer G, et al. Fundamentals of momentum, heat, and mass transfer[M]. John Wiley & Sons, 2009. P398

15 Fletcher C D, Schultz R R. RELAP5/MOD3 Code Manual Volume II: User’s Guide and Input Requirements[J]. Idaho National Engineering Laboratory, Idaho, USA, 1995.

16 Allison C M, Berna G A, Coryell E W, et al. SCDAP/RELAP5/MOD3. 2 Code Manual Volume III: SCDAP/RELAP5 Users Guide and Input Manual[R]. NUREG/CR-6150 Rev. 1, EGG-2720, Idaho National Engineering and Environmental Laboratory, Idaho Falls, ID, 1998.

17 Coryell E W, Allison C M, Berna G A. SCDAP/RELAP5/MOD 3.2 code manual: Interface theory. Volume 1[R]. Nuclear Regulatory Commission, Washington, DC (United States). Div. of Systems Technology; Idaho National Engineering Lab., Idaho Falls, ID (United States), 1998.

18 Carlson, K. E., et al. "Relap5/mod3 code manual volume i: Code structure, system models and solution methods." US NRC NUREG/CR-5535, Washington (DC, USA) June (1990).

19 Katscher, W., Moorman, R., 1986. Graphite Corrosion under Severe HTR Accident Condition, IAEA Specialists' Meeting on Graphite Component Structural Design, JAERI Tokai (Japan), September 8–11, IWGGCR-11, pp. 182–188.

20 Velasques, C., Hightower, G., Burnette, R., 1978. The Oxidation of H-451 Graphite by Steam, Part 1: Reaction Kinetics, GA-A14951, General Atomtics, San Diego, CA.

21 O'Brien, M.H., Merrill, B.J., Ygaki, S.N., 1988. Combustion testing and Thermal Modeling of Proposed CIT Graphite Tile Materials, EGG-FSP-8255, Eg&G Idaho.

22 Rossberg M. Experimentelle Ergebnisse über die Primärreaktionen bei der Kohlenstoffverbrennung[J]. Zeitschrift für Elektrochemie, Berichte der Bunsengesellschaft für physikalische Chemie, 1956, 60(9-10): 952-956.

23 Hinssen, H.K., Katcher, W., Moorman, R., 1983. Kinetics der Graphite/Sauerstoff Reaction Juel-1875.

24 Takahashi M, Kotaka M, Sekimoto H. Burn-off and Production of CO and CO2 in the Oxidation of Nuclear Reactor-Grade Graphites in a Flow System[J]. Journal of Nuclear Science and Technology, 1994, 31(12): 1275-1286.

25 Kim E S, No H C. Experimental study on the oxidation of nuclear graphite and development of an oxidation model[J]. Journal of Nuclear Materials, 2006, 349(1): 182-194.

26 Lim, H. S. and H. C. No, 2003, "Transient multicomponent mixture analysis based on ICE numerical scheme for predicting an air ingress phenomena in an HTGR," 10th International Topical Meeting on Nuclear Reactor Thermal Hydraulics (NURETH-10), Seoul, Korea, October 5-9, 2003.

27 Xiaowei L, Jean-Charles R, Suyuan Y. Effect of temperature on graphite oxidation behavior[J]. Nuclear Engineering and design, 2004, 227(3): 273-280.

28 Blanchard, A. Appendix 2. The Thermal Oxidation of Graphite, Irradiation Damage in Graphite Due to Fast Neutrons in Fission and Fusion Systems, IAEA-TECDOC-1154. pp. 207–213.

29 El-Genk M S, Tournier J M P. Sherwood number correlation for nuclear graphite gasification at high temperature[J]. Progress in Nuclear Energy, 2013, 62: 26-36.

30 Fuller E L, Okoh J M. Kinetics and mechanisms of the reaction of air with nuclear grade graphites: IG-110[J]. Journal of Nuclear Materials, 1997, 240(3): 241-250.

31 M.B. Richards, Energy 15 1990. 729

32 Kakaç, S., Yener, Y., 1995. Convective Heat Transfer, second ed. CRC Press, Inc., Ann Arbor, MI, pp. 119e185 (Chapter 6).

33 Hee C, Kim J, Park G C, et al. Development of Safety analysis codes and experimental validation for a very high temperature gas-cooled reactor[R]. INEEL/EXT-04-02459 Idaho National Engineering and Environmental Laboratory, 2004.

34 Oh, C. H., B. J. Merrill, R. L. Moore

35 Lim H S, No H C. Transient Multicomponent Mixture Analysis Based On an ICE Numerical Technique for the Simulation of an Air Inggess Accident in an HTGR[J]. Nuclear Engineering and Technology, 2004, 36(5): 375-387.

36 Dryer F L, Glassman I. High-temperature oxidation of CO and CH4[C]//Symposium (International) on combustion. Elsevier, 1973, 14(1): 987-1003.

37 Howard J B, Williams G C, Fine D H. Kinetics of carbon monoxide oxidation in postflame gases[C]//Symposium (International) on Combustion. Elsevier, 1973, 14(1): 975-986.

38 Takeda T, Hishida M. Studies on molecular diffusion and natural convection in a multicomponent gas system[J]. International Journal of Heat and Mass Transfer, 1996, 39(3): 527-536.

39 Schlögl B. Oxidation kinetics of innovative carbon-based materials in severe air ingress accidents in HTRs[J]. Safety Research for Nuclear Reactors, 23.

40 Moormann, R., 1984. Effect of delays in afterheat removal on consequences of massive air ingress accidents in high temperature gas cooled reactors. J. Nucl. Sci. Technol. 21 (11), 824.

41 Xu Wei. Analysis of A Massive Air Ingress Accident of The High Temperature Gas Cooled Reactor Pebble-bed Module (HTR-PM).ANS 2016 winter conference, Las Vegas

42 Heat transfer and fluid flow in nuclear systems[M]. Elsevier, 2013. P335

43 Greene G A, Finfrock C C, Irvine T F. Total hemispherical emissivity of oxidized Inconel 718 in the temperature range 300–1000° C[J]. Experimental Thermal and Fluid Science, 2000, 22(3): 145-153.

44 Smetana W, Reicher R. A new measuring method to determine material spectral emissivity[J]. Measurement Science and Technology, 1998, 9(5): 797.

45 Wan Z, Ng D, Dozier J. Spectral emissivity measurements of land-surface materials and related radiative transfer simulations[J]. Advances in Space Research, 1994, 14(3): 91-94.

46 Krishna M G, Rajendran M, Pyke D R, et al. Spectral emissivity of ytterbium oxide-based materials for application as selective emitters in thermophotovoltaicdevices[J]. Solar energy materials and solar cells, 1999, 59(4): 337-348.

47 Iuchi T, Furukawa T, Wada S. Emissivity modeling of metals during the growth of oxide film and comparison of the model with experimental results[J]. Applied optics, 2003, 42(13): 2317-2326.

48 Zhang B, Redgrove J, Clark J. New apparatus for measurement of the spectral, angular, and total emissivity of solids[J]. High Temperatures-High Pressures, 2004, 36(3): 289-302.

49 Sova, Raymond M., et al. "High-temperature infrared properties of sapphire, AlON, fused silica, yttria, and spinel." Infrared Physics & Technology 39.4 (1998): 251-261.

50 Goodwin A, Marsh K N, Wakeham W A. Measurement of the thermodynamic properties of single phases[M]. Elsevier, 2003.p493

51 Sridharan K, Allen T, Anderson M, et al. Emissivity of Candidate Materials for VHTR Applicationbs: Role of Oxidation and Surface Modification Treatments[R]. University of Wisconsin, 2011.

52 del Campo L, Pérez-Sáez R B, Esquisabel X, et al. New experimental device for infrared spectral directional emissivity measurements in a controlled environment[J]. Review of scientific instruments, 2006, 77(11): 113111.

53 GrenisA F, Levitt A P. The spectral emissivity and total normal emissivity of commercial graphites at elevated temperatures[R]. Watertown Arsenal Labs., Mass., 1962.

54 Thorn R J, Simpson O C. Spectral emissivities of graphite and carbon[J]. Journal of Applied Physics, 1953, 24(5): 633-639.

55 Pierson H O. Handbook of carbon, graphite, diamonds and fullerenes: processing, properties and applications[M]. William Andrew, 2012.P109

56 Null M R, Lozier W W. Measurement of reflectance and emissivity of graphite at arc temperature with a carbon arc image furnace[J]. Journal of Applied Physics, 1958, 29(11): 1605-1605.

57 Neuer G, Jaroma-Weiland G. Spectral and total emissivity of high-temperature materials[J]. International Journal of Thermophysics, 1998, 19(3): 917-929

58 Wang F, Cheng L, Mei H, et al. Effect of surface microstructures on the infrared emissivity of graphite[J]. International Journal of Thermophysics, 2014, 35(1): 62-75.

59 Kostanovskii A V, Zeodinov M G, Kostanovskaya M E. The determination of thermal conductivity and emissivity of graphite at high temperatures[J]. High Temperature, 2005, 43(5): 793-795.

60 Kostanovskii A V, Zeodinov M G, Kostanovskaya M E. The thermal conductivity and emissivity of DE-24 graphite at temperatures of 2300-3000 K[J]. Measurement Techniques, 2011, 53(12): 1380.

61 Seo S K, Roh J S, Kim E S, et al. Thermal Emissivity of Nuclear Graphite as a Function of Its Oxidation Degree (1)-Effects of Density, Porosity, and Microstructure[J]. Carbon letters, 2009, 10(3): 225-229.

62 Seo S K, Roh J S, Kim E S, et al. Thermal emissivity of a nuclear graphite as a function of its oxidation degree (2)-effect of surface structural changes[J]. Carbon letters, 2009, 10(4): 300-304.

63 Seo S K, Roh J S, Kim S H, et al. Thermal Emissivity of Nuclear Graphite as a Function of its Oxidation Degree (3): Structural Study using Scanning Electron Microscope and X-Ray Diffraction[J]. Carbon letters, 2011, 12(1): 8-15.

64 TEMPAX. (n.d.). Retrieved May 11, 2017, from http://www.glass-dictionary.com/tainetu/tennpakkusu/

65 Davis C B, Oh C H. The addition of noncondensable gases into Relap5-3D for analysis of high temperature gas-cooled reactors[R]. Idaho National Laboratory (INL), 2003.

66 Chi S H, Kim G C. Comparison of the oxidation rate and degree of graphitization of selected IG and NBG nuclear graphite grades[J]. Journal of nuclear materials, 2008, 381(1): 9-14.

67 Choi, Woong-Ki, et al. "Oxidation behavior of IG and NBG nuclear graphites." Nuclear Engineering and Design 241.1 (2011): 82-87.

68 Contescu C I, Guldan T, Wang P, et al. The effect of microstructure on air oxidation resistance of nuclear graphite[J]. Carbon, 2012, 50(9): 3354-3366.

69 Kim E S, No H C. Experimental study on the reaction between nuclear graphite IG-110 and carbon dioxide[J]. Journal of nuclear materials, 2006, 350(1): 96-100.

70 Wang P, Contescu C I, Yu S, et al. Pore structure development in oxidized IG-110 nuclear graphite[J]. Journal of Nuclear Materials, 2012, 430(1): 229-238.

71 Adachi M, Shioyama H, Narisawa M, et al. The Temperature Dependence of Electrical Resistivity of Polycrystalline Graphite in the Range of 900K-2800K[J]. Tan

72 Ishihara, M., Iyoku, T., Toyota, J., Sato, S., Shiozawa, S., An Explication of Design Data of the Graphite Structural Design Code for Core Components of High Temperature Engineering Test Reactor, JAERI-M 91-153, 1991